



POLITECNICO DI TORINO

Master's Degree in Aerospace Engineering

Tesi di Laurea Magistrale

**Optimal Control Theory applied to
interplanetary transfer for a
Near-Earth Asteroid retrieval
Mission**

Relatori

prof.ssa Manuela Battipede
ing. Luigi Mascolo, PhD

Candidato

Alessandro Labarbuta
matricola: 293010

JULY 2024

Sommario

The growing interest in exploiting extraterrestrial resources has spotlighted asteroid retrieval missions as a pivotal strategy for resource utilization and planetary defense. This study proposes a non-destructive retrieval approach by rendezvousing with Near-Earth Asteroids (NEA) and utilizing guided propulsion to move part of its mass closer to Earth in order to allow in-orbit production of spacecraft components without launching them from Earth making spacecraft construction less expensive.

From the JPL Small Bodies Database, a refined selection of asteroids is identified through a Pareto front analysis that searches for bodies that have the best orbital parameters' proximity to those matching the departure point, at the Sun-Earth Lagrange Point L2. Optimal low-thrust trajectories via indirect methods based on the Optimal Control Theory are determined for the spacecraft to rendezvous with the asteroids. Upon attachment, a matching the retrieved asteroid's mass is introduced, and the mission transitions to seeking the quickest manoeuvre to retrieve the highest possible amount of asteroid mass back to strategic points in the Earth-Moon system such as the L4 or L5 Lagrangian points. The desired trajectory is calculated using a single-shooting method relying on the Pontryagin's Minimum Principle (PmP) to reduce the propellant mass spent and an autonomous switching function based on the bang-bang control to regulate the thrust without having previously specified the thrust and coasting arcs, this being possible thanks to the complexity of gravitational interactions among the considered celestial bodies.

The dynamic modeling of planetary bodies' positions relies on JPL DE441 ephemeris incorporating the gravitational influence of the Sun in a two-bodies system.

Table of contents

Elenco delle figure	IV
Elenco delle tabelle	VIII
1 Introduction	1
2 Dynamics of the system	3
2.1 The N-body problem	3
2.2 The two-body problem	4
2.2.1 The equation of the relative motion	4
2.2.2 Constants of motion	6
2.3 The reference frame	7
2.3.1 The Heliocentric-Ecliptic reference frame	7
2.3.2 The perifocal reference frame	8
2.3.3 Ephemerides and Julian Day	10
2.3.4 Classical orbital parameters	12
2.4 Equations of dynamics	16
2.4.1 Equations of dynamics in Cartesian coordinates	17
2.5 Electrical propulsion	17
2.6 Lagrangian Points	19
3 Implementation of the mathematics	23
3.1 Differential corrector	23
3.2 Single-shooting procedure	25
3.2.1 Single-shooting procedure for free-TOF and free- ν vs fixed-TOF and fixed- ν calculations	27
3.3 Non-dimensionalizing values adopted	28
3.4 Implementation of the code	28
4 The Optimal Control Problem (OCP)	30
4.1 Direct vs Indirect Numerical Methods	30
4.2 The Optimal Control Theory	31
4.3 Multi-Point Optimal Control Theory	34
4.4 The implemented Boundary Value Problem	36
4.5 OCP for spacecraft trajectory optimization	38
4.5.1 The reduced transversality conditions	40

5	Case study: Near-Earth Asteroids (NEA) targeting and retrieval mission	42
5.1	Asteroids selection process	44
5.1.1	The estimation of the asteroid mass and diameter	46
6	Results	48
6.1	Trajectories from Earth to 2013BS45	48
6.1.1	Principal family of solutions for 2013BS45 rendez-vous	51
6.1.2	Secondary family of solutions for 2013BS45 rendez-vous	66
6.1.3	Solutions TOF-free for transfers towards 2013BS45 orbit	68
6.1.4	Optimal adjoint variables values and their dependence with time of flight and true anomaly	75
6.2	Feasibility conditions for a rendez-vous through a TOF-free maneuver . . .	81
6.3	Retrieval maneuver	88
6.3.1	Transfer towards the waiting orbit	89
6.3.2	Transfer towards Earth orbit	90
6.4	Conclusions	96
6.5	Future Research	97
A	Equations for the adjoint variables	99
B	List of the selected asteroids	100

Table of contents

Elenco delle figure

2.1	Gravitational interaction between two bodies m_1 and m_2	5
2.2	Heliocentric-Ecliptic reference frame (black axes) [20]	8
2.3	Perifocal plane [12]	9
2.4	Rotation from Cartesian to perifocal reference frame [12]	10
2.5	Classical orbital parameters [34]	12
2.6	Structure of an elliptical orbit [54]	13
2.7	Hyperbolic orbit [21]	16
2.8	The synodical reference frame for a three body problem [42]	19
2.9	Position of the five Lagrangian points in a gravitational system of two main bodies m_1 and m_2 [15]	20
2.10	The potential function \mathcal{U} close to the Lagrangian points [51]	22
4.1	Schematic representation of the MPBVP arc discretization of its domain and its trajectory [34]	35
5.1	Orbits of the selected NEA	46
6.1	Trajectory resulting from a failed convergence process with too high initial costates on velocity components	51
6.2	Trajectory resulting from a failed convergence process with too high initial costates on position components	52
6.3	3D optimal transfer towards 2013BS45 with rendez-vous on May 27 th , 2026	53
6.4	2D optimal transfer towards 2013BS45 with rendez-vous on May 27 th , 2026	54
6.5	Orbital, angular and thrust data from maneuver for rendez-vous with 2013BS45 on May 27 th , 2026	54
6.6	3D optimal transfer towards 2013BS45 with rendez-vous on November 16 th , 2025	55
6.7	2D optimal transfer towards 2013BS45 with rendez-vous on November 16 th , 2025	55
6.8	Orbital, angular and thrust data from maneuver for rendez-vous with 2013BS45 on November 16 th , 2025	56
6.9	Arc of the 2013BS45 orbit where no convergence has been found	56
6.10	3D optimal transfer towards 2013BS45 with rendez-vous on July 4 th , 2026 .	57
6.11	2D optimal transfer towards 2013BS45 with rendez-vous on July 4 th , 2026 .	57
6.12	Orbital, angular and thrust data from maneuver for rendez-vous with 2013BS45 on July 4 th , 2026	58

6.13	3D optimal transfer towards 2013BS45 with rendez-vous on August 27 th , 2026	58
6.14	2D optimal transfer towards 2013BS45 with rendez-vous on August 27 th , 2026	59
6.15	Orbital, angular and thrust data from maneuver for rendez-vous with 2013BS45 on August 27 th , 2026	59
6.16	3D optimal transfer towards 2013BS45 with rendez-vous on January 14 th , 2027	60
6.17	2D optimal transfer towards 2013BS45 with rendez-vous on January 14 th , 2027	60
6.18	Orbital, angular and thrust data from maneuver for rendez-vous with 2013BS45 on January 14 th , 2027	61
6.19	Values for m_f over TOF for trajectories among the primary family of solutions	61
6.20	Primary family maneuvers	62
6.21	3D optimal transfer towards 2013BS45 starting on January the 4 th , 2025 with rendez-vous on July 26 th , 2026	63
6.22	Orbital, angular and thrust data from maneuver starting on January the 4 th , 2025 for a rendez-vous with 2013BS45 on July 26 th , 2026	63
6.23	Data from the diverging solution for the transfer towards 2013BS45 (attempted rendez-vous on 26 th July 2026) before the first use of the pseudo-inverse of the Jacobian matrix	64
6.24	Data from the diverging solution for the transfer towards 2013BS45 (attempted rendez-vous on 26 th July 2026) at the first use of the pseudo-inverse of the Jacobian matrix	65
6.25	Data from the diverging solution for the transfer towards 2013BS45 (attempted rendez-vous on 26 th July 2026) at the 5 th and last use of the pseudo-inverse of the Jacobian matrix	65
6.26	3D optimal transfer towards 2013BS45 with rendez-vous on November 4 th , 2026	68
6.27	2D optimal transfer towards 2013BS45 with rendez-vous on November 4 th , 2026	69
6.28	Orbital, angular and thrust data from maneuver for rendez-vous with 2013BS45 on November 4 th , 2026	69
6.29	3D optimal transfer towards 2013BS45 with rendez-vous on November 4 th , 2026 (from primary family)	70
6.30	Orbital, angular and thrust data from maneuver for rendez-vous with 2013BS45 on November 4 th , 2026 (from primary family)	70
6.31	3D optimal transfer towards 2013BS45 with rendez-vous on January 20 th , 2027	71
6.32	2D optimal transfer towards 2013BS45 with rendez-vous on January 20 th , 2027	72
6.33	Orbital, angular and thrust data from maneuver for rendez-vous with 2013BS45 on January 20 th , 2027	72
6.34	3D optimal transfer towards 2013BS45 with rendez-vous on February 3 rd , 2027	73
6.35	2D optimal transfer towards 2013BS45 with rendez-vous on February 3 rd , 2027	74

6.36	Orbital, angular and thrust data from maneuver for rendez-vous with 2013BS45 on February 3 rd , 2027	74
6.37	3D optimal transfer towards 2013BS45 with rendez-vous on September 26 th , 2027	75
6.38	2D optimal transfer towards 2013BS45 with rendez-vous on September 26 th , 2027	76
6.39	Orbital, angular and thrust data from maneuver for rendez-vous with 2013BS45 on September 26 th , 2027	76
6.40	Secondary family maneuvers	77
6.41	Comparison between m_f for maneuvers from primary and secondary family	77
6.42	3D optimal transfer towards 2013BS45 at $\nu = 256.1^\circ$	78
6.43	2D optimal transfer (zoom) towards 2013BS45 at $\nu = 256.1^\circ$	79
6.44	Orbital, angular and thrust data from maneuver towards 2013BS45 orbit at $\nu = 256.1^\circ$	79
6.45	3D optimal transfer towards 2013BS45 at $\nu = 320.3^\circ$	80
6.46	2D optimal transfer (zoom) towards 2013BS45 at $\nu = 320.3^\circ$	81
6.47	Orbital, angular and thrust data from maneuver towards 2013BS45 orbit at $\nu = 320.3^\circ$	81
6.48	3D optimal transfer towards 2013BS45 at $\nu = 185.0^\circ$	82
6.49	2D optimal transfer (zoom) towards 2013BS45 at $\nu = 185.0^\circ$	83
6.50	Orbital, angular and thrust data from maneuver towards 2013BS45 orbit at $\nu = 185.0^\circ$	83
6.51	Optimal maneuvers towards 2013BS45 obtained leaving TOF free	84
6.52	Final mass comparison between TOF-free, primary family and secondary family of solutions	84
6.53	Variations of λ_x , λ_y and λ_z over TOF and ν of the mission for free-TOF optimal maneuver for 2013BS45	85
6.54	Variations of λ_{v_x} , λ_{v_y} , λ_{v_z} and λ_m over TOF and ν of the mission for free-TOF optimal maneuver for 2013BS45	85
6.55	Variations of λ_x , λ_y and λ_z over TOF and ν of the mission for primary family of rendez-vous solutions for 2013BS45	86
6.56	Variations of λ_{v_x} , λ_{v_y} , λ_{v_z} and λ_m over TOF and ν of the mission for primary family of rendez-vous solutions for 2013BS45	86
6.57	Variations of λ_x , λ_y and λ_z over TOF and ν of the mission for secondary family of rendez-vous solution for 2013BS45	87
6.58	Variations of λ_{v_x} , λ_{v_y} , λ_{v_z} and λ_m over TOF and ν of the mission for secondary family of rendez-vous solutions for 2013BS45	87
6.59	Comparison over variations of adjoint variables λ and final mass m_f between the primary family (blue) and the secondary family (orange) of solutions	88
6.60	3D transfer towards waiting orbit starting on January the 4 th , 2027 from 2013BS45 orbit with arrival on March the 6 th , 2028	91
6.61	Orbital, angular and thrust data from maneuver towards waiting orbit starting on January the 4 th , 2027 from 2013BS45 orbit with arrival on March the 6 th , 2028	91
6.62	3D minimum-TOF transfer towards Earth orbit at $\nu = 80.54^\circ$	93
6.63	Data for the minimum-TOF transfer towards Earth orbit at $\nu = 80.54^\circ$	93

6.64 Retrieved mass over initial mass ratio over the number of retrieved asteroids
from the paper by Ionescu, Ceriotti, McInnes (results and image from [23]) 96

Elenco delle tabelle

- 1.1 Data for a generical launch from the Earth surface towards LEO, from [24] 2
- 2.1 Gravitational parameter (μ) for the main bodies of the Solar Systems . . . 6
- 2.2 Keplerian orbital parameters 12
- 3.1 Average iteration rate given one random calculation for each possible architecture (both TOF and ν fixed or only ν fixed) 29
- 6.1 Spacecraft characteristics at the beginning of the transfer towards 2013BS45 49
- 6.2 Keplerian parameters of the starting point of all the trajectories described in this chapter 49
- 6.3 Characteristics of 2013BS45, part 1 50
- 6.4 Characteristics of 2013BS45, part 2 50
- 6.5 Comparison between transfers towards $\nu = 229.67^\circ$ (rendez-vous on 4th of November 2026, TOF = 794 days) from Primary and Secondary Family . . 67
- 6.6 $\Delta\nu$ between asteroids and their ideal position to be reached in a rendez-vous after the quickest TOF-free optimal transfer from Earth 88
- 6.7 Time to the next availability for the least-TOF free-TOF maneuver 89
- 6.8 Mass data about the spacecraft after the rendez-vous with the asteroid . . 89
- 6.9 Keplerian parameters of the waiting orbit 90
- 6.10 Mass data about the spacecraft after reaching the waiting orbit (retrieved asteroid mass = 15000 kg) 90
- 6.11 Keplerian parameters for starting orbit and target orbit for the last maneuver of the mission 92
- 6.12 Mass data about the second spacecraft carrying the first spacecraft(2537.15 kg) and the asteroid mass retrieved (15000 kg) back to Earth orbit 92
- 6.13 Waiting time for the spacecraft on the waiting orbit (wo) before the beginning of the maneuver to reach Earth orbit 94
- 6.14 Comparison between maneuvers between 2013BS45 orbit and the waiting orbit 94
- 6.15 Comparison between maneuvers between the waiting orbit and Earth orbit 95
- 6.16 Comparison between waiting time for the spacecraft on the waiting orbit (wo) before the beginning of the maneuver to reach Earth orbit between the two cases of retrieved mass considered (15000 kg vs 16000 kg), $\Delta n = 6.5174 \cdot 10^{-7}^\circ/\text{s}$ 95
- B.1 Keplerian parameters of the selected asteroids 101

B.2	Orbital characteristics of the selected asteroids	102
B.3	Physical characteristics of the selected asteroids	103

Acronimi

EO Earth Orbit

ISS International Space Station

JAXA Japanese Aerospace Exploration Agency

JD Julian Day

JPL Jet Propulsion Laboratory

LEO Low Earth Orbit

MPBVP Multi-Point Boundary Value Problem

NASA National Aeronautic and Space Agency

NEA Near-Earth Asteroids

NEO Near-Earth Objects

NMR Nuclear Magnetic Resonance

OCP Optimal Control Problem

OCT Optimal Control Theory

ODEs Ordinary Differential Equations

PGMs Platinum Group Materials

PmP Pontryagin's minimum Principle

RAAN Right Ascension of the Ascending Node

ROI Return On Investments

RTBP Restricted Three-Body Problem

STM State Transition Matrix

TBP Two-Body Problem

TOF Time of Flight

TPBVP Two-Point Boundary Value Problem

Alessandro Labarbuta
matricola: 293010

18 luglio 2024

Capitolo 1

Introduction

One of the most engaging enterprises ever attempted by human race, with its unique ability to unify people from countries politically nearly unable to establish long-term peaceful relations and to bring those countries to join their forces to build the most amazing (and expensive) structure in the history of mankind, the International Space Station (ISS), is space exploration.

After an initial "golden age" culminated with the *Apollo* missions designed by National Aeronautic and Space Agency (NASA) (1969-1972) and followed by some decades of less celebrated activity, in the last decade space exploration has known a new growth in interest from both the general public and private companies (this comes more as a novelty considered the complete domain national agencies used to have on the subject of space exploration) with the arise of new protagonist like Elon Musk and Jeff Bezos which have started companies (*Space X* and *Blue Origin* respectively) that design vehicles capable to reach space for commercial flights, and new challenges such as the attempt to land a man on the surface of Mars (many mission like the most recent *Curiosity* and *Perseverance* by NASA and the *ExoMars* designed by ESA involving automatic mechanical probes and rovers have been successfully attempted or are currently under development) or the attempt to establish once and for all the human presence on the surface of our only natural satellite, the Moon, with the *Artemis* program alongside with the project of a space station orbiting it (the *Lunar Gateway*).

In this context space trajectory optimization has always been crucial in bolstering the feasibility of every mission. In fact, if we consider the arch-famous Tsiolkovski's *Rocket equation* [47],

$$m_f = m_0 e^{-\frac{\Delta V}{c}} \quad (1.1)$$

where m_0 and m_f are the initial and the final mass of the spacecraft, ΔV is the term that indicates how much energy (in terms of kinetic energy) the spacecraft needs to be given to perform the desired transfer and c is the *effective exhaust velocity* measuring the performance provided by the propellant, assuming we want to launch a 1 kg spacecraft to insert it into Low Earth Orbit (LEO) (for the characteristics of the given transfer and the considered spacecraft see table 1.1) through chemical propulsion, the only way we know to generate the high amount of thrust necessary to defy gravitational pull exerted by Earth [47], we get that more than 27 kg of propellant (excluding the engines and the tanks

themselves that would influence the actual result) are necessary and this value grows with the ΔV of the maneuver and the inefficiencies of the propellant and the thruster itself.

ΔV	≈ 10 km/s
c	2943 m/s
I_{sp}	300 s
g_0	9.81 m/s
desired m_f	1 kg
necessary m_0	28 kg

Tabella 1.1: Data for a generical launch from the Earth surface towards LEO, from [24]

This little example clarifies how crucial optimization in general, and space trajectory optimization in particular, can be to reduce mission costs. In fact, when talking about designing flying vehicles (so this is true for little airplanes and for space ships as well), we do not want to bring on board what we do not really want or need because every kg of mass brought has its cost, whether in terms of chemical propellant or in terms of Xenon, the gaseous propellant used for electrical propulsion [24].

In fact, since the late sixties (when thrusters still happened to be called *thrusters* in scientific literature and the *Apollo* space program was still in progress) electric propulsion was seen as a potential way to generate thrust for in-space maneuvers because of their undisputed efficiency and endurance, especially for attitude corrections where accelerations on the order of 10^{-5} to $10^{-4} g_0$ are sufficient, along (at that time) with nuclear-heated, hydrogen-fueled engines [45]. However in the following decades those two technologies diverged in their development path with electrical propulsion whose use has become prominent also for deep-space missions [26] even though its potential has not been fully expressed yet. The only downside of such technology is the longer mission time it requires to complete it when using electric thrust because of the very low force produced. In fact some groups of this family of thrusters, specifically the ion-thrusters, can produce an amount of thrust in a range of [0.01, 500]mN, depending on the propellant, with a 80% efficiency and a durability in terms of years [47]. This makes them one of the best options we have right now for long-time in-space maneuvers.

The goal of this thesis is building a Python code that is able to perform optimal trajectories calculations inside a Two-Body Problem (TBP) with a focus in reducing the needed propellant mass and validating it by applying it to the case study of an asteroid retrieval mission with the task to find the optimal trajectory that enables the spacecraft to reach the targeted NEA with the least amount of mass of propellant spent.

The code implements a differential correction that through a *try-and-error* single-shooting process (described in chapter 3) applies the Optimal Control Theory (OCT) and therefore the Pontryagin's minimum Principle (PmP) in order to minimize the *objective function* that depends on the variables that we want to minimize to achieve the desired optimization (in our case it is the mass of propellant spent), as it is discussed in chapter 4, through an iterative correction of the initial guess made by the user of the code about the initial state variables which are not constrained.

In the chapter 5 the case-study of the asteroid retrieval will be discussed while in chapter 6 the results will be shown along with the notes about possible future research that could improve the work done for this thesis.

Capitolo 2

Dynamics of the system

In this chapter the dynamical model considered for this work will be described. Given the nature of the gravitational system we operate in where the Sun is the central body with all the planets and other celestial bodies orbiting it and exerting their gravitational influences on each other the dynamical model of the *n-body system* is discussed. However, for this work of thesis, all the gravitational influences besides the one of the central body have been neglected so a particular case of n-body system, the two-body system, has been implemented and therefore it will be discussed afterwards. The definition of the considered reference frames are also given along with their description and with the Ephemerides system, the Julian Day calendar used in this work as a reference for space-time coordinates of the celestial bodies along their orbits and the Keplerian orbital parameters and all the other characteristics of an orbit. Lastly, the equations of the dynamics are represented along with some generic information about electric propulsion and Lagrange points (all the trajectories discussed in chapter 6 have the L2 point of the Sun-Earth system as a starting point, so some elements about the Restricted Three-Body Problem (RTBP) are given).

2.1 The N-body problem

The *n-body problem* is the generalization of the *two-body problem* in describing the resulting gravitational influence on a body generated by n other bodies according with the following generic expression of the gravitational force F_i acting on the *i-th* body of the system

$$\mathbf{F}_i = m_i \ddot{\mathbf{R}}_i = \sum_{j=1, j \neq i}^N \mathbf{F}_{ij} = \mathbf{F}_1 + \mathbf{F}_2 + \cdots + \mathbf{F}_j + \cdots + \mathbf{F}_N \quad (2.1)$$

Each gravitational force acting on the *i-th* body follows the equation of the Newton's Gravity Force

$$\mathbf{F}_{ij} = -G \frac{m_i m_j}{r_{ij}^2} \frac{\mathbf{r}_{ij}}{r_{ij}} \quad (2.2)$$

where $G = 6.67 \times 10^{-5} \frac{\text{km}^3}{\text{s}^2 \text{kg}}$ is the gravitational constant.

If we want to refer all the distances implied in the equations 2.1 and 2.2 to the central body of the system (this being the Sun, the Earth or whatever) we can describe the distance between each j -th body and the i -th body as a difference of distances between the two bodies and the central one as follows

$$r_{ij} = \|\mathbf{R}_i - \mathbf{R}_j\| \quad (2.3)$$

so the Newton's Gravity expression changes as follows.

$$\mathbf{F}_{ij} = -G \frac{m_i m_j}{\|\mathbf{R}_i - \mathbf{R}_j\|^2} \frac{\mathbf{R}_i - \mathbf{R}_j}{\|\mathbf{R}_i - \mathbf{R}_j\|} \quad (2.4)$$

If we sum together all the forces acting on the i -th body and we compare the equation obtained in this way with the expression of the resultant force acting on the i -th body written accordingly with the second Newton's law of dynamics we get, dividing both sides of the equation by the mass of the i -th body

$$\ddot{\mathbf{R}}_i = \sum_{j=1, j \neq i}^N \left[-G \frac{m_j}{\|\mathbf{R}_i - \mathbf{R}_j\|^2} \frac{\mathbf{R}_i - \mathbf{R}_j}{\|\mathbf{R}_i - \mathbf{R}_j\|} \right] \quad (2.5)$$

that is the equation of the acceleration the i -th body feels because of the action of all the other bodies in the system in relation with the inertial reference frame centered in the central body of the system.

The equation 2.5 depends on the distances between each j -th body and the central one so if we consider their motion we have to integrate this equation along with all the second order differential equation describing the motion of each j -th body. However this problem does not have any analytical solution so we have to take numerical methods into consideration or to apply simplified methods such as the *patched-conics method* at least in the early stage of the project of the desired trajectory.

2.2 The two-body problem

The *two-body problem* comes as a result of the integration of some simplifying assumptions to the n-body model:

1. The bodies are spherically symmetric so their masses can be considered to be concentrated in their centers;
2. The only forces acting in the model are the gravitational forces that act along the line joining the center of the planets involved;

2.2.1 The equation of the relative motion

All the evaluations discussed here are referred to an inertial reference frame even though in reality the best we can define is a quasi-inertial reference frame [5].

If we consider two bodies, \mathbf{M} and \mathbf{m} , in a non-rotating reference frame defined by three rectangular Cartesian coordinates (\mathbf{X}' , \mathbf{Y}' , \mathbf{Z}') having their origin in the \mathbf{M} body while we put the origin of a rotating reference frame defined by rectangular Cartesian

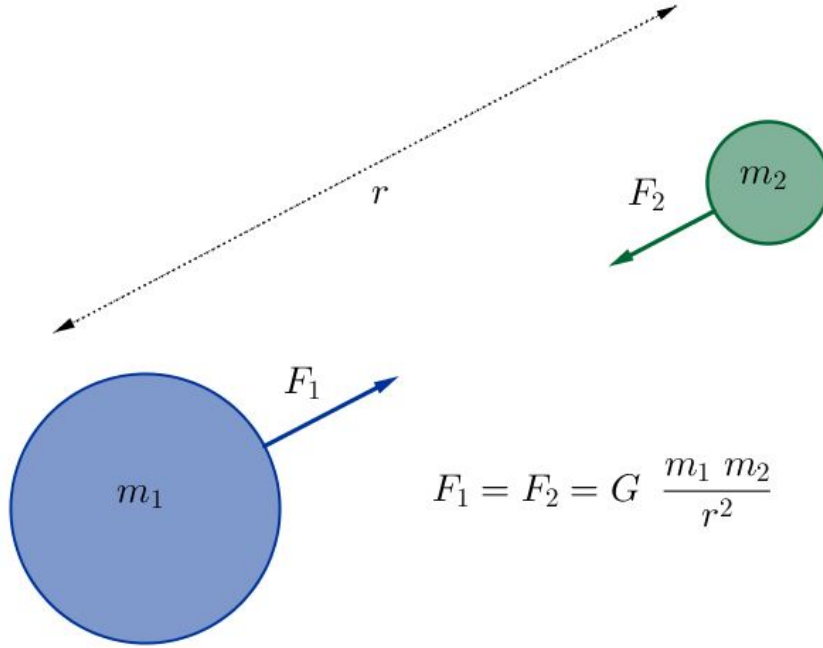


Figura 2.1: Gravitational interaction between two bodies m_1 and m_2

coordinates $(\mathbf{X}, \mathbf{Y}, \mathbf{Z})$ in the \mathbf{m} body we can define their distances in the $(\mathbf{X}', \mathbf{Y}', \mathbf{Z}')$ reference frame as

$$r = r_m - r_M \quad (2.6)$$

where r_M and r_m are the distances of the \mathbf{M} and the \mathbf{m} bodies from the origin of the $(\mathbf{X}', \mathbf{Y}', \mathbf{Z}')$ reference frame.

If we apply the Newton second law to both the bodies we will get, because of the assumptions previously made,

$$m\ddot{r}_m = -\frac{GMm}{r^2} \frac{\mathbf{r}}{r} \quad (2.7)$$

and

$$M\ddot{r}_M = \frac{GMm}{r^2} \frac{\mathbf{r}}{r} \quad (2.8)$$

so simplifying both the sides of both equations and adding them together we can find the total acceleration applied on both bodies simultaneously

$$\ddot{\mathbf{r}} = -\frac{G(M+m)}{r^3} \mathbf{r} \quad (2.9)$$

that is the equation of the relative motion for the two-body problem.

If we want to study the motion of a satellite or a probe orbiting around a planet or a moon we would be able to assume that the \mathbf{m} body has a neglectable mass contribution if compared with the one given by the \mathbf{M} body so $M+m \simeq M$ and the eq.2.9 can be rewritten as follows

$$\ddot{\mathbf{r}} + \frac{\mu}{r^3} \mathbf{r} = 0 \quad (2.10)$$

where $\mu = GM$ is the *gravitational parameter* and depends on the considered central body of the system.

body	μ $\frac{km^3}{s^2}$
Earth	398600
Moon	4921
Sun	1.32712 10^{11}
Mercury	22032
Venus	324859
Mars	42828
Jupiter	126686534
Saturn	37931187
Uranus	5793939
Neptune	6836529

Tabella 2.1: Gravitational parameter (μ) for the main bodies of the Solar Systems

2.2.2 Constants of motion

As it is more deeply discussed in [5] we can prove that in such a dynamical model there are some physical properties that are associated with quantities that are constant along the orbit. These quantities allow many calculation such as the ones regarding maneuvers from an orbit to another to be made in order to solve eq.2.10 when we want to calculate positions or velocities.

Along an orbit in the two-body model its *mechanical energy* is constant and can be described through the following equation

$$E = \frac{V^2}{2} - \frac{\mu}{r} \quad (2.11)$$

where the term $\frac{V^2}{2}$ stands for the *kinetic energy per mass unit* of the orbiting body while the term $\frac{\mu}{r}$ is the *potential energy for mass unit* term that, because of the convention of setting the reference point for potential energy at the infinity (in order to nullify the constant of integration c), will always be negative. It is important to point out that, apart from circular orbits, the distance between the two bodies always changes and so does the potential energy. Conservation of the total mechanical energy implies that in such cases the loss of potential energy will result in a gain of kinetic energy and vice versa and so therefore the modulus of the velocity vector will always change along the orbit (as Kepler's second law points out).

Another constant quantity along an orbit is the *specific angular momentum*, \mathbf{h} (the angular momentum for mass unit). It is defined as the cross product between the position vector \mathbf{r} and the velocity vector \mathbf{v}

$$\mathbf{h} = \mathbf{r} \wedge \mathbf{v} \quad (2.12)$$

so \mathbf{h} is always perpendicular to both \mathbf{r} and \mathbf{v} that define a plane and therefore we can conclude that the orbital plane never changes because the direction of \mathbf{h} itself never does.

These quantities, because of their being constant along the orbit, allow eq.2.10 to be integrated in order to obtain the expression of the position of the orbital body in relation to the central one that can be proven, as it is done in [5] and others, to be the following

$$r = \frac{h^2/\mu}{1 + (B/\mu) \cos \nu} \quad (2.13)$$

where B is the vector constant of integration.

2.3 The reference frame

Every trajectory of a body or spacecraft in space has to be described inside of a reference frame that is defined through a point called *center* that is the origin of its axis and a plane containing the x-axis and y-axis of the system (so therefore the z-axis is always perpendicular to that). They can be assumed as *quasi-inertial* or *non-inertial* according with the presence or the absence of any relative acceleration between the bodies present inside the system (such as the *Coriolis* acceleration).

The system adopted for this thesis is the heliocentric-ecliptic with a Cartesian set of coordinates for the calculations that with the proper rotation matrix can be converted into a heliocentric-ecliptic perifocal system where information given by the Ephemerides generated by NASA through the Horizon System that relies upon the J2000 reference system. In particular the Ephemerides used for this thesis are from the DE431 series.

Here follows a more deep description of those two reference frames used along with an analysis of the various sets of orbital parameters that can be used (noting that for the calculations the Keplerian orbital parameters have been used thanks to the relationship they have with the Cartesian set of coordinates).

2.3.1 The Heliocentric-Ecliptic reference frame

In this subsection we will describe the *heliocentric reference frame* used to describe all the distances and velocities used in the calculations.

The Heliocentric reference frame has its center in the Sun, its fundamental plan in the *Ecliptic Plan* and has the positive direction of its *z-axis* oriented towards the celestial hemisphere containing the star *Polaris*. The *x-axis* is determined by a line joining the center of the Sun and the center of the Earth during the first day of Spring (during the *Vernal Equinox* when the Earth, seen from the Sun, is in the Aries constellation). It is worth remembering that the equinox line is not aligned with the line of the absides because of a perturbation process of this line, called *precession of the equinox line* caused by the influence of the mass of the Moon and of the other planets on the Earth that causes each equinox to be anticipated by one day each 71.63 years (and once every 13000 years we have the inversion of the seasons).

For the motion of the Earth around the Sun in the Heliocentric-Ecliptic reference frame we can define more than one revolution period:

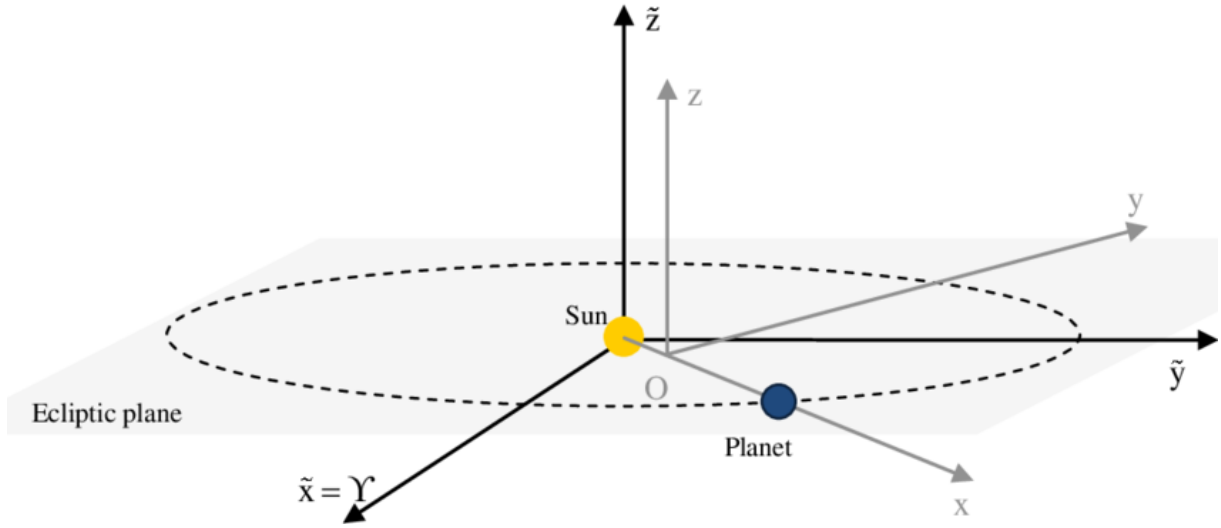


Figura 2.2: Heliocentric-Ecliptic reference frame (black axes) [20]

1. Sidereal year: it is measured between two consecutive passages of the Earth in front of one of the background stars and it is 365 days, 6 hours, 9 minutes and 9 seconds long;
2. Tropic year: it is measured between two consecutive passages through the equinox line and it is 365 days, 5 hours, 48 minutes and 46 seconds long;

2.3.2 The perifocal reference frame

The perifocal reference frame is defined as a reference frame centered into a focus of the orbit we are studying in it (typically, in the case of a closed orbit, we choose the focus where the central body is, so considering an heliocentric orbit the Sun will occupy the center of the system) and has the x-axis and the y-axis oriented as the vectors \hat{p} and \hat{q} referred to the directions of the periaxis and of the semilatus rectum of the orbit respectively while the third axis, called \hat{w} , follows the direction that is parallel to the angular momentum \mathbf{h} one.

Given the calculation operated in this thesis it is crucial to use the perifocal reference frame as an intermediate one to switch from the Keplerian elements used to describe the starting and the final orbit of the maneuver we want to optimize to the Cartesian components of the position \mathbf{r} and velocity \mathbf{v} vectors of the Earth and the other bodies orbiting the Sun (spacecraft included). The angle that determines the position of the body along its orbit is the *true anomaly*, ν , that as a consequence determines also the components of the position and velocity vectors in relation with the main directions \hat{p} and \hat{q} inside of the orbital plane.

$$\mathbf{r} = r \cos \nu \hat{p} + r \sin \nu \hat{q} \quad (2.14)$$

$$\mathbf{v} = (\dot{r} \cos \nu - r \dot{\nu} \sin \nu) \hat{p} + (\dot{r} \sin \nu + r \dot{\nu} \cos \nu) \hat{q} \quad (2.15)$$

In this reference frame those vectors (eq.2.14 and 2.15) are linked through a relationship regarding their internal product that can be proved (as in [5]) to be

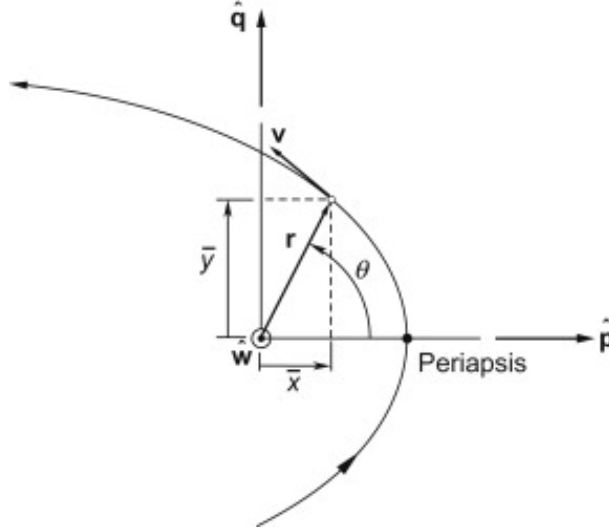


Figura 2.3: Perifocal plane [12]

$$\mathbf{r} \cdot \mathbf{v} = rv \sin \phi \quad (2.16)$$

so their internal product depends on the *azimuth angle* and if the orbiting body is moving towards its apoaxis it will be positive (negative if it is moving towards its periaxis instead).

The rotation of a reference frame

It is possible to switch from a reference frame to another one through a sequence of elementary rotations each one performed around the proper axis finding this way the relationship between each defining vector of the axis of a reference frame with the ones of the final one.

In this case we can rotate the heliocentric-ecliptic reference frame into the perifocal one through a sequence of 3 elementary rotation around an axis according with the sequence 3-1-3 (the first and the last rotation are performed around the z-axis while the first one is performed around the x-axis) called *Eulerian rotation*. We obtain a rotation matrix L_i from each rotation and their matricial product gets us the whole rotation matrix L (in order to switch back from the perifocal to the heliocentric reference frame we have to transpose the whole rotation matrix L^T).

Each rotation matrix has a 3x3 dimension and each term is the inner product of each couple of defining vectors of each reference system that is equal (having the defining vectors magnitude of 1) to the cosine of the rotation angle (the three angles of the sequence are the Right Ascension of the Ascending Node (RAAN), the inclination i and the argument of periaxis ω)

$$L_1^T = \begin{bmatrix} \hat{I} \cdot \hat{n} & \hat{J} \cdot \hat{n} & \hat{K} \cdot \hat{n} \\ \hat{I} \cdot \hat{m} & \hat{J} \cdot \hat{m} & \hat{K} \cdot \hat{m} \\ \hat{I} \cdot \hat{k} & \hat{J} \cdot \hat{k} & \hat{K} \cdot \hat{k} \end{bmatrix} = \begin{bmatrix} \cos \Omega & \sin \Omega & 0 \\ -\sin \Omega & \cos \Omega & 0 \\ 0 & 0 & 1 \end{bmatrix} \quad (2.17)$$

$$L_2^T = \begin{bmatrix} \hat{n} \cdot \hat{n} & \hat{m} \cdot \hat{n} & \hat{k} \cdot \hat{w} \\ \hat{n} \cdot \hat{l} & \hat{m} \cdot \hat{l} & \hat{k} \cdot \hat{w} \\ \hat{n} \cdot \hat{k} & \hat{m} \cdot \hat{k} & \hat{k} \cdot \hat{w} \end{bmatrix} = \begin{bmatrix} 1 & 0 & 0 \\ 0 & \cos i & \sin i \\ 0 & -\sin i & \cos i \end{bmatrix} \quad (2.18)$$

$$L_3^T = \begin{bmatrix} \hat{n} \cdot \hat{p} & \hat{l} \cdot \hat{p} & \hat{w} \cdot \hat{p} \\ \hat{n} \cdot \hat{q} & \hat{l} \cdot \hat{q} & \hat{w} \cdot \hat{q} \\ \hat{n} \cdot \hat{w} & \hat{l} \cdot \hat{w} & \hat{w} \cdot \hat{w} \end{bmatrix} = \begin{bmatrix} \cos \omega & \sin \omega & 0 \\ -\sin \omega & \cos \omega & 0 \\ 0 & 0 & 1 \end{bmatrix} \quad (2.19)$$

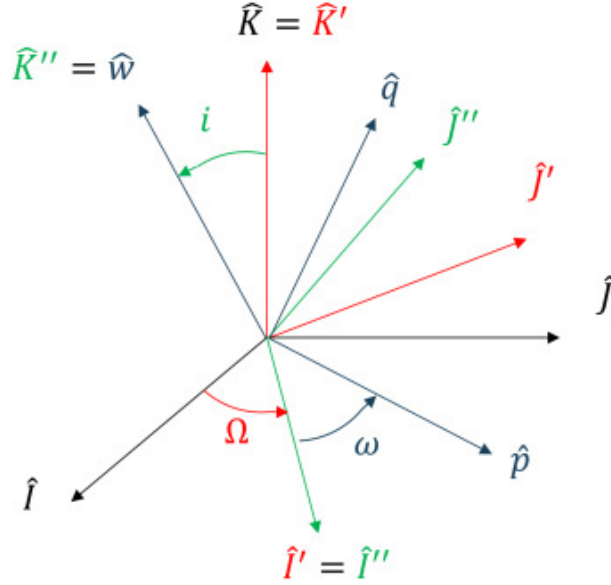


Figura 2.4: Rotation from Cartesian to perifocal reference frame [12]

As a result we can get the whole rotation matrix L^T

$$\mathbf{r}_{pqw} = L_3^T L_2^T L_1^T \mathbf{r}_{ijk} = L^T \mathbf{r}_{ijk} \quad (2.20)$$

while the reverse rotation is the following

$$\mathbf{r}_{ijk} = L_1 L_2 L_3 \mathbf{r}_{pqw} = L \mathbf{r}_{pqw} \quad (2.21)$$

2.3.3 Ephemerides and Julian Day

In order to calculate distances between bodies within the Solar System we used the *Ephemerides* that are tables that collect values referred to multiple astronomical variables, such as orbital parameters and coordinates of every body inside the Solar System (and distances between them and the Sun as well), as they can be measured throughout time by observing the motion of planets, comets and asteroids. They are kept and updated by NASA's Jet Propulsion Laboratory (JPL) and they are referred to the quasi-inertial J2000 system.

In order to describe and express positions of celestial bodies Ephemerides show the following set of values for each celestial body for each day of the Gregorian Calendar:

- *Julian Day* at 00:00 of the considered day;

- *Sideral time* at 00:00 GMT;
- the error between time calculations made by using the *average Sun* and the *real Sun*;

In particular the Julian Day (JD), as explained in [5], is a way to measure time rationalizing the keeping of calendar across multiple centuries and calendars. It is a separate calendar that counts astronomical days numbering them consecutively from an epoch that was chosen to be sufficiently far in the past to precede the current historical period. It starts at 0 defined to be *January 1st, 4713 b.C. @12:00 UTC*. Its cycle lasts 7800 years as a result of the sum of three different cycles:

- 15 years for the *Indiction cycle* (a cycle that was used especially during the Medieval Era for taxation reasons);
- 19 years for the *Metonic cycle* (the cycle of the lunisolar calendar that is aimed at keeping lunar and solar phases synchronized);
- 28 years for the *repetition of week and month days cycle*;

For each date (expressed in D, days, M, months, Y, years) we can calculate its Julian Day using the proper equation (which equation to use depends on whether we are using the Gregorian Calendar or the Julian one). In case we are using the Julian Calendar the equation is:

$$JD = D + fl \left[\frac{153m + 2}{5} \right] + 365y + fl \left[\frac{y}{4} \right] - 32083 \quad (2.22)$$

while if we are using the Gregorian Calendar the equation is:

$$JD = D + fl \left[\frac{153m + 2}{5} \right] + 365y - fl \left[\frac{y}{100} \right] + fl \left[\frac{y}{400} \right] + fl \left[\frac{y}{4} \right] - 32045 \quad (2.23)$$

where the coefficients a, y and m are obtained through D, M and Y

$$a = fl \left[\frac{12 - M}{12} \right] \quad (2.24)$$

$$y = Y + 4800 - a \quad (2.25)$$

$$m = M + 12a - 3 \quad (2.26)$$

We can also use the *Modified Julian Day* if we reduce the Julian Day by 2400000.5 removing all the days until *November 16th 1858 @0:00 UTC*.

This can help to evaluate differences in positions using the J2000 system (so we need to evaluate the days passed since January 1st 2000 @12:00 UTC in terms of Julian Day) through the evaluation of α_G

$$\alpha_G = \alpha_{G_0} + \omega_{Earth}d + 0.0003875t^2 \quad (2.27)$$

where ω_{Earth} , the Earth angular velocity, is equal to $7.29 \cdot 10^{-5} \frac{rad}{s}$ (or 360.93564736629° per day), t represents the number of centuries passed since January 1st 2000 @12:00 where α_{G_0} is evaluated (it being equal to 280.46061837°)

$$t = \frac{d}{365.2425 \cdot 100} \quad (2.28)$$

and d is the difference between JD evaluated at the time present and the one at January 1st 2000 @12:00 UTC.

2.3.4 Classical orbital parameters

Classical (or *Keplerian*) orbital parameters are useful to describe every orbit as sections of conics. If we want to describe an orbit in a 3D reference frame as the one we previously introduced we need 7 parameters that can be defined as in figure 2.5

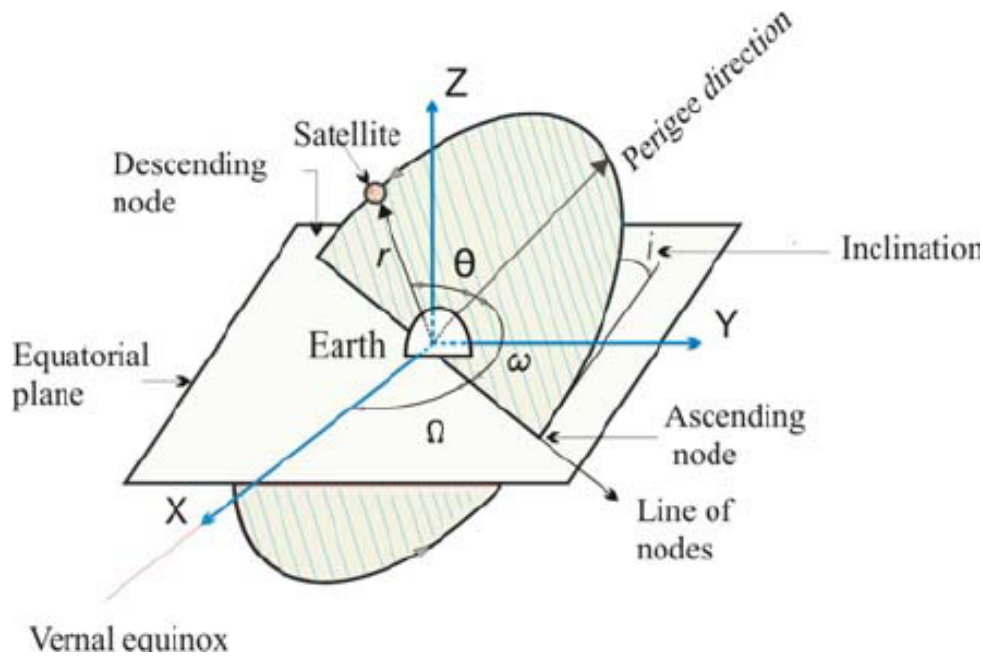


Figura 2.5: Classical orbital parameters [34]

parameter	name
a	semi-major axis
p	semilatus rectum
e	eccentricity
ω	argument of periaxis
ν	true anomaly
Ω	RAAN
i	inclination of the orbital plane

Tabella 2.2: Keplerian orbital parameters

In the table 2.2 there are some parameters (the last 4 of them) that are typical for the description, if added to the 3 previously listed in it, of every 3D orbit. Those can be defined as follows:

- ω : it is the angle formed by the *line of the nodes* and the direction of the periaxis;
- ν : it is the angle swept by the position vector in respect to the direction of the periaxis during the revolution of the orbiting body around the central one;
- Ω : it is the angle formed by the *x-axis* of the reference frame we describe the orbit in and by the *line of the nodes*;
- i : it is the angle formed by the *z-axis* of the reference frame we describe the orbit in and by the direction of the angular momentum of the orbiting body;

The other three parameters will be defined later on in this section.

According with its definition, a conic is the *locus* of the points on a plane whose fraction calculated for their distance from a point called *focus* and a reference straight-line called *director* is constant. This fraction is called *eccentricity* of the conic and therefore of the orbit itself.

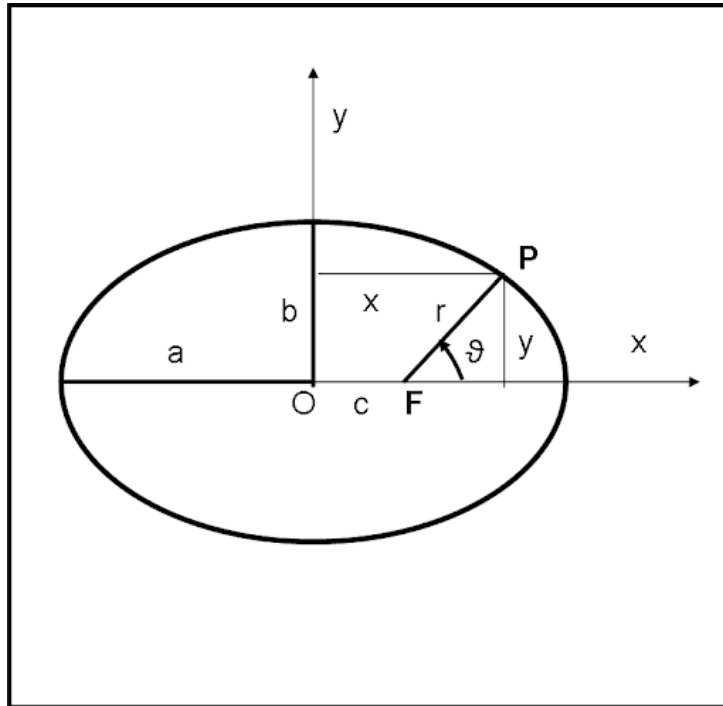


Figura 2.6: Structure of an elliptical orbit [54]

$$e = \frac{r}{d} \quad (2.29)$$

Orbits can be *open* or *closed* depending on the value of the total mechanical energy that defines them (positive for open conics and negative for closed ones) and those characteristics impact on the values of the orbital parameters themselves.

If we consider the geometrical structure of an elliptical orbit we can define some elements:

- $a = \text{semi-major axis}$ of the orbit;
- $b = \text{semi-minor axis}$ of the orbit;
- $c = \text{inter-focal distance}$ of the orbit, describing the distance between the two points called *focus* of the orbit;

It is possible to prove, as in [5], that the following expressions hold

$$e = \frac{c}{a} \tag{2.30}$$

$$a^2 = b^2 + c^2 \tag{2.31}$$

and given the equation that geometrically describes an ellipse

$$\frac{x^2}{a^2} + \frac{y^2}{b^2} = 1 \tag{2.32}$$

we get expressions that relate the position of a body along its orbit with the orbital parameters themselves

$$e = \frac{r_a - r_p}{r_a + r_p} \tag{2.33}$$

$$p = a(1 - e^2) \tag{2.34}$$

where r_a and r_p are the distances of the orbiting body from the central body at its furthest point (the so called *apoaxis*) and at its closest (the so called *periaxis*) and p is the *semilatus rectum* that represents the distance between the orbiting body when its true anomaly is $\nu = 90^\circ$ and the central one.

From those equations we can obtain the expression of the position of the body along the elliptical orbit as a particular case of 2.13:

$$r = \frac{p}{1 + e \cos \nu} \tag{2.35}$$

where

$$p = \frac{h^2}{\mu} \tag{2.36}$$

and h being the angular momentum of the orbit represented by the following expression

$$h = \sqrt{\mu a(1 - e^2)} \tag{2.37}$$

while the total mechanical energy of the orbit is represented by the following expression that is valid for every type of orbit.

$$E_g = -\frac{\mu}{2a} \tag{2.38}$$

For elliptical orbit we can also evaluate the *flight-path angle* ϕ , the angle generated by the velocity vector with the direction perpendicular to the position vector joining the orbiting body with one of the two foci of the orbit (the one containing the central body) whose change at every point along the orbit allows the angular momentum vector to be constant as for eq.2.12, that [5] proves to be described by the following expression

$$\tan \phi = \frac{e \sin \nu}{1 + e \cos \nu} \quad (2.39)$$

and proves also to be equal in every point of the orbit to ϕ' , the *flight-path angle* measured with respect to the other focus of the elliptical orbit.

All of the aforementioned orbital parameters can be obtained through the position and the velocity vectors (\mathbf{r} and \mathbf{v}):

- Eccentricity can be defined, comparing eq.2.13 with eq.2.35, as follows (where the B vector can be defined isolating it from the eq.2.13)

$$e = \frac{B}{\mu} = \frac{\mathbf{v} \wedge \mathbf{h}}{\mu} - \frac{\mathbf{r}}{\|\mathbf{r}\|} \quad (2.40)$$

where $\mathbf{h} = \mathbf{r} \wedge \mathbf{v}$;

- Argument of periaxis is the angle defined, as shown in figure 2.5, by the direction of the *line of the nodes* and the direction of the *periaxis* so we can define it with the following expression

$$\mathbf{n} \cdot \mathbf{p} = \|\mathbf{n}\| \|\mathbf{p}\| \cos \omega \quad (2.41)$$

that can lead us to define ω more straightforwardly as

$$\omega = \arccos(\hat{\mathbf{n}} \cdot \hat{\mathbf{p}}) \quad (2.42)$$

- True anomaly is defined by the direction of the *line of the nodes* and by the direction of the position vector \mathbf{r} of the orbiting body along its trajectory so knowing from figure 2.5 that

$$\mathbf{p} \cdot \mathbf{r} = \|\mathbf{p}\| \|\mathbf{r}\| \cos \nu \quad (2.43)$$

we can get the new definition of ν

$$\nu = \arccos(\hat{\mathbf{r}} \cdot \hat{\mathbf{p}}) \quad (2.44)$$

- The RAAN Ω is defined, as it is shown in figure 2.5, by the x-axis of the chosen reference frame of coordinates and by the direction of the *line of nodes* so

$$\Omega = \arccos(\hat{\mathbf{I}} \cdot \hat{\mathbf{n}}) \quad (2.45)$$

- Inclination i is defined by the z-axis of the chosen reference frame of coordinates and by the *angular momentum vector* \mathbf{h} so

$$i = \arccos(\hat{\mathbf{k}} \cdot \hat{\mathbf{h}}) \quad (2.46)$$

where

$$\hat{\mathbf{h}} = \frac{\mathbf{h}}{\|\mathbf{h}\|} \quad (2.47)$$

If we then consider circular orbits, a simplified kind of elliptical orbit where $c = 0$ (the two foci collapse in a single point called *center*), we can easily define some of their main orbital parameters. In fact according with 2.30 we get that for these particular orbits $e = 0$.

If we nullify the total mechanical energy of the orbit we get a parabolic orbit where, by definition, the distances between the only *focus* of the orbit and the *director* line are equal. This aspect, according with 2.29, shows how $e = 1$ while $a = \infty$ and $e = \infty$.

The last kind of orbits we examine in this section is the hyperbolic orbit that is characterized by $e > 1$ and $e = \frac{1}{\cos \phi}$ where ϕ is the angle represented as ρ in fig. 2.7.

Those parameters can cause some issues for some particular orbits such as:

- $i = 0$: If an orbit lies on the fundamental plane of the reference frame it is studied into we do not have a *line of nodes* anymore so we do not have any Ω angle that is therefore non defined;
- $e = 0$: It consists of a circular orbit where *periaxis* and *apoaxis* are not defined and so therefore ω is non defined;
- $i = 0$ and $e = 0$: For such orbits the angles Ω , ω and ν are not distinguishable so they can only be summed together to obtain the *true longitude* angle $l(t)$.

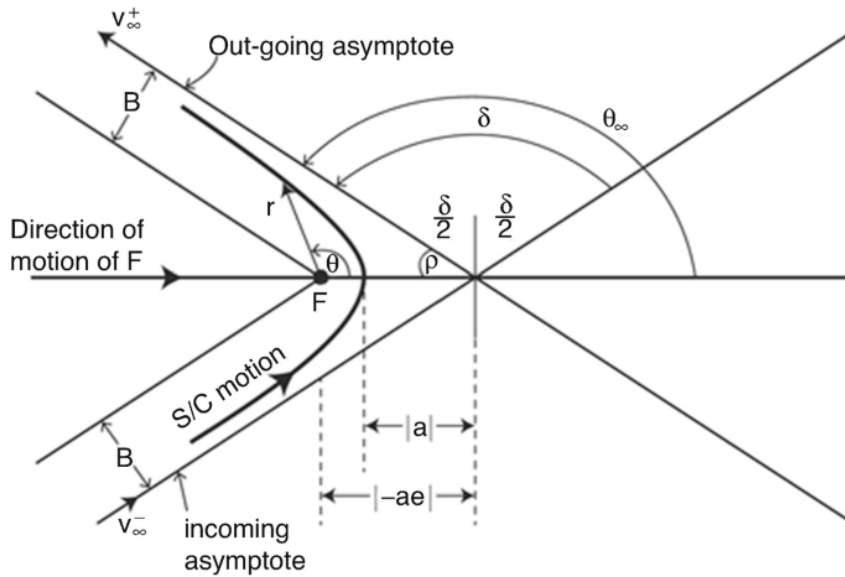


Figura 2.7: Hyperbolic orbit [21]

2.4 Equations of dynamics

In order to study the problem of space trajectories it is necessary to integrate over the time span of duration of the performed maneuver a set of Ordinary Differential Equations (ODEs) that describe the evolution of position, velocity and mass of the spacecraft as they are influenced by the central body it is moving around and by the performance of the thruster and of the propellant used.

$$\begin{aligned}
 \frac{d\mathbf{r}}{dt} &= \mathbf{V} \\
 \frac{d\mathbf{V}}{dt} &= \mathbf{g} + \frac{\mathbf{T}}{m} + \frac{\mathbf{L}}{m} + \frac{\mathbf{D}}{m} + \mathbf{a}_p \\
 \frac{dm}{dt} &= -\frac{T}{c}
 \end{aligned} \tag{2.48}$$

where the vectors \mathbf{T} , \mathbf{L} and \mathbf{D} represent the thrust generated, the lift and the drag respectively (the last two of them are neglected being the studied orbits far from Earth and its atmosphere) and the \mathbf{g} term represents the gravitational acceleration generated by the central body (in this case, the Sun) on the spacecraft itself and is described by the relation obtained through isolating the acceleration term $\ddot{\mathbf{r}}$ in eq.2.10.

2.4.1 Equations of dynamics in Cartesian coordinates

If we consider all the Cartesian components for the position and velocity vectors (\mathbf{r} and \mathbf{V}) we can write the equation of the dynamic for each of their component so the equations have the following form (without considering any lift, drag or perturbation)

$$\begin{aligned}
 \frac{dx}{dt} &= \mathbf{V}_x \\
 \frac{dy}{dt} &= \mathbf{V}_y \\
 \frac{dz}{dt} &= \mathbf{V}_z \\
 \frac{d\mathbf{V}_x}{dt} &= -\frac{\mu}{r^{3/2}}x + \frac{\mathbf{T}}{m} \frac{\lambda_{v_x}}{\lambda_V} \\
 \frac{d\mathbf{V}_y}{dt} &= -\frac{\mu}{r^{3/2}}y + \frac{\mathbf{T}}{m} \frac{\lambda_{v_y}}{\lambda_V} \\
 \frac{d\mathbf{V}_z}{dt} &= -\frac{\mu}{r^{3/2}}z + \frac{\mathbf{T}}{m} \frac{\lambda_{v_z}}{\lambda_V} \\
 \frac{dm}{dt} &= -\frac{T}{c}
 \end{aligned} \tag{2.49}$$

where λ_V is the *primer vector* whose components are the velocity components costates

$$\lambda_V = \{\lambda_{v_x}, \lambda_{v_y}, \lambda_{v_z}\}^T \tag{2.50}$$

and λ_V is its magnitude

$$\lambda_V = \sqrt{\lambda_{v_x}^2 + \lambda_{v_y}^2 + \lambda_{v_z}^2} \tag{2.51}$$

2.5 Electrical propulsion

Space propulsion is focused on generating a certain amount of power through one of the available sources such as chemical reactions (like the one involving liquid chriogenic Hydrogen and liquid chriogenic Oxygen that is used to push rockets into space defeating the pull of gravity during the lift-off phase of every mission), electrical power or nuclear

reactions (actually we do not have any thrusters ready-to-use that can rely on such source of power, NASA is working on them but only at a conceptual design level [18]) to transform it into kinetical power for a propellant that accelerates while it cools down flowing through a nozzle generating thrust for the spacecraft as it slows down.

The choice of the source of power heavily depends on the type of mission we want to accomplish. In this case of asteroid retrieval a very long-lasting source of thrust will be required so we will need very high *specific impulse*, I_{sp} ,

$$I_{sp} = \frac{I_t}{m_p g_0} = \frac{T}{\dot{m}_p g_0} = \frac{c}{g_0} = \Delta t \quad (2.52)$$

to get a thruster that is able to provide high *effective exhaust velocity*, c , for long time. This means that the necessary *total impulse*, I_t , will be very high with the necessity of keeping the *propellant mass*, m_p , as low as possible. Considering that

$$T = m_p g_0 \quad (2.53)$$

we can conclude that in order to have high I_{sp} because of the high duration of the mission we will have a limit on the maximum thrust we will be able to generate. This means that the source of power we will need to use is the electrical one.

The electrical power can be generated through an external source (such as the power radiated by a nearby star collected with panels) or an internal source (such as a battery) to transform a fraction of it into internal energy for the propellant (the higher the efficiency of the electrical power system, the higher the fraction of it that will be given to the propellant as internal energy). We can easily show that the high internal power given to the propellant brings to high velocity of the propellant at the nozzle exit, c , as it is stated in the following equation

$$c = \sqrt{\frac{2\eta P_E}{\dot{m}_p}} = \frac{2\eta P_E}{T} \quad (2.54)$$

so once more we get that to generate high c and so therefore high I_{sp} we need to limit the thrust generated, T (this will implicitly help to reduce the necessary propellant mass flow). This is why we cannot use them to launch rockets into Earth orbit, however these characteristics make such propulsion ideal to perform orbital maneuvers.

A typical way to use electrical thrusters is pushing the spacecraft by performing long continuous burns to change different orbital parameters (we will be able to change a parameter or another depending mainly on the direction of the generated thrust in relation to the direction of the actual velocity of the spacecraft) rather than performing quasi-impulsive maneuvers typical for chemical thrusters. Because of the long duration of the burns used for such maneuvers we cannot describe them through Hohmann or Lambert's formulation because of them being used specifically for impulsive maneuvers, so we need to apply the Edelbaum's formulation for single-revolution and for multiple-revolution maneuvers in order to have an analytical formulation of the problem or alternatively we can simply integrate the aforementioned equations of the dynamics using the value of the given thrust inside of them.

2.6 Lagrangian Points

Lagrangian points are places in space whose coordinates can be defined in the context of a *three-body system*. By its own definition, if we consider a system composed of two main bodies whose masses are m_1 and m_2 (we can define the μ factor as it follows

$$\mu = \frac{m_1}{M} \quad (2.55)$$

where M is the sum of m_1 and m_2) orbiting in circular orbits around the common center of gravity (if we define a *circular* three-body system) we can introduce a third body whose mass is neglectable ($m \ll m_1, m_2$, so therefore it can be considered *restricted*) and describe its motion through the equation that equals the sum of all the mechanical accelerations m is subjected to with the sum of the gravitational accelerations the two bodies generate on it

$$\ddot{\mathbf{r}} + \boldsymbol{\omega} \wedge (\boldsymbol{\omega} \wedge \mathbf{r}) + 2 \boldsymbol{\omega} \wedge \dot{\mathbf{r}} = \frac{1}{m} (\mathbf{F}_1 + \mathbf{F}_2) \quad (2.56)$$

where the first three terms of the left-hand side of the equation are the inertial term, the centripetal term and the Coriolis term respectively, \mathbf{F}_1 and \mathbf{F}_2 are the gravitational forces by m_1 and m_2 on m described by 2.2 and the distances between m and m_1 and m_2 respectively are given by

$$|r_1| = \sqrt{[x - \mu R]^2 + y^2 + z^2} \quad (2.57)$$

$$|r_2| = \sqrt{[x - (1 - \mu) R]^2 + y^2 + z^2} \quad (2.58)$$

where the coordinates $[x, y, z]^T$ are defined in the synodic reference frame centered in the common center of gravity of the system as in fig. 2.8.

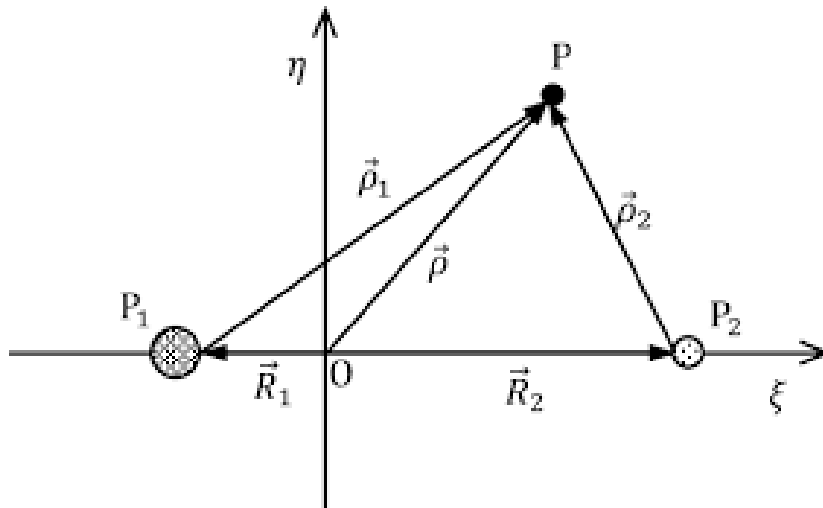


Figura 2.8: The synodical reference frame for a three body problem [42]

So knowing the three components for \mathbf{r} , $\dot{\mathbf{r}}$ and $\boldsymbol{\omega}$ we can calculate all the components for the accelerations that play a role in eq.2.56 obtaining the equations of motion (one for each main direction of the system)

$$\begin{cases} \xi'' - \xi - 2\eta' &= -(1-\mu)\frac{\xi+\mu}{\rho_1^3} - \mu\frac{\xi-(1-\mu)}{\rho_2^3} \\ \eta'' - \eta + 2\xi' &= -(1-\mu)\frac{\eta}{\rho_1^3} - \mu\frac{\eta}{\rho_2^3} \\ \zeta'' &= -(1-\mu)\frac{\zeta}{\rho_1^3} - \mu\frac{\zeta}{\rho_2^3} \end{cases} \quad (2.59)$$

where $[\xi, \eta, \zeta]^T$ are the adimensional coordinates (resulting from the division of $[x, y, z]^T$ by R , the distance between the m body and the center of gravity). These are 3 equations in 6 variables that can be turned into a system of 6 ODE in 6 variables ($[\xi', \eta', \zeta', \xi'', \eta'', \zeta'']^T$) for them to be numerically solved.

There are five points in the space of the system defined in fig. 2.8 where gravitational and centrifugal forces reach a state of equilibrium generating no acceleration on the body that orbits there so those are equilibrium points where all the components of the relative velocity $[\xi', \eta', \zeta']^T$ and of the relative acceleration $[\xi'', \eta'', \zeta'']^T$ are equal to zero so that every body that orbits there is motionless in respect with the reference frame. Those points are called *Lagrangian points* of the system and it is mathematically proven [34] that their position in relation with the two main bodies of the system is the one represented in fig. 2.9.

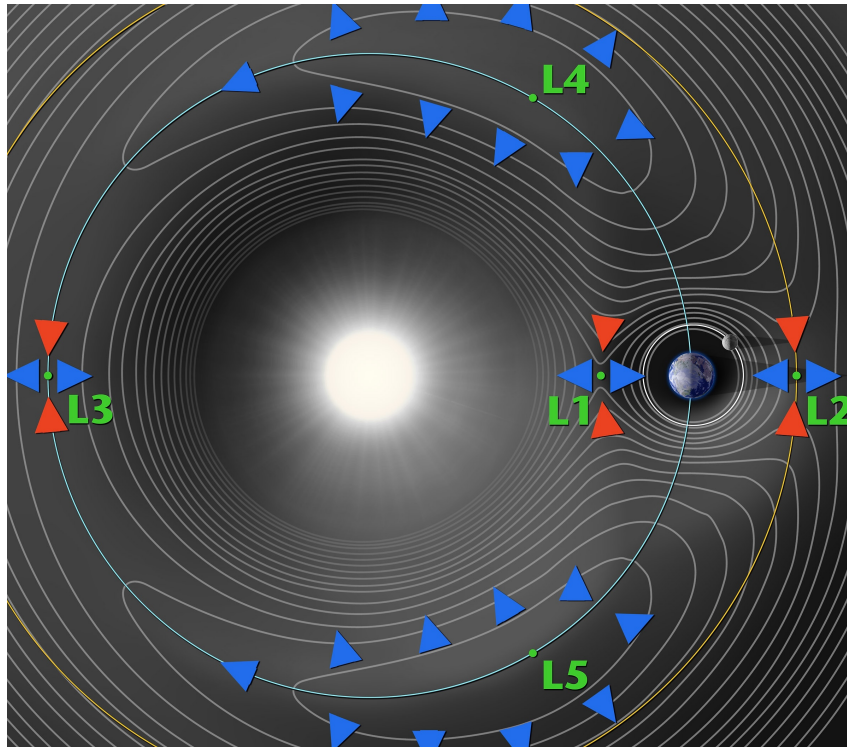


Figura 2.9: Position of the five Lagrangian points in a gravitational system of two main bodies m_1 and m_2 [15]

In order to find their coordinates in the synodic reference frame of the system we can define the *potential function* that in the three-body system can be described as follows

$$\mathcal{U} = \frac{1-\mu}{\rho_1} + \frac{\mu}{\rho_2} + \frac{1}{2}(\xi^2 + \eta^2) \quad (2.60)$$

so if we derive it in respect to the non-dimensional coordinates $[\xi', \eta', \zeta']^T$ and remembering that derivatives for ρ_1 and ρ_2 in respect to $[\xi, \eta, \zeta]^T$ are

$$\begin{bmatrix} \frac{\partial \rho_1}{\partial \xi} & \frac{\partial \rho_1}{\partial \eta} & \frac{\partial \rho_1}{\partial \zeta} \\ \frac{\partial \rho_2}{\partial \xi} & \frac{\partial \rho_2}{\partial \eta} & \frac{\partial \rho_2}{\partial \zeta} \end{bmatrix} = \begin{bmatrix} \frac{\xi + \mu}{\rho_1^3} & \frac{\eta}{\rho_1} & \frac{\zeta}{\rho_1} \\ \frac{\xi - (1 - \mu)}{\rho_2^3} & \frac{\eta}{\rho_2} & \frac{\zeta}{\rho_2} \end{bmatrix} \quad (2.61)$$

we get the following derivatives for \mathcal{U}

$$\begin{cases} \frac{\partial \mathcal{U}}{\partial \xi} = \xi - (1 - \mu) \frac{\xi + \mu}{\rho_1^3} - \mu \frac{\xi - (1 - \mu)}{\rho_2^3} \\ \frac{\partial \mathcal{U}}{\partial \eta} = \eta - (1 - \mu) \frac{\eta}{\rho_1^3} - \mu \frac{\eta}{\rho_2^3} \\ \frac{\partial \mathcal{U}}{\partial \zeta} = -(1 - \mu) \frac{\zeta}{\rho_1^3} - \mu \frac{\zeta}{\rho_2^3} \end{cases} \quad (2.62)$$

and if we move each linear term from the left to the right-hand side of (2.59) we can point out that the left-hand side of those equations will be the same as for 2.62 so we can equalize their respective right-hand sides obtaining what follows.

$$\begin{cases} \frac{\partial \mathcal{U}}{\partial \xi} = \xi'' - 2\eta' \\ \frac{\partial \mathcal{U}}{\partial \eta} = \eta'' + 2\xi' \\ \frac{\partial \mathcal{U}}{\partial \zeta} = \zeta'' \end{cases} \quad (2.63)$$

So if we nullify the right-hand side of the eqs.2.62 and 2.63 we are imposing the derivatives of the potential being equal to zero and we can find the coordinates of the Lagrangian points.

The first Lagrangian point is located along the line that links the centers of gravity of both the main bodies of the system and is between them (so that the sum of the non-dimensional distances of m_1 and m_2 , ρ_1 and ρ_2 , is equal to 1)

$$\begin{cases} \frac{\partial \mathcal{U}}{\partial \xi} = \xi - (1 - \mu) \frac{\xi + \mu}{\rho_1^3} - \mu \frac{\xi - (1 - \mu)}{\rho_2^3} = 0 \\ \frac{\partial \mathcal{U}}{\partial \eta} = \eta - (1 - \mu) \frac{\eta}{\rho_1^3} - \mu \frac{\eta}{\rho_2^3} = 0 \\ \rho_1 + \rho_2 = 1 \end{cases} \quad (2.64)$$

so if we choose one derivative and we add to it the third equation of the set we obtain the distance between the second main body and the first Lagrangian point (called L_1). We can do the same with the second Lagrangian point (L_2) that, as shown in fig. 2.9 is further from m_1 than m_2 so that $\rho_1 - \rho_2 = 1$, and with the third Lagrangian point (L_3) that is on the other side of m_1 (L_1 , L_2 and L_3 are located along the same line so they are called *co-linear* so that for all the three of them we have $\eta = 0$) so that $\rho_2 - \rho_1 = 1$. We can therefore obtain their distance ρ_2 from m_2 that in the context of the Heliocentric ecliptic system is the Earth (while m_1 represents the Sun), so the non-dimensional mass it should be used is $1 - \mu$.

$$\begin{cases} \rho_2(L_1) = \sqrt[3]{\frac{1 - \mu}{3}} \\ \rho_2(L_2) = \sqrt[3]{\frac{1 - \mu}{3}} \\ \rho_2(L_3) = 2 \end{cases} \quad (2.65)$$

The last two Lagrangian points (L_4 and L_5) are called *equatorial* and are located at the two intersections of the two circles centered in m_1 and m_2 respectively. They are both

the upper apex of two equatorial triangles having at the other two apexes m_1 and m_2 . If we consider both the derivatives of the potential function in relation with ξ and η equaled with zero (as in the first two equations of the set 2.64) we can calculate the expressions of the coordinates ξ and η for L_4 and L_5 .

$$\begin{cases} \xi(L_4) = \frac{1}{2} - \mu \\ \eta(L_4) = \frac{\sqrt{3}}{2} \end{cases} \quad (2.66)$$

$$\begin{cases} \xi(L_5) = \frac{1}{2} - \mu \\ \eta(L_5) = -\frac{\sqrt{3}}{2} \end{cases} \quad (2.67)$$

As we mentioned earlier in those Lagrangian points the potential function \mathcal{U} has a minimum point, however the equilibrium at the three co-linear Lagrangian points (L_1 , L_2 and L_3) is not stable, in fact very little perturbations can push the m body towards m_1 or m_2 because of their very deep potential hole (very close to m_1 and m_2 we have that \mathcal{U} goes to ∞ while the further we move from the main bodies of the system the more influence the term $(\xi^2 + \eta^2)$ from the (2.60) gets generating the circular *level lines* defining the lines along which the potential function has the same value). On the other hand the shape of the function \mathcal{U} is more flat close to L_4 and L_5 such that their equilibrium is stable as shown in fig. 2.10.

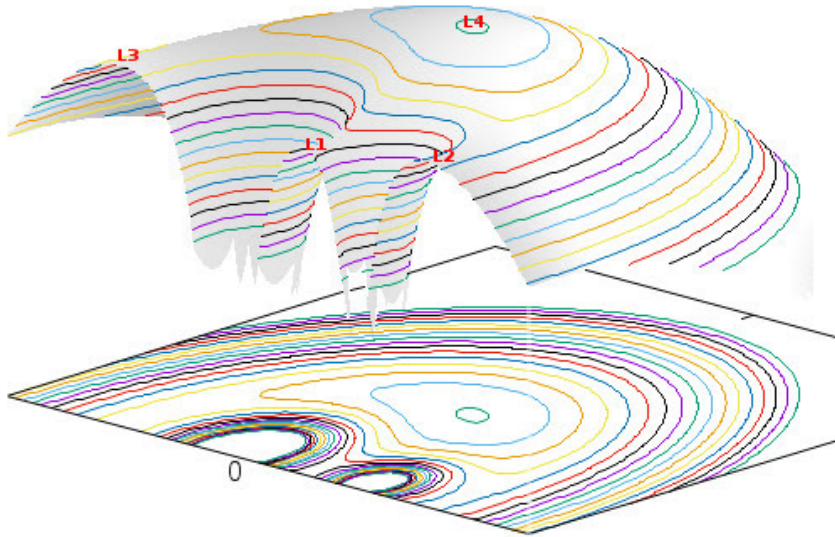


Figura 2.10: The potential function \mathcal{U} close to the Lagrangian points [51]

Capitolo 3

Implementation of the mathematics

In this thesis heliocentric orbits in a two-body system were generated to design interplanetary transfers to be performed by a spacecraft starting from the Lagrangian point L_2 of the Sun-Earth system.

Both starting and arrival orbits around the Sun are elliptical as predicted by Keplerian laws of planetary motion ([5]) and explained through the previously presented conservation of mechanical energy ((2.11)) while the position of each NEA is referred to data taken from NASA Ephemerides so the system built is time-dependent.

In this context low-thrust trajectories have been designed. This brings to elliptical multi-revolution orbits that differentiate themselves from the classical impulsive maneuvers (such as the *Lambert* or *Hohmann's* manoeuvre), typical for the chemical propulsion that is able to generate higher levels of thrust, which take less time to be completed but have a much lower efficiency in terms of propellant consumed in comparison with electrical propulsion and so therefore impose higher mass cost. As a downside, the lower the thrust the greater the number of revolutions around the Sun needed along with more computational difficulties linked with maneuvers performed in the closeness of a planet because of the strength of its gravitational field. An example of this is depicted by [14] regarding escape trajectories from the Earth-Moon system.

3.1 Differential corrector

The aim of this thesis is performing interplanetary trajectory optimization with low-thrust in a two-body model whose central body is the Sun in order to rendez-vous with an asteroid whose orbit is similar to the one of the Earth to get some of its mass and retrieve it back to Earth to use that material to build components for spacecrafts already into Earth orbit, so without any need for them to be launched from Earth with a consequent strong reduction of launching costs. The goal is finding the best solution in order to save propellant during the transfer knowing the departing and the arrival orbits using numerical methods that can be applicable to the widest possible group of orbits rather than to quasi-circular orbits only, as the *Edelbaum's approximation*, that is applied to Gauss's planetary equations, does.

In order to do this a single-shooting procedure has been implemented in order to improve an initial guess regarding the variables of the initial state of the maneuver $\tilde{x}(t_0)$ that, after the integration over the chosen time-span Δt of the equations being performed,

leads to a final state $\tilde{x}(\tilde{x}(t_0), t_f)$ we want to be as similar as possible to the desired final state x_f . As it is described in [34] it is a try-and-error process that does not allow to get which effect any change on the initial guess can generate on the potential convergence. This method has been implemented in the context of a Two-Point Boundary Value Problem (TPBVP) that strictly relies on the comprehension of the relation the problem has with the starting conditions.

The aforementioned improvement of the initial guess is obtained through the *differential correction* process that is applied once the integration of the ODEs of this iteration has been performed. This starts from the initial state guess (composed of constrained values and free values such as the adjoint variables values) and brings to a final state that usually happens to have a discrepancy from the desired. The differential corrector relies on the calculation of this discrepancy

$$\delta\tilde{x}(\tau_f) = \tilde{x}(\tilde{x}(\tau_0), \tau_f) - \tilde{x}^*(\tilde{x}(\tau_0), \tau_f) \quad (3.1)$$

we want to nullify (or to reduce until it goes under a certain threshold when we stop calculations and establish that the convergence has been reached) through the production of a new guess from the correction of the previous one.

$$\tilde{x}^*(\tau_0) = \tilde{x}(\tau_0) + \delta\tilde{x}(t_0) \quad (3.2)$$

If we substitute (3.2) in (3.1) we get the equation that allows to calculate the correction we want to apply on the previous initial guess based upon the discrepancy obtained over the final state

$$\begin{aligned} \delta\tilde{x}(\tau_f) &= \tilde{x}(x(\tau_0), \tau_f) - \tilde{x}^*(\tilde{x}^*(\tau_0), \tau_f) \\ &= \tilde{x}(\tilde{x}(\tau_0) + \delta\tilde{x}(t_0), t_f) - \tilde{x}^*(\tilde{x}^*(\tau_0), \tau_f) \\ &= \frac{\partial\tilde{x}(\tau_f)}{\partial\tilde{x}(\tau_0)}\delta\tilde{x}(t_0) \\ &= \tilde{\Phi}(\tau_f, \tau_0)\delta\tilde{x}(t_0) \end{aligned} \quad (3.3)$$

where $\tilde{\Phi}(\tau_f, \tau_0)$ is the *State Transition Matrix (STM)*, in non-dimensional form, that mediates the relationship between the partial derivatives of the state variables of the final state \tilde{x}_f and the partial derivatives of the initial state \tilde{x}_0 . In the two-body system this matrix assumes the following form

$$\tilde{\Phi}_{ij}(\tau_f, \tau_0) = \frac{\partial\tilde{x}_i(\tau_f)}{\partial\tilde{x}_j(\tau_0)} \quad (3.4)$$

where the vector \tilde{x} has the following structure

$$\tilde{x} = \{x, y, z, \dot{x}, \dot{y}, \dot{z}, m, \lambda_x, \lambda_y, \lambda_z, \lambda_{\dot{x}}, \lambda_{\dot{y}}, \lambda_{\dot{z}}, \lambda_m\}^T \quad (3.5)$$

so this matrix can be considered as the sum of 4 sub-matrixes containing the partial derivatives of variables of position and velocity computed at the final state in relation with both variables of position and velocity of the initial state guess. This means that the STM works as a sensitivity matrix because it evaluates how final state discrepancies with the desired one vary accordingly with the variations imposed on the initial state guess.

This matrix evolves over time along the trajectory of the spacecraft so we can describe how it varies through 36 ODEs that follow the expression below

$$\dot{\tilde{\Phi}}(\tau, \tau_0) = \frac{d}{d\tau} \tilde{\Phi}(\tau, \tau_0) = \frac{d}{d\tau} \left(\frac{\partial \tilde{\chi}}{\partial \tilde{\chi}_0} \right) = \frac{\partial}{\partial \tilde{\chi}_0} \left(\frac{d\tilde{\chi}}{d\tau} \right) = \frac{\dot{\tilde{\chi}}}{\tilde{\chi}_0} = \frac{\partial \dot{\tilde{\chi}}}{\partial \tilde{\chi}} \frac{\partial \tilde{\chi}}{\partial \tilde{\chi}_0} = \tilde{A}(\tau) \tilde{\Phi}(\tau, \tau_0) \quad (3.6)$$

so if we know the initial state STM we can get STM variations at the non-dimensional time τ thanks to the *Jacobian matrix* $\tilde{A}(\tau)$ that establishes the relationship between the second derivatives of the state variables with their underived values. However, if we consider a model defined through a set of first-order ODEs (they have to be integrated only once) we get that the STM will coincide with the Jacobian matrix.

3.2 Single-shooting procedure

The single-shooting procedure is based on the choice of an initial state guess to be used to integrate the ODEs of the system getting a final state result $\tilde{x}(\tau_f)$ that has to be as close as possible to the desired final state x_f . In this thesis it has been applied to a TPBVP in which at every iteration the discrepancy between the obtained $\tilde{x}^k(\tau_f)$ and the desired x_f is calculated and this result is therefore used to correct the initial guess obtaining a new initial guess that will be used to integrate the equations during the following iteration.

If we consider the initial conditions first guess

$$\tilde{x}_0 = \{\tilde{x}_1, \tilde{x}_2, \tilde{x}_3, \dots, \tilde{x}_n\}^T \quad (3.7)$$

and the constraints vector containing the desired final values for the state variables we want the final result to respect

$$\tilde{x}_f = \{\tilde{x}_{1f}, \tilde{x}_{2f}, \tilde{x}_{3f}, \dots, \tilde{x}_{nf}\}^T \quad (3.8)$$

so that the discrepancy between the desired final state x_f and the obtained one $\tilde{x}^k(\tau_f)$ can be collected in the χ vector.

$$\chi(\tilde{x}_f) = \begin{Bmatrix} \chi_1 \\ \chi_2 \\ \dots \\ \chi_m \end{Bmatrix} = \begin{Bmatrix} x - x^* \\ y - y^* \\ z - z^* \\ \dot{x} - \dot{x}^* \\ \dot{y} - \dot{y}^* \\ \dot{z} - \dot{z}^* \end{Bmatrix} \quad (3.9)$$

The whole process is aimed at finding the optimal initial state \tilde{x}_0 that brings us to get $\chi(\tilde{x}_f) = 0$. In order to do that we apply the first-order Taylor expansion of the constraint vector as it follows:

$$\chi(\tilde{x}) = \chi(\tilde{x}_0) + \frac{\partial \chi(\tilde{x}_0)}{\partial \tilde{x}} (\tilde{x} - \tilde{x}_0) \quad (3.10)$$

where the partial derivatives of each constraint component are computed with the finite differences method (that can be computed forward or backward-in-time indifferently)

using the results for χ obtained by integrating ODEs starting from \mathbf{x}_0 and the same quantities obtained by the integration of the same equations starting from a perturbed initial state \mathbf{x}_0^* obtained by perturbing the initial state adding a constant $\boldsymbol{\delta} = \delta\{1, 0, 0, \dots, 0\}^T$ to one of its components whose value has been imposed in 10^{-7}

$$\mathbf{x}_0^* = \mathbf{x}_0 + \boldsymbol{\delta} \quad (3.11)$$

so the obtained perturbed solution is used to calculate its own discrepancy in relation with \mathbf{x}_f in order to calculate a column of the Jacobian matrix (every column is obtained through this same procedure with the only difference that the $\boldsymbol{\delta}$ vector used has its only non-zero term in a different position referred to the only perturbed state variable) according with the following equation

$$\frac{\partial \boldsymbol{\chi}(\tilde{\mathbf{x}}_0)}{\partial \tilde{\mathbf{x}}} = \tilde{\mathbf{J}}(\boldsymbol{\chi}(\tilde{\mathbf{x}}_0), \tilde{\mathbf{x}}) = \begin{bmatrix} \frac{\partial \chi_1}{\partial \tilde{x}_1} & \frac{\partial \chi_1}{\partial \tilde{x}_2} & \cdots & \frac{\partial \chi_1}{\partial \tilde{x}_n} \\ \frac{\partial \chi_2}{\partial \tilde{x}_1} & \frac{\partial \chi_2}{\partial \tilde{x}_2} & \cdots & \frac{\partial \chi_2}{\partial \tilde{x}_n} \\ \vdots & \vdots & \ddots & \vdots \\ \frac{\partial \chi_m}{\partial \tilde{x}_1} & \frac{\partial \chi_m}{\partial \tilde{x}_2} & \cdots & \frac{\partial \chi_m}{\partial \tilde{x}_n} \end{bmatrix} \quad (3.12)$$

where each term is computed with the finite difference method

$$\frac{\partial \boldsymbol{\chi}}{\partial \tilde{\mathbf{x}}_j^*} = \frac{\boldsymbol{\chi} - \boldsymbol{\chi}^*}{\delta} \quad (3.13)$$

So the Jacobian matrix will be $\tilde{\mathbf{J}} \in \mathbb{R}^{m \times n}$ where m is the number of the constrained quantities in the $\boldsymbol{\chi}$ vector and n is the number of the state variables contained in the state vector $\tilde{\mathbf{x}}$.

If we apply this procedure to each iteration we can find the initial state guess to use in the following iteration as a correction of the previous iteration's one following that

$$\boldsymbol{\chi}(\tilde{\mathbf{x}}_{r+1}) = \boldsymbol{\chi}(\tilde{\mathbf{x}}_r) + \frac{\partial \boldsymbol{\chi}(\tilde{\mathbf{x}}_r)}{\partial \tilde{\mathbf{x}}_{r+1}} (\tilde{\mathbf{x}}_{r+1} - \tilde{\mathbf{x}}_r) \quad (3.14)$$

so if we assume that the solution found at the iteration $r+1$ exists we get $\boldsymbol{\chi}_{r+1} = 0$ and so from the inverse expression of (3.14) we get the expression of the new iteration initial state guess

$$\boldsymbol{\chi}(\tilde{\mathbf{x}}_r) + \tilde{\mathbf{J}}(\tilde{\mathbf{x}}_{r+1} - \tilde{\mathbf{x}}_r) = \mathbf{0} \quad (3.15)$$

so isolating $\tilde{\mathbf{x}}_{r+1}$ at the left-hand-side of the 3.15 we get

$$\tilde{\mathbf{x}}_{r+1} = \tilde{\mathbf{x}}_r - \left[\tilde{\mathbf{J}}(\boldsymbol{\chi}_r) \right]^{-1} \boldsymbol{\chi}(\tilde{\mathbf{x}}_r) \quad (3.16)$$

this being always true in this case because the number of variables constrained m is equal to the number of state variables n ($m = n = 9$ if Time of Flight (TOF) and ν are both fixed as it will be discussed in the next subsection). In the calculations for this thesis we used a relaxation factor k_1 equal to 0.1 in order to reduce the corrections induced at every iteration so the (3.16) changes as follows

$$\tilde{\mathbf{x}}_{r+1} = \tilde{\mathbf{x}}_r - k_1 \left[\tilde{\mathbf{J}}(\boldsymbol{\chi}_r) \right]^{-1} \boldsymbol{\chi}(\tilde{\mathbf{x}}_r) \quad (3.17)$$

3.2.1 Single-shooting procedure for free-TOF and free- ν vs fixed-TOF and fixed- ν calculations

Calculations have been made in both the cases considering the arrival time, called TOF, and the true anomaly ν free or fixed.

Every calculation has always been conducted with targeting a single orbit through its Keplerian parameters ($\{a, e, i, \Omega, \omega, \nu\}^T$) as they have been defined in table 2.2, however with keeping ν free we can target an orbit without aiming precisely at any of its points (as we will discuss more in depth in the next chapter the goal of every optimization calculation in this thesis is to maximize the final mass of the spacecraft so as a result the calculation will target the least expensive point of the orbit to reach) while with keeping TOF free we can leave the code free to reach convergence for the trajectory with the duration that maximizes m_f of the spacecraft (if then we set $T = T_{max}$ without any relation with the values of the switching function we will have a *least-time problem* in which we will calculate the quickest trajectory to reach the targeted orbit where weather its arrival point is fixed or not will depend on ν being kept fixed or free).

If ν or TOF or both are free an initial guess will have to be made also about them so the $\tilde{\mathbf{x}}$ at every iteration has to contain also TOF or ν or both. In a similar fashion also J will have different dimensions.

If both are fixed $\boldsymbol{\chi}$ will have 9 elements while $\tilde{\mathbf{x}}$ will have 7 so $J \in \mathbb{R}^{9 \times 7}$. Otherwise, if both are free $J \in \mathbb{R}^{7 \times 9}$ with $\boldsymbol{\chi}$ having 7 elements and $\tilde{\mathbf{x}}$ having 9 instead. If one of the two is free $J \in \mathbb{R}^{8 \times 8}$.

The introduction of the reduced transversality

In order to target an orbit without putting any constraint on ν that for non-circular orbits is linked to all the velocity components it is possible to introduce an alternative transversality condition, an *reduced transversality condition* that has been defined and successfully applied to space trajectories optimization by [38] and follows the expression below

$$\left[\begin{array}{c} \frac{r_f^2}{h_f} \vec{V}_f \\ - \frac{\mu}{r_f^3} \vec{r}_f \frac{r_f^2}{h_f} \end{array} \right] \left\{ \begin{array}{c} \lambda_{r_f} \\ \lambda_{V_f} \end{array} \right\} = 0 \quad (3.18)$$

Conditions from (3.18) have to be added to $\boldsymbol{\chi}$ as an additive constraints. We compute the norm of the vector containing the results of the six equations contained in (3.18) and we reach the optimal solution whenever it gets to zero (or below the minimal threshold established for optimality) so when calculating the norm of $\boldsymbol{\chi}$ we have to consider this term too.

Free-time calculation

If free-time calculation are conducted in order to find the mission-time (TOF) that minimizes the cost of the maneuver in terms of propellant mass a condition has to be added to the $\boldsymbol{\chi}$ vector as a *transversality condition* regarding the value of the Hamiltonian function as it will be discussed in chapter 4, so in this case the following condition evaluated on the final state has to be imposed.

$$\mathcal{H}_f = 0 \tag{3.19}$$

3.3 Non-dimensionalizing values adopted

In order to avoid numerical problems due to the big difference in greatness-order between all the variables involved in the problem (length in an heliocentric maneuver problem is in the order of 10^8 km while for mass is about 10^3 kg and for velocity is about 10^1 km/s) that would occur, for instance, when perturbing the initial state guess by the chosen δ (we want to use the same value for δ for every variable of the problem, but a 10^{-7} perturbation can cause heavily different perturbing effects on the various variables) so it is very beneficial in order to have a more robust code to switch to non-dimensional variables dividing each of them by a characteristic value for that variable so that all the values of the state variables used in the calculations will have a similar order of magnitude (around 10^0).

The non-dimensionalizing length has been chosen equal to the astronomical unit ($1.496 \cdot 10^8$ km), the mean Sun-Earth distance while for the mass it has been chosen the starting mass of the spacecraft (assumed to be 5000 kg). Also gravitational effects have been made non-dimensional using the gravitational parameter of the sun μ_{SUN} (equal to $1.327122 \cdot 10^{11}$ km³/s²). All the other non-dimensionalizing quantities have been indirectly defined, using the defining expressions of the various state variables involved and the aforementioned values chosen for the fundamental variables, as it follows

$$\begin{aligned} V_{adim} &= \sqrt{\frac{\mu_{adim}}{l_{adim}}} \\ t_{adim} &= \frac{l_{adim}}{V_{adim}} \end{aligned} \tag{3.20}$$

An exception has been made for the length along the *z-axis* because of the very low values of inclination of the targeted orbits that bring the recurrent values used for the *z* variables to always be much lower (even by 6 orders of magnitude) than the average value of the other two position coordinates so the value $l_{adim} \sin 2^\circ$ has been used (given that 2° is the maximum inclination for the orbits of the asteroids considered in this thesis).

3.4 Implementation of the code

The aforementioned methods have been implemented in a similar fashion or used by many authors in literature. In particular [17] uses MIN-PACK-1, a package of Fortran, as optimizer while others (such as [49], [50] and others) decided to opt for the MATLAB function *fmincon* together with the genetic optimization method NSGA-II to select the most suitable solutions among a population of trajectories given the problem to solve.

For this work, unlike for all the papers previously cited, a Python code has been implemented with a differential correction optimizer paired with a *C++* precompiled integrator using the library *Numbalsoda* [2] because of its higher computational velocity in comparison with the Python integrator *njit*.

The code has been implemented on a computer using a Intel Core i7 with a frequency of 4.60 GHz and a memory of 8 GB and the consequent performances during computation are reported by table 3.1.

Free TOF	Free ν	Calculation time [s]	Titerations	Avg. iteration rate [iter/s]
Yes	No	86	1690	19.65
No	No	60	1218	20.3

Tabella 3.1: Average iteration rate given one random calculation for each possible architecture (both TOF and ν fixed or only ν fixed)

Capitolo 4

The Optimal Control Problem (OCP)

The goal of Optimal Control Problem (OCP) is the maximization of a merit index to get the desired optimal solution through an optimal control law. In this work calculations are aimed at obtaining the optimal trajectory that minimizes the cost parameter represented by the propellant mass used by the spacecraft. Many sources in literature, such as [27] show how much the Optimal Control Theory has been applied to a great variety of problems such as space trajectory optimization [40], optimization of therapeutic protocols [6], quantum computing [36], dynamic reconstruction problems [46], pulse sequence design optimization in Nuclear Magnetic Resonance (NMR) [44] and other problems.

4.1 Direct vs Indirect Numerical Methods

Optimal Control Problems can be solved implying various possible numerical methods to simplify the more complex problem into by turning it into a group of more simple problems. Those can be divided into two groups of methods that are both widely represented in the literature such as [32], [34], [39] and others

1. Direct Methods
2. Indirect Methods

In particular [34] and [39] point out advantages and disadvantages that the preference for a family of methods rather than for the other leads to.

In fact direct methods, thanks to a discretization of the calculation domain (if the problem is time-dependant this is discretized paying attention to make the mesh as more dense as possible) that sets a finite limit to the number of its dimensions, have a more straightforward implementation, show more robustness and can be applied also to very complex problems. As a downside they can lack of accuracy requiring for the solution to be refined.

On the other hand indirect methods are more accurate and less expensive both computational-wise and time-wise, but they are also more difficult to bring to convergence and to implement in the context of the problem itself given the presence of variables strongly linked

to the particular problem. Another element of complexity in their implementation that is worth noting is their high sensitivity towards initial conditions (their selection has to be carefully made and requires a deep understanding of the problem such method is applied to). Difficulties in finding solutions in different basins of the solution domain can arise especially when used in synergy with single-shooting methods (so switching to multiple-shooting methods can be beneficial to increase robustness of such methods).

4.2 The Optimal Control Theory

It is applied to a system of differential equations that can be described by the following form

$$\dot{\mathbf{x}}(t) = \mathbf{f}(\mathbf{x}(t), \mathbf{u}(t), t) \quad (4.1)$$

where the vector \mathbf{x} , called the *state vector* of the problem, contains the n real-valued state variables of the problem and the vector \mathbf{u} contains the m control variables, so being *m-dimensional*, and all of those can be defined, accordingly with the problem, as time-dependent.

Optimal Control Problems can have constraints applied to some of its state variables to either (or both) ends of the time interval the calculation is made on. Those constraints are called Boundary Conditions (BCs) and can be described by equations collected in the vector χ defined as follows

$$\chi(\mathbf{x}_0, \mathbf{x}_f, t_0, t_f) = \mathbf{0} \quad (4.2)$$

where $\chi : [\mathbb{R}^n, \mathbb{R}^n, \mathbb{R}, \mathbb{R}] \rightarrow \mathbb{R}$.

Also the vector \mathbf{u} can be constrained through an admissibility range defined by maximum or minimum values the control variable can assume. The criterion is defined with the expression $\mathbf{u} \in U$

$$J = \phi(\mathbf{x}_0, \mathbf{x}_f, t_0, t_f) + \int_{t_0}^{t_f} [\Phi(\mathbf{x}(t), \mathbf{u}(t), t)] dt \quad (4.3)$$

The goal of OCP is finding stationary points (maximum or minimum) for a function J that is the cost functional (a real-valued function defined through an integral expression) of the problem. It is used to associate a cost with each possible state and each admissible control and for this reason the goal is to maximize or minimize it finding the optimality of the problem (with the optimal state vector \mathbf{x}^* and the optimal control vector \mathbf{u}^* associated with it).

The function ϕ represents the contribution to the whole cost coming from the state variables for the values they assume at the extremes of the considered time domain. If we nullify it ($\phi = \mathbf{0}$) we get the Lagrange's form of the problem. The function Φ represents how the cost function varies over time. If we nullify it ($\Phi = \mathbf{0}$) we get the Mayer's form of the problem. For the sake of brevity we can adopt the following expressions.

$$\phi = \phi(\mathbf{x}_0, \mathbf{x}_f, t_0, t_f) \quad (4.4)$$

$$\chi = \chi(\mathbf{x}_0, \mathbf{x}_f, t_0, t_f) \quad (4.5)$$

If we consider an OCP with BCs we get the *augmented form* of the cost functional (J^*) that contains the term $\boldsymbol{\mu}^T \boldsymbol{\chi}$ where $\boldsymbol{\mu}$ contains the Lagrange multipliers related to each BC in the context of the first-order necessary condition for optimality in n-dimensional constrained problems that states that it can be proven, if the hypothesis reported by [27] are fulfilled, that in order to get the optimality it is necessary to have

$$\delta J^* = 0 \quad (4.6)$$

that translates into an expression that [27] shows to be the definition of the linear dependence between the gradient of the function to optimize and a linear combination of the gradients of the constraint functions whose coefficient are the Lagrange multipliers collected into $\boldsymbol{\mu}$

$$\nabla J^* = \sum_{j=1}^n \boldsymbol{\mu}_j^T \nabla \boldsymbol{\chi}_j \quad (4.7)$$

so integrating the equation we find the definition of the augmented cost as the sum of the ϕ and the $\boldsymbol{\mu}^T \boldsymbol{\chi}$ terms. Moreover, the integral term contains the influence played on the cost by the closeness of the results of the equations of the problem to optimality (it is achieved if (4.1) is satisfied) and it is obtained in similar fashion as already done with the $\boldsymbol{\mu}^T \boldsymbol{\chi}$ because of the application of the first order necessary condition for optimality to the integral term for the OCP with constraints.

So the augmented cost is

$$J^* = \phi + \boldsymbol{\mu}^T \boldsymbol{\chi} + \int_{t_0}^{t_f} [\boldsymbol{\Phi} + \boldsymbol{\lambda}^T (\boldsymbol{f} - \dot{\boldsymbol{x}})] dt \quad (4.8)$$

and so, because of (4.6), we get m more constraint equations that can be added to the aforementioned n BC equations.

If we apply the integration by parts on the integral term it follows

$$\int_{t_0}^{t_f} -[\boldsymbol{\lambda}^T \dot{\boldsymbol{x}}] dt = -(\boldsymbol{\lambda}_f^T \boldsymbol{x}_f) + (\boldsymbol{\lambda}_0^T \boldsymbol{x}_0) + \int_{t_0}^{t_f} [\dot{\boldsymbol{\lambda}}^T \boldsymbol{x}] dt \quad (4.9)$$

so the augmented cost functional expression gets the following form

$$J^* = \phi + \boldsymbol{\mu}^T \boldsymbol{\chi} + (\boldsymbol{\lambda}_0^T \boldsymbol{x}_0 - \boldsymbol{\lambda}_f^T \boldsymbol{x}_f) + \int_{t_0}^{t_f} [\boldsymbol{\Phi} + \boldsymbol{\lambda}^T \boldsymbol{f} - \dot{\boldsymbol{\lambda}}^T \boldsymbol{x}] dt \quad (4.10)$$

where we can underline the presence of a very important term, the *Hamiltonian*, defined as follows.

$$\mathcal{H} = \boldsymbol{\Phi} + \boldsymbol{\lambda}^T \boldsymbol{f} \quad (4.11)$$

For the aforementioned first-order necessary condition for optimality we have to find a stationary point for the augmented cost function so we calculate its derivatives with respect to the variables it depends on, those being t_0 , t_f , \boldsymbol{x}_0 , \boldsymbol{x}_f so the obtained expression is the following

$$\begin{aligned}
 \delta J^* = & \left(\frac{\partial \phi}{\partial t_0} + \boldsymbol{\mu}^T \frac{\partial \boldsymbol{\chi}}{\partial t_0} - \mathcal{H}_0 \right) \delta t_0 + \left(\frac{\partial \phi}{\partial t_f} + \boldsymbol{\mu}^T \frac{\partial \boldsymbol{\chi}}{\partial t_f} - \mathcal{H}_f \right) \delta t_f + \\
 & + \left(\frac{\partial \phi}{\partial \mathbf{x}_0} + \boldsymbol{\mu}^T \frac{\partial \boldsymbol{\chi}}{\partial \mathbf{x}_0} - \boldsymbol{\lambda}_0^T \right) \delta \mathbf{x}_0 + \left(\frac{\partial \phi}{\partial \mathbf{x}_f} + \boldsymbol{\mu}^T \frac{\partial \boldsymbol{\chi}}{\partial \mathbf{x}_f} - \boldsymbol{\lambda}_f^T \right) \delta \mathbf{x}_f + \\
 & + \int_{t_0}^{t_f} \left[\left(\frac{\partial \mathcal{H}}{\partial \mathbf{x}} + \dot{\boldsymbol{\lambda}}^T \right) \delta \mathbf{x} + \frac{\partial \mathcal{H}}{\partial \mathbf{u}} \delta \mathbf{u} \right] dt
 \end{aligned} \tag{4.12}$$

so applying the statement (4.6) as a result it is possible to get two sets of equations.

The first is obtained by nullifying the expressions multiplied by the variations of the t_0 , t_f , \mathbf{x}_0 and \mathbf{x}_f variables among which we have two equations, obtained by nullifying the t_0 and t_f , called *transversality conditions* which are useful to impose the necessary perpendicularity between the optimal adjoint variables vector in the final state, $\boldsymbol{\lambda}^*(t_f)$, and the tangent space to the surface determined by the constraint equations and so determining the optimal t_0 and t_f (if they are not constrained)

$$\frac{\partial \phi}{\partial t_0} + \boldsymbol{\mu}^T \frac{\partial \boldsymbol{\chi}}{\partial t_0} - \mathcal{H}_0 = 0 \tag{4.13}$$

$$\frac{\partial \phi}{\partial t_f} + \boldsymbol{\mu}^T \frac{\partial \boldsymbol{\chi}}{\partial t_f} - \mathcal{H}_f = 0 \tag{4.14}$$

and a pair of sets composed of n equations each, obtained by nullifying the \mathbf{x}_0 and \mathbf{x}_f terms of δJ^* , called *optimality conditions* that allow to determine the optimal initial and final state ($\mathbf{x}^*(t_0)$ and $\mathbf{x}^*(t_f)$) with their optimal adjoint variables vectors ($\boldsymbol{\lambda}^*(t_0)$ and $\boldsymbol{\lambda}^*(t_f)$) if they are not constrained.

$$\frac{\partial \phi}{\partial \mathbf{x}_0} + \boldsymbol{\mu}^T \frac{\partial \boldsymbol{\chi}}{\partial \mathbf{x}_0} - \boldsymbol{\lambda}_0^T = \mathbf{0} \tag{4.15}$$

$$\frac{\partial \phi}{\partial \mathbf{x}_f} + \boldsymbol{\mu}^T \frac{\partial \boldsymbol{\chi}}{\partial \mathbf{x}_f} - \boldsymbol{\lambda}_f^T = \mathbf{0} \tag{4.16}$$

so those $2n+2$ equations represent how time and state variables (along with the adjoint state variables and the Hamiltonian that "plays the role" of the adjoint variable for the time variable). It is worth noticing that if t_0 or t_f are neither constrained (so there are no equations involving them in the $\boldsymbol{\chi}$ vector) nor present in ϕ (so both $\frac{\partial \phi}{\partial t_0}$ and $\frac{\partial \boldsymbol{\chi}}{\partial t_0}$ or $\frac{\partial \phi}{\partial t_f}$ and $\frac{\partial \boldsymbol{\chi}}{\partial t_f}$ are equal to 0) as a consequence $\mathcal{H}_0 = 0$ or $\mathcal{H}_f = 0$ meaning that t_0 or t_f are subject to optimization. On the other hand if t_0 or t_f are constrained \mathcal{H}_0 and \mathcal{H}_f are free. In the same fashion it is possible to point out this sort of relationship existing also between each state variable (x_{0i} and x_{fi}) and its adjoint variable (λ_{0i} and λ_{fi}). If the state is free and subject to optimization its costate is 0, if the state is fixed its costate is subject to optimization.

The second set of equations obtained from the condition (4.6) comes from nullifying the integral term of δJ^*

$$\int_{t_0}^{t_f} \left[\left(\frac{\partial \mathcal{H}}{\partial \mathbf{x}} + \dot{\boldsymbol{\lambda}}^T \right) \delta \mathbf{x} + \frac{\partial \mathcal{H}}{\partial \mathbf{u}} \delta \mathbf{u} \right] dt = 0 \tag{4.17}$$

so by nullifying both the terms contained in it (the $\delta \mathbf{x}$ and $\delta \mathbf{u}$ term) we get two more equations, the *Hamilton's canonical equations* (the first is called *Euler-Lagrange equation*) that have to be added to the already defined $2n+2$ equations

$$\frac{d\boldsymbol{\lambda}}{dt} = -\left(\frac{\partial \mathcal{H}}{\partial \mathbf{x}}\right)^T \quad (4.18)$$

$$\left(\frac{\partial \mathcal{H}}{\partial \mathbf{u}}\right)^T = 0 \quad (4.19)$$

From the equation (4.19) it is possible to point out that in order to extremize the augmented cost function it is also necessary to extremize the Hamiltonian point-by-point along the trajectory with respect to the command vector \mathbf{u} . This is what is stated by the *Pontryagin's Maximum Principle (PMP)*. The result of these equations depends on the relationship between the Hamiltonian and the vector of the control variables. In fact, if this relationship is linear it follows that the derivative is constant, otherwise it will depend on u_i itself

$$\frac{\partial \mathcal{H}}{\partial u_i} = \begin{cases} k_{ui} & \text{if } H \text{ is affine wrt } u_i \\ f(u_i) & \text{otherwise} \end{cases} \quad (4.20)$$

so in order to maximize the Hamiltonian we can impose $\mathbf{u}_i = \mathbf{U}_{max}$ if $k_{ui}>0$ while $\mathbf{u}_i = \mathbf{U}_{min}$ if $k_{ui}<0$. This control is called *bang-bang control*. The only exception is referred to the case of $k_{ui}=0$ that is due to the fact that the Hamiltonian has no dependence on the command variable. The $k_{ui}<0$ term is called *switching function* so we associate to it being positive the maximum admissible value for the control variable while we associate to it being negative the minimum admissible value for the control variable.

As a consequence the OCP is mathematically defined by two transversality equations (4.13 and 4.14), $2n$ optimality equations (4.15 and 4.16) and m control equations (4.19) while the n Euler-Lagrange equations (4.18) have to be added to the defining equations of the problem itself (4.1) to determine the optimal values of the adjoint variables through the computation of their time derivatives.

4.3 Multi-Point Optimal Control Theory

A way to increase robustness of the code and to avoid any issue related with discontinuities of one or more variables along the trajectory (also potentially due to local constraints throughout the transfer) is to divide the time domain of integration of the equations into arcs cleverly chosen to eventually set their borders exactly where such discontinuities or constraints are supposed to be. This tool is useful to have continuous variables along each arc and the goal of the OCP (that becomes so a *Multi-Point Optimal Control Problem, MPOCP*)

As a consequence of this choice the vector of BCs equations have to be determined on each border between a pair of consecutive arcs as it follows through their values of time and state variables.

$$\boldsymbol{\chi}\left(\mathbf{x}_{(j-1)_+}, \mathbf{x}_{j_-}, t_{(j-1)_+}, t_{j_-}\right) = \mathbf{0} \quad (4.21)$$

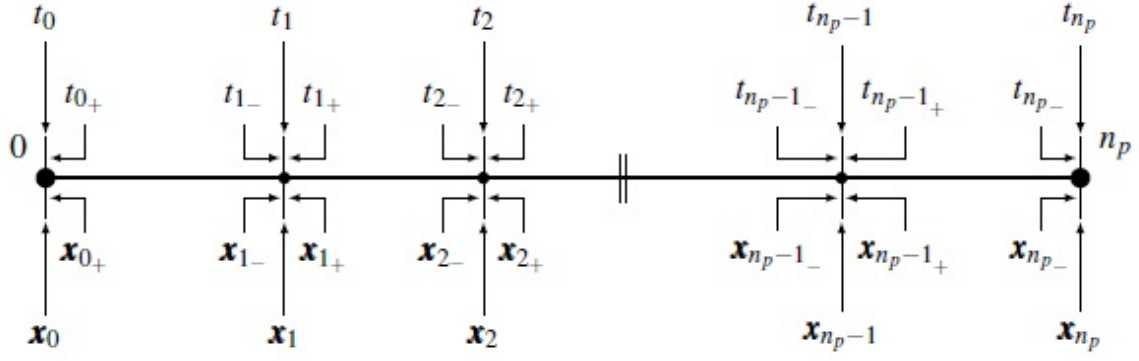


Figure 4.1: Schematic representation of the MPBVP arc discretization of its domain and its trajectory [34]

The same thing happens with the definition of the cost functional and its augmented form

$$J = \phi \left(\mathbf{x}_{(j-1)_+}, \mathbf{x}_{j_-}, t_{(j-1)_+}, t_{j_-} \right) + \sum_{j=1}^{n_p} \int_{t_{(j-1)_+}}^{t_{j_-}} [\Phi(\mathbf{x}(t), \mathbf{u}(t), t)] dt \quad (4.22)$$

$$J^* = \phi + \boldsymbol{\mu}^T \boldsymbol{\chi} + \sum_{j=1}^{n_p} \int_{t_{(j-1)_+}}^{t_{j_-}} [\Phi + \boldsymbol{\lambda}^T (\mathbf{f} - \dot{\mathbf{x}})] dt \quad (4.23)$$

where both the non integral and the integral terms have to be calculated on each arc, each of them having their own ϕ and Φ functions defined along.

The original OCP has now been turned into a series of smaller OCPs we have to solve each along every arc in order to obtain the optimal solution through the sum of many optimal arcs of trajectory. It is a sort of generalization of the problem where the global optimal solution is obtained through a sum of optimal segments of solution. For this reason the goal is to extremize J^* through the application of the *first-order necessary condition for optimality* (equation 4.6)

$$\begin{aligned} \delta J^* = & \left(\frac{\partial \phi}{\partial t_{(j-1)_+}} + \boldsymbol{\mu}^T \frac{\partial \boldsymbol{\chi}}{\partial t_{(j-1)_+}} - \mathcal{H}_{(j-1)_+} \right) \delta t_{(j-1)_+} + \\ & + \left(\frac{\partial \phi}{\partial t_{j_-}} + \boldsymbol{\mu}^T \frac{\partial \boldsymbol{\chi}}{\partial t_{j_-}} - \mathcal{H}_{j_-} \right) \delta t_{j_-} + \\ & + \left(\frac{\partial \phi}{\partial \mathbf{x}_{(j-1)_+}} + \boldsymbol{\mu}^T \frac{\partial \boldsymbol{\chi}}{\partial \mathbf{x}_{(j-1)_+}} - \boldsymbol{\lambda}_{(j-1)_+}^T \right) \delta \mathbf{x}_{(j-1)_+} + \\ & + \left(\frac{\partial \phi}{\partial \mathbf{x}_{j_-}} + \boldsymbol{\mu}^T \frac{\partial \boldsymbol{\chi}}{\partial \mathbf{x}_{j_-}} - \boldsymbol{\lambda}_{j_-}^T \right) \delta \mathbf{x}_{j_-} + \int_{t_{(j-1)_+}}^{t_{j_-}} \left[\left(\frac{\partial \mathcal{H}}{\partial \mathbf{x}} + \dot{\boldsymbol{\lambda}}^T \right) \delta \mathbf{x}_0 + \frac{\partial \mathcal{H}}{\partial \mathbf{u}} \delta \mathbf{u} \right] dt \end{aligned} \quad (4.24)$$

If we nullify δJ^* we get the two *transversality equations*, the $2n$ *optimality equations* that have to be imposed on each arc to find the optimal solution on each of them and the two sets of *Hamilton's canonical equations*, the *Euler-Lagrange equations* and the equations stating the relationship between the Hamiltonian and the control variables

$$\frac{\partial \phi}{\partial t_{(j-1)_+}} + \boldsymbol{\mu}^T \frac{\partial \chi}{\partial t_{(j-1)_+}} - \mathcal{H}_{(j-1)_+} = 0, \quad j = 0, \dots, n_p - 1 \quad (4.25)$$

$$\frac{\partial \phi}{\partial t_{j_-}} + \boldsymbol{\mu}^T \frac{\partial \chi}{\partial t_{j_-}} - \mathcal{H}_{j_-} = 0, \quad j = 1, \dots, n_p \quad (4.26)$$

$$\frac{\partial \phi}{\partial \mathbf{x}_{(j-1)_+}} + \boldsymbol{\mu}^T \frac{\partial \chi}{\partial \mathbf{x}_{(j-1)_+}} - \boldsymbol{\lambda}_{(j-1)_+}^T = 0, \quad j = 0, \dots, n_p - 1 \quad (4.27)$$

$$\frac{\partial \phi}{\partial \mathbf{x}_{j_-}} + \boldsymbol{\mu}^T \frac{\partial \chi}{\partial \mathbf{x}_{j_-}} - \boldsymbol{\lambda}_{j_-}^T = 0, \quad j = 1, \dots, n_p \quad (4.28)$$

$$\frac{\partial \mathcal{H}}{\partial \mathbf{x}} + \dot{\boldsymbol{\lambda}}^T = 0 \quad (4.29)$$

$$\frac{\partial \mathcal{H}}{\partial \mathbf{u}} = 0 \quad (4.30)$$

4.4 The implemented Boundary Value Problem

In order to solve the aforementioned OCP we implement a Boundary Value Problem (BVP) using an indirect single-shooting method depending on the initial values (typical feature for indirect methods) we have to generate a guess about at every iteration, starting from an initial guess whose structure should be coherent with the following expression.

$$\mathbf{y}_0^* = \left\{ (\mathbf{x}_0^*)^T (\boldsymbol{\lambda}_0)^T \right\}^T \quad (4.31)$$

The result can heavily depend on the initial guess because it is the basis to generate all the subsequent guesses so therefore it is necessary to guide the convergence of the problem to the solution to avoid it to converge to a different one. The correctness of the obtained solution is checked by calculating the difference between the resulting final state $\mathbf{y}_r(t_f)$ and the desired one \mathbf{y}_f^* . If it is below a certain established threshold we can conclude that the initial guess used to start the integration of the differential equations of the problem for that iteration, $\tilde{\mathbf{y}}_0^*$, is the optimal initial state for the manoeuvre.

The considered problem has a strong time-dependance so it is possible to normalize the time-span of integration given the fact that we do not know the time-length of each arc. As a consequence we can have that $\Delta t_j = 1$ for each $j \in (1, n_p)$. This implies that t (that is therefore normalized into t_ϵ) will span from $j - 1$ to j , independently from its effective time duration that is not known at the beginning of the calculation, accordingly with the following expression.

$$t_\epsilon = (j - 1) + \frac{t - t_{j-1}}{t_j - t_{j-1}} = (j - 1) + \frac{t - t_{j-1}}{\Delta t_j} \quad \Delta t_j = t_j - t_{j-1} \quad (4.32)$$

Changing the time variable transforms the equations of the problem bringing them to the following time-adimensional form that can be used to generalize the notation in this chapter

$$\dot{\check{y}} = \mathbf{f}(\check{y}(t_\epsilon), t_\epsilon) \quad (4.33)$$

$$\dot{\check{z}} = \mathbf{f}(\check{z}(t_\epsilon), t_\epsilon) \quad (4.34)$$

where $\dot{\check{z}}$ is composed of the time derivatives of the state variables \check{y} of the constants vector \check{c}

$$\dot{\check{z}} = \begin{bmatrix} \dot{\check{y}} \\ \dot{\check{c}} \end{bmatrix} = \begin{bmatrix} \Delta t_j \frac{dy(t)}{dt} \\ 0 \end{bmatrix} \quad (4.35)$$

At every iteration we check the difference between the obtained final state and the desired one (the results are collected in the boundary conditions vector $\check{\chi}(\check{s})$) to verify if the following relation holds

$$\chi(\check{s}) = 0 \quad (4.36)$$

where \check{s} according with the general notation is the matrix containing at each column the vector of the conditions at the boundaries at each arc if the discretion of the time interval of the integration is implemented.

$$\check{s} = \left\{ \check{y}_0^T \quad \check{y}_1^T \quad \dots \quad \check{y}_{n_p-1}^T \quad \check{y}_{n_p}^T \quad \check{c} \right\} \quad (4.37)$$

At every iteration after the integration of the equations and the evaluation of the $\check{\chi}(\check{s})$ vector containing the boundary conditions we perturb the initial conditions by a delta that we assumed as 10^{-7} in order to integrate the equations again and evaluate the $\check{\chi}(\check{s})$ of the perturbed problem and to use them to calculate the *Jacobian matrix* that guides the calculation of the new initial conditions guess for the next iteration according with the following equation (and its indirect form where the guess for the next iteration is explicitly calculated)

$$\chi(\check{q}_{r+1}) = \chi(\check{q}_r) + \frac{\partial \chi(\check{q}_r)}{\partial \check{q}_{r+1}} (\check{q}_{r+1} - \check{q}_r) \quad (4.38)$$

$$\check{q}_{r+1} = \check{q}_r - [\check{J}(\check{\chi}_r)]^{-1} \chi(\check{q}_r) \quad (4.39)$$

while the convergence is obtained when the following relationship holds true.

$$0 = \chi(\check{q}_r) + [\check{J}(\check{\chi}_r)] (\check{q}_{r+1} - \check{q}_r) \quad (4.40)$$

The Jacobian matrix is the result of the variations in the results of the border conditions vector caused by a variation in the initial conditions

$$\check{J} = \begin{bmatrix} \frac{\partial \chi_1}{\partial x_{01}} & \frac{\partial \chi_1}{\partial x_{02}} & \frac{\partial \chi_1}{\partial x_{03}} & \frac{\partial \chi_1}{\partial x_{04}} & \frac{\partial \chi_1}{\partial x_{05}} & \frac{\partial \chi_1}{\partial x_{06}} & \frac{\partial \chi_1}{\partial x_{07}} \\ \frac{\partial \chi_2}{\partial x_{01}} & \frac{\partial \chi_2}{\partial x_{02}} & \frac{\partial \chi_2}{\partial x_{03}} & \frac{\partial \chi_2}{\partial x_{04}} & \frac{\partial \chi_2}{\partial x_{05}} & \frac{\partial \chi_2}{\partial x_{06}} & \frac{\partial \chi_2}{\partial x_{07}} \\ \frac{\partial \chi_3}{\partial x_{01}} & \frac{\partial \chi_3}{\partial x_{02}} & \frac{\partial \chi_3}{\partial x_{03}} & \frac{\partial \chi_3}{\partial x_{04}} & \frac{\partial \chi_3}{\partial x_{05}} & \frac{\partial \chi_3}{\partial x_{06}} & \frac{\partial \chi_3}{\partial x_{07}} \\ \frac{\partial \chi_4}{\partial x_{01}} & \frac{\partial \chi_4}{\partial x_{02}} & \frac{\partial \chi_4}{\partial x_{03}} & \frac{\partial \chi_4}{\partial x_{04}} & \frac{\partial \chi_4}{\partial x_{05}} & \frac{\partial \chi_4}{\partial x_{06}} & \frac{\partial \chi_4}{\partial x_{07}} \\ \frac{\partial \chi_5}{\partial x_{01}} & \frac{\partial \chi_5}{\partial x_{02}} & \frac{\partial \chi_5}{\partial x_{03}} & \frac{\partial \chi_5}{\partial x_{04}} & \frac{\partial \chi_5}{\partial x_{05}} & \frac{\partial \chi_5}{\partial x_{06}} & \frac{\partial \chi_5}{\partial x_{07}} \\ \frac{\partial \chi_6}{\partial x_{01}} & \frac{\partial \chi_6}{\partial x_{02}} & \frac{\partial \chi_6}{\partial x_{03}} & \frac{\partial \chi_6}{\partial x_{04}} & \frac{\partial \chi_6}{\partial x_{05}} & \frac{\partial \chi_6}{\partial x_{06}} & \frac{\partial \chi_6}{\partial x_{07}} \\ \frac{\partial \chi_7}{\partial x_{01}} & \frac{\partial \chi_7}{\partial x_{02}} & \frac{\partial \chi_7}{\partial x_{03}} & \frac{\partial \chi_7}{\partial x_{04}} & \frac{\partial \chi_7}{\partial x_{05}} & \frac{\partial \chi_7}{\partial x_{06}} & \frac{\partial \chi_7}{\partial x_{07}} \end{bmatrix} \quad (4.41)$$

where every single term of the matrix is defined as follows

$$\check{J}_{ij} = \frac{\partial \chi(\check{q}_r)}{\partial \check{q}_{r+1}} = \frac{\check{\chi}_i - \chi_i}{\Delta x_{0j}} \quad (4.42)$$

The inversion of the Jacobian matrix is crucial in order to calculate the correction of the initial condition guess used and so to obtain the guess to use for the following iteration as in eq.4.39.

Also the Jacobian matrix is subjected to an evolution that can be tracked by calculating a matrix multiplication

$$\check{J}(\check{\chi}_r) = \frac{\partial \chi(\check{q}_r)}{\partial \check{q}_{r+1}} \quad (4.43)$$

Such formulation allows also the introduction of discontinuities in the state variables at the boundaries of each arc that can be eventually used if we want to use the Multi-Point Boundary Value Problem (MPBVP) as described in [34].

The use of linear mapping through a STM induces errors during the iterative process of differential correction inducing divergences so in order to avoid that two correction factors have been introduced:

- k_1 is introduced as a relaxation parameter during the correction process of the new initial conditions guess as shown in the eq.4.39:

$$\check{q}_{r+1} = \check{q}_r - k_1 [\check{J}(\check{\chi}_r)]^{-1} \chi(\check{q}_r) \quad (4.44)$$

where lower values for k_1 (close to its minimum assumed to be 0.1) are useful for the first raw attempts only to increase it when we are getting closer to convergence;

- k_2 is used on a control over the relationship between the error calculated at two successive iterations to check if the successive iteration has a greater error than the previous one (if it is the case k_2 can be halved up to five times)

$$E_{max_{r+1}} < k_2 E_{max_r} \quad (4.45)$$

4.5 OCP for spacecraft trajectory optimization

In this work the OCT has been applied to the integration of a set of ODEs describing the dynamics of a spacecraft in a two-body system without any considered perturbation.

$$\frac{d\mathbf{r}}{dt} = \mathbf{V} \quad (4.46)$$

$$\frac{d\mathbf{V}}{dt} = \mathbf{g} + \frac{\mathbf{T}}{m} \quad (4.47)$$

$$\frac{dm}{dt} = -\frac{\mathbf{T}}{c} \quad (4.48)$$

The goal of their integration combined with the application of the optimal control theory is finding the optimal control law $\mathbf{u}^*(t)$ that maximizes the final mass of the spacecraft at the end of the maneuver.

The variables of the problem are the state vector that as an input is described through keplerian orbital parameters

$$\mathbf{x}_{kepl} = \{a, e, i, \Omega, \omega, \nu\}^T \quad (4.49)$$

and can be converted into Cartesian parameters.

$$\mathbf{x}_{cart} = \{x, y, z, V_x, V_y, V_z\}^T \quad (4.50)$$

If we add also their adjoint variables we get the *state vector* containing $2n$ terms

$$\mathbf{x}_{cart} = \{x, y, z, V_x, V_y, V_z, \lambda_x, \lambda_y, \lambda_z, \lambda_{V_x}, \lambda_{V_y}, \lambda_{V_z}, m, \lambda_m\}^T \quad (4.51)$$

while the merit index (being $\Phi=0$ as for the Mayer formulation) is the final mass of the spacecraft.

The Hamiltonian function \mathcal{H} , as following eq.4.11, assumes the following expression

$$\begin{aligned} \mathcal{H} = \boldsymbol{\lambda}^* \mathbf{f} &= \sum_{i=1}^{2n} \lambda_i f_i = \lambda_x V_x + \lambda_y V_y + \lambda_z V_z + \\ &+ \lambda_{V_x} \left[-\frac{\mu}{r^{3/2}} x + \frac{T}{m} \frac{\lambda_{V_x}}{\lambda_V} \right] + \lambda_{V_y} \left[-\frac{\mu}{r^{3/2}} y + \frac{T}{m} \frac{\lambda_{V_y}}{\lambda_V} \right] + \\ &+ \lambda_{V_z} \left[-\frac{\mu}{r^{3/2}} z + \frac{T}{m} \frac{\lambda_{V_z}}{\lambda_V} \right] - \lambda_m \frac{T}{c} \end{aligned} \quad (4.52)$$

that, after grouping all the terms multiplying the thrust-to-mass ratio in the so called *switching function* that defines weather the thruster is pushing and when not, assumes the following more compact form

$$\mathcal{H} = \lambda_x V_x + \lambda_y V_y + \lambda_z V_z - \frac{\mu}{r^{3/2}} (x \lambda_{V_x} + y \lambda_{V_y} + z \lambda_{V_z}) + T \mathcal{S}_F \quad (4.53)$$

where the *switching function* has the following expression

$$\mathcal{S}_F = \frac{\boldsymbol{\lambda}_V}{m} - \frac{\lambda_m}{c} \quad (4.54)$$

so it is possible to notice how the components of the *primer vector* $\boldsymbol{\lambda}_V$, collecting the adjoint variables of the three components of velocity

$$\boldsymbol{\lambda}_V = \{\lambda_{V_x}, \lambda_{V_y}, \lambda_{V_z}\}^T \quad (4.55)$$

so that $\lambda_V = \|\boldsymbol{\lambda}_V\|$, influences \mathcal{S}_F so that if the costates on the velocity components are high enough to make it positive they will lead the thrusters to push more in the simulation. As we can see from the ODEs of the costates in appendix A they are influenced by the costates on the position vector components (λ_x , λ_y and λ_z) so these are responsible for the \mathcal{S}_F to be positive. If $\mathcal{S}_F > 0$ holds true for the whole Δt of integration we will have that the thruster will push along the whole manoeuvre so that the code will have many difficulties to converge to any solution because given the time and state constraints assumed it is impossible for the spacecraft performing the manoeuvre to fulfill it even by always pushing. The same goes for λ_x , λ_y and λ_z too low so that $\boldsymbol{\lambda}_V$ makes $\mathcal{S}_F < 0$ because the spacecraft would always be on costing mode.

The *control vector* $\mathbf{u}(t)$ is defined by the magnitude and the direction of the *thrust vector* \mathbf{T} that are determined by the maximum value of the thrust provided by the thrusters (being the control a *bang-bang* because the hamiltonian has a linear relationship with the Thrust so only T_{max} can maximize the hamiltonian) and the thrust angles α_T , that describes the direction of the thrust into the orbital plane, and β_T that defines its component along the perpendicular direction to the plane. In order to evaluate the α_T and β_T values that can maximize the hamiltonian we have to nullify the derivatives of the hamiltonian in relation with both of the thrust angles respectively given the expression of the thrust vector \mathbf{T}

$$T = \begin{Bmatrix} T_u \\ T_v \\ T_w \end{Bmatrix} = T \begin{Bmatrix} \sin \alpha_T \cos \beta_T \\ \cos \alpha_T \cos \beta_T \\ \sin \beta_T \end{Bmatrix} \quad (4.56)$$

So if we want to maximize the Hamiltonian through the proper values for α_T and β_T we get

$$\frac{\partial \mathcal{H}}{\partial \alpha_T} = 0 = \cos \alpha_T \lambda_{v_x} - \sin \alpha_T \lambda_{v_y} \quad (4.57)$$

$$\frac{\partial \mathcal{H}}{\partial \beta_T} = 0 = -\sin \beta_T (\sin \alpha_T \lambda_{v_x} + \cos \alpha_T \lambda_{v_y}) + \cos \beta_T \lambda_{v_z} \quad (4.58)$$

and after a proper mathematical manipulation of eqs. 4.57 and 4.58 that also involves prostapheresis equations we get both the expressions for the optimal values of α_T and β_T

$$\alpha_T = \arctan \frac{\lambda_{v_x}}{\lambda_{v_y}} \quad (4.59)$$

$$\beta_T = \arctan \frac{\lambda_{v_z}}{\cos \alpha_T \lambda_{v_y} (1 + \tan^2 \alpha_T)} = \arcsin \frac{\lambda_{v_z}}{\lambda_V} \quad (4.60)$$

and the equations that give the components of the primer vector in relation with thrust angles

$$\begin{aligned} \frac{\lambda_{v_x}}{\lambda_V} &= \sin \alpha_T \cos \beta_T \\ \frac{\lambda_{v_y}}{\lambda_V} &= \cos \alpha_T \cos \beta_T \\ \frac{\lambda_{v_z}}{\lambda_V} &= \sin \beta_T \end{aligned} \quad (4.61)$$

4.5.1 The reduced transversality conditions

Whenever we want to solve a problem of Space Trajectory Optimization targeting an orbit without specifying one or more of its Keplerian parameters (because we want to find their optimal value in order to minimize the propellant mass spent) we have to consider a different type of transversality conditions, the *reduced transversality conditions* that are built in order to work properly in an optimization problem without any use of the Lagrange multipliers which heavily decrease the robustness of the code in finding convergences.

This relies on the fact that it is systematically possible to set constraints on Keplerian orbital parameters rather than on certain components of position and velocity (this is possible anyway because targeting some Keplerian parameters of an orbit automatically fixes values for components of position and velocity). In particular [38] shows conditions linked with each Keplerian parameter being set free that can be added to the already defined constraints vector $\boldsymbol{\chi}$.

These being transversality conditions are applied to the final state \boldsymbol{x}_f and they follow the expression

$$\boldsymbol{y}_i^T(\boldsymbol{x}_f)\boldsymbol{\lambda}_f = 0 \quad i = 1, \dots, 6 - k \quad (4.62)$$

where k is the number of constrained variables and y_i is a set of linearly independent solutions of the preceding system (each \boldsymbol{y}_i is a function of x_f , $\boldsymbol{y}_i(\boldsymbol{x}_f)$). It is worth pointing out the necessity for $\boldsymbol{\lambda}_f$ involved in (4.62) to satisfy the condition

$$\boldsymbol{\lambda}_f = \left(\frac{\partial \boldsymbol{\chi}}{\partial \boldsymbol{x}_f} \right)^T \boldsymbol{\mu}_p \quad (4.63)$$

where $\boldsymbol{\mu}$ is the unknown vector that contains one element for each unconstrained state variable.

In [38] it is shown a sample of the width of cases where such conditions can be applied in addition to the $\boldsymbol{\chi}$ constrain equations, with the chosen set of conditions depending on which parameters are set free. However, some exceptions are pointed out. In fact if the target orbit has no inclination ($i = 0^\circ$) therefore the reduced transversality condition equation for both ω and Ω set free are not linearly independent so they cannot be used simultaneously (in fact it is not possible to define either ω or Ω for an orbit with inclination angle null). In a similar fashion conditions for both ω and ν set free are not linearly independent for orbits without any eccentricity (in fact it is not possible to define any periaxis in an orbit with $e = 0$ and therefore there is no reference to count the ν angle from) so they cannot be used simultaneously. For this thesis only reduced transversality equations for ν free have been used.

Capitolo 5

Case study: Near-Earth Asteroids (NEA) targeting and retrieval mission

During the last decade the increasing number of dedicated observation programs [43] (especially thanks to the improved IR observation technology along with the ground-based optical telescopes [3]) has brought to the discovery of an always higher number of asteroids whose orbital parameters are similar to the ones of the Earth that are called Near-Earth Asteroids (NEA) or Near-Earth Objects (NEO). The discussion about their exact definition will be faced in the section 5.1. The number of asteroids yearly spotted for their first time has continuously grown since 1995 when many of the actual observation programs have begun their activity (in the only year 2020 nearly 3000 new NEA were discovered) [43] and now, according with the last update made by NASA to its NEA database [37] on the 12/7/24, 35266 objects (864 with a diameter above 1 km and 10932 above 140 m) are reported, 58 more than the previous update made on the 1/7/24. The vast majority of the newly discovered bodies have a diameter in a range of [10, 140]m, but the vast majority of them is yet to be spotted (even among the bodies longer than 1 km, that are the easiest to spot because of their dimensions, it has been estimated that only 16% of the actual $D > 1\text{km}$ NEA have been discovered [7]).

There are many reasons of interest towards NEA.

From a scientific perspective they are seen as the specimen of the early stages of the life of the Solar System with their non-corrupted material that still has the composition and the characteristics of the early Solar System along with their being the remnants of ancient impacts between proto-planetary bodies [4]. They are also seen as the potential source, thanks to the frequent impacts (billions of years ago, luckily for us) of ancient fellows of theirs on the surface of other rocky planets like the Earth, of many of the chemical elements and compounds (like the organic ones and water) that are responsible for the formation of life on our planet ([4], [10] and [53]).

From an industrial point of view, asteroids are seen as a source of material that are very rare on the surface of the Earth's crust such as gold [55] along with platinum, iridium and palladium that are listed among the Platinum Group Materials (PGMs) [7]. In fact, in the early stages of the life of the Solar System the larger bodies that had a strong enough

gravitational pull were able to attract heavier materials towards the center of the planet when their mass was still not solid while smaller objects and other bodies that used to orbit further from the Sun (in what it is actually known as the Outer Solar System) cooled down too quickly getting frozen and did not have the time to do that. For this reason those very dense and very important materials in various industrial applications, being rare on the surface of the more massive bodies like the planets while abundant in their core, are rare on Earth above a certain depth in the ground. By the way, some of those proto-planets with their materials already gravitationally differentiated happened to collide between them fragmenting themselves in hundreds of smaller bodies so that now it is possible to discover asteroids made mainly of metals (the *M-type* asteroids) coming from the nuclei of one of those once planetary bodies already fully formed at the time of their destructive collision. On more, they are already into space so they can eventually be mined ([13] reviews some safe methods for both on Earth and in Space mining) to build components for spacecraft into space without launching them from the Earth so saving on the cost of the whole business.

Lastly, every asteroid that orbits the sun too closely to the Earth constitutes a danger for the planetary safety by itself. As [43] reports, when falling on the Earth an asteroid with $D \approx 15\text{m}$ can cause many damages to structures and people. In that regard it references to the famous example of the Chelyabinsk town in Russia where a 19-meters asteroid fell exploding in the air (before the impact on the ground) on February 15, 2013 and generating a shock-wave that shattered windows of buildings on a vast area around the origin of the explosion with nearly 1500 people injured (in prevalence with superficial wounds at their face because of the explosion of the glass they were facing, attracted by the bright glow they saw in the sky caused by the explosion itself that was the forerunner of the shock-wave). And this happened to be a very small body. Consequently, the bigger the asteroid, the more damages it can cause. This makes the planetary defense a major issue that has been addressed (mainly theoretically, up to now) through many possible solutions. Disruption techniques have been taken into account during the years, as [30] sums up, in order to face imminent threats (the use of waves of 100 or 250 penetrators, each one with a mass of 100 kg and 40 kg respectively with an expected 50% ratio of the total energy of the impactors going into the disruption of the asteroid, is described) along with deflection techniques through kinetic impactor (already tested with the AIDA DART mission, conducted by NASA, that in October 2022 successfully deflected the asteroid Didymos from its original orbit to another stable orbit through a spacecraft designed to impact its surface, [11]) that are able to preserve the integrity of the asteroid itself for potential future exploitation [35]. For small porous asteroids the disruption through nuclear weapons is also considered [3].

Many different space agencies have successfully attempted to reach NEA with dedicated missions, especially with sample return missions, such as OSIRIS-REx [33] (a sample return mission conducted by NASA focused on collecting 60g of material from the surface of the asteroid 101955 Bennu, also known as 1999RQ36, and on bringing it on the Earth for further analysis), the aforementioned AIDA-DART and the two missions Hayabusa-1 [25] (a mission sample return targeting the asteroid Itokawa, conducted by the Japanese Aerospace Exploration Agency (JAXA), in 2005) and Hayabusa-2 [22] (another mission sample return conducted by JAXA that landed successfully in June 2018 on the asteroid Ryugu to bring the collected material home on November 2019).

Also private investors (like the B612 Foundation [41]) are promoting studies aimed at

developing technologies and mission structures that can enable space agencies to intercept those asteroids from their own orbit to move them towards Earth Orbit (EO).

All the mathematical and computational tools so far described or developed have been applied to the resolution of a trajectory optimization problem aimed at designing an asteroid retrieval mission. Many redirection methods exist as they are collected by [3] in its overview: they can be perturbed gravitationally along their orbit as they are attracted by the mass of a spacecraft (the *gravity tractor* method) [29], pushed by the stream jet emitted by the ion-thruster of a spacecraft directed straight towards them (the *ion-beam* method) [8] or alternatively by one or more gimballed thrusters that can detumble and push it after having landed on it (the *tugboat* method, ideal for small diameter asteroids with $\Delta V < 200$ m/s) [41] while other methods that require provoking mass expulsion from the asteroid (the *mass driver* method) or sublimation of part of its constituent material through a focused beam of light (the *ablation* or *sublimation* method) [31] are also discussed there.

Also with regard to potential mission structures two main different approaches are presented in literature. In particular [23] describes and compares the strength and the weaknesses of a first potentially applicable mission structure that relies on one single spacecraft, the most represented one in literature ([1], [28] and others) that performs the whole mission, both the retrieval maneuver and the insertion in its final orbit closer to the Earth, and the second that relies on a two-spacecraft structure where the first one, the *pitcher*, deflects asteroids from their orbit through impulsive maneuvers that provide them the necessary ΔV to reach the orbit of the Earth, and a second spacecraft, the *catcher*, collects it and provides the required ΔV to stop it on the final orbit. In other words, the two spacecrafts provide to the asteroid the first and the second burn of a Hohmann's maneuver respectively.

For this thesis the transfer from Earth (specifically from the Sun-Earth L2 point) to the orbit of an asteroid (2013BS45, see table 6.3) has been analyzed through optimal trajectory calculations and comparing all the obtained families of potential solutions (and evaluating the feasibility of the lowest-TOF of them) to find the optimal maneuver to reach it. In the following section a potential mission structure made by a combination of the *tugboat* mission advantages (the use of an ion-thruster to provide slow but continuous push that guarantees the integrity of the asteroid to be kept rather than an impulsive maneuver that can disrupt it [41]) and the ones of the two-spacecraft mission structure proposed by [23] (two spacecraft can allow the *pitcher* to retrieve more mass because it does not have to perform the second burn of the mission) to complete the retrieval maneuver has been analyzed with the goal to maximize the amount of mass retrieved from the asteroid and delivered back to EO.

All the data about the position of the asteroid have been taken from NASA Ephemeris that are set into the J2000 system.

5.1 Asteroids selection process

In the recent years a great number of new asteroids has been discovered especially close to the Earth. For this reason a new category of bodies that orbit the Sun close to the Earth, the *Near-Earth Asteroids*, *NEA*. Many articles and other sources in literature, such as [3], [23], [28] and [52], define NEAs as those bodies which have orbital characteristics

similar to Earth. In particular [16] collects various categorizations already present in literature between NEA such as their distinction into four families, the *Atens* and *Apollos* whose orbits cross the orbit of the Earth, the *Amors* that always orbit around the Sun being outside of the Earth orbit and the *Atira* that orbit always inside of the Earth orbit. In order to make a selection of the bodies collected into the *JPL Small-Body Database* [37], as it was at the time of consultation (30th April 2024) we selected some parameters, given what has already been used in literature (such as the Brassier and Wiegert one, as reported by [16]), to isolate the closest bodies to the Earth:

- eccentricity less than 0.1, so their orbits can be considered as *quasi-circular*;
- semiaxis major in a range between 0.97 and 1.03 a.u.;
- inclination less than 2°, so their orbits should be as close as possible at being coplanar with the ecliptic plane;

while no distinction was made between *numbered* and *non-numbered asteroids*. According with those parameters 36 asteroids were selected.

The second selection phase was conducted to rank them by the necessary ΔV to reach it with a spacecraft from Earth. This pruning phase was conducted as in many works in literature ([16], [48] and others) where the two-impulse Hohmann's manoeuvre was used as a reference. The change of inclination of the orbital plane was considered combined with the variation of the semi-major axis according with the following equation (assuming that the plane change is performed starting from 0° of Latitude so therefore no rotation of the line of the nodes is generated and that all the orbits are circular)

$$\Delta V = \sqrt{\Delta V_1^2 + \Delta V_2^2 - 2V_1V_2 \cos(\alpha\Delta i)} \quad (5.1)$$

where Δi is the variation of inclination of the orbital plane and α is the fraction of the overall Δi that is performed inside the first burn of the whole Hohmann's manoeuvre (the remaining $1-\alpha$ is performed with the second one so its cost is reduced because it is performed further from the central body). A difference between bodies closer to the Sun and further from it than Earth was made because a penalty for bodies whose semi-major axis was less than the Earth's one would have been created so $\alpha=0.1$ was used for asteroids further from the Sun than Earth while $\alpha=0.9$ was employed for the ones closer in order to always perform 90% of the variation of i further from the Sun.

As a result, twenty asteroids with ΔV below 1 km/s were selected for further calculation. The complete list of the selected asteroids has been reported in appendix B while their orbits in comparison with the one of the Earth are shown in fig. 5.1.

It is worth noticing that even using similar parameters to [16] the list of the selected asteroids is much longer (only 10 NEA were selected) with only few of them in common with the list of asteroids selected for this thesis. This is because that study was made in 2013 so many NEA considered for this thesis were yet to be spotted (in tables B.1, B.2 and B.3 it is possible to notice by their recording name how many of those NEA have been discovered in the last 10 years).

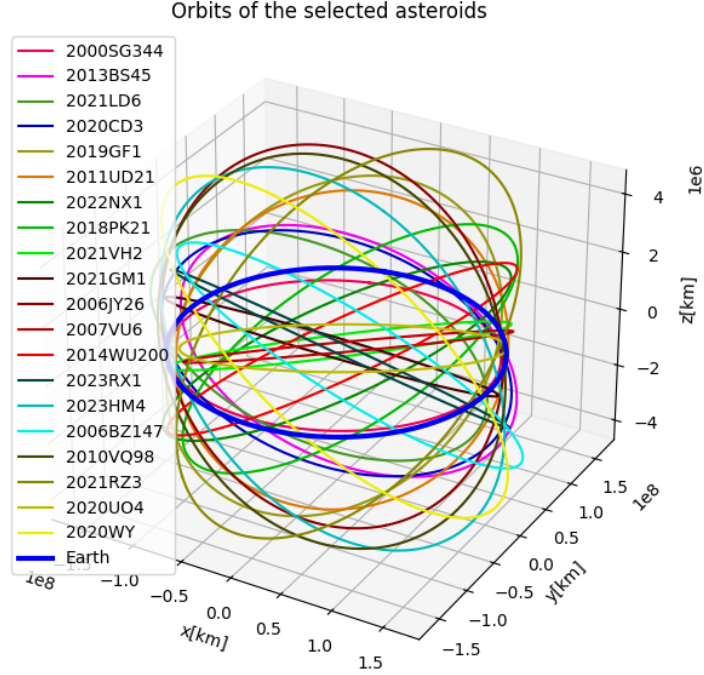


Figura 5.1: Orbits of the selected NEA

5.1.1 The estimation of the asteroid mass and diameter

In order to define the asteroid mass, given the difficulties in spotting NEA because of their rocky and so therefore light-absorbing nature that leads to a general lack of physical data, the following equations found in literature ([16], [19], [28], [48] and others) were used to estimate their mass and diameter.

$$m_{ast} = \frac{\pi}{6} \rho \left(\frac{1.329 \cdot 10^6}{\sqrt{p_v}} 10^{-\frac{H}{5}} \right)^3 \quad (5.2)$$

$$D = 1329 km \times H^{-1/5} p_v^{-1/2} \quad (5.3)$$

where H is the apparent magnitude of the observed NEA (taken from JPL's NEA database), p_v is its albedo and ρ is the density of the asteroid (that [48] assumes in a range between 1300 kg/m^3 for porous objects called *S-class asteroids* and 5300 kg/m^3 for metallic objects called *M-class asteroids*, so that for every asteroid a minimum and a maximum mass are reported).

The aim of those calculations is not only to evaluate how much mass composes them and therefore how much material we can retrieve from them, but also to understand, as [16] points out, how heavily they can be gravitationally perturbed by the Earth itself during a close encounter that can occur when they reach an alignment in relation with the sun during their orbit (it should happen when their orbits are at one of their closest

points but considering the overall general proximity between the orbit of every NEA and the orbit of the Earth we can assume it as a possibility that limits the theoretical feasibility of the mission, with this limit that should be studied more in depth in future studies).

All those results are collected in appendix B and show how, with an albedo chosen in a range between 0.05 (very dark object) and 0.50 (very bright object), all the considered bodies from the JPL small-bodies database have a very small diameter in a range [1 – 50]m showing how high Earth gravitational influence can be on their orbital parameters and therefore how important considering maneuvers that can take a TOF that is shorter than the Δt to the next close encounter can be.

Capitolo 6

Results

6.1 Trajectories from Earth to 2013BS45

In order to validate the mathematical Python code written to perform these optimization calculations the asteroid 2013BS45 has been chosen among the selected NEA (after the pruning process discussed in section 5.1). The goal of the calculations presented in this section is to find the optimal trajectory (in order to minimize the mass of propellant utilized) to reach the asteroid orbit targeting the TOF and the true anomaly that allow to reach the asteroid itself (so those parameters are both fixed).

In order to make these calculations some assumptions were made. The dynamical system used is a *two-bodies system* where all the gravitational influences from third-bodies were neglected while the launch has been assumed to be performed from the Sun-Earth L2 point, so the initial values of the velocity components in relation with the Sun in the Heliocentric-Ecliptic reference frame have to be obtained from the ones of the Earth through a proportion considered the increased distance from the Sun as in (6.1) (this because L2 is a point in space that is always perfectly aligned with the Sun and the Earth so it is not orbiting on its own independent orbit) where the distance between the Sun-Earth L2 point and the Sun is given by summing 1 to the result of (2.65) and then multiplying it by the Sun-Earth distance (1.496×10^8 km) and so it is 1.511×10^8 km.

$$\mathbf{x}_{L2} = \mathbf{x}_{Earth} \left(\frac{r_{L2}}{r_{Earth}} \right) \quad (6.1)$$

The spacecraft is assumed to have an initial wet mass of 5000 kg (2000kg of dry mass, according with the example of mass distribution presented by [16], without any payload given the absence of any in-situ scientific purpose beside the collection of the most possible mass from the targeted asteroid) and is pushed by 35 ion-thrusters producing 25mN each (with a total thrust of 785mN) and $I_{sp} = 2000$ s (see [9] and [24]). However, considering that the average life of a ion-thruster is less then 10000 hours (less than 1.5 years) a set of back-up thrusters must be considered to be able to rely on the maximum level of thrust in every moment of the mission. All these values are collected by table 6.1. The choice of using such a small spacecraft if compared to the one considered for analogous missions ([23]) has been made to allow multiple similar missions to be launched in sequence towards the same asteroid with the possibility to use electrical propulsion and less powerful launcher at the beginning of the mission.

m_{weto} [kg]	m_{dry} [kg]	m_p [kg]	$n_{ion\ thrusters}$	Thrust [N]	I_{sp} [s]
5000	2000	3000	35	0.875	2000

Tabella 6.1: Spacecraft characteristics at the beginning of the transfer towards 2013BS45

All the optimal trajectories in this section are referred to the launch date of September the 1st, 2024 that has been arbitrarily chosen as the starting date (see table 6.2) and have the Near-Earth Asteroid 2013BS45 as their final destination.

date	a [AU]	e	i [°]	Ω [°]	ω [°]	ν [°]
1/9/2024	1	0.017	0	348.74	114.21	237.54

Tabella 6.2: Keplerian parameters of the starting point of all the trajectories described in this chapter

The calculations for an optimal trajectory towards 2013BS45 have led towards the finding of two separate families of solutions where the first is called *principal family* because its solutions are related with a minor amount of propellant mass consumed and the second is called *secondary family* because their mass of propellant consumed is higher than the principal family.

Each family is composed of a sequence of solutions (each one targeting a different value of true anomaly on 2013BS45 orbit) that show the amount of propellant mass spent to get to the targeted orbit for ν values that are progressively further than the one that can be reached at the moment of the rendez-vous with the asteroid through a transfer whose switching function is completely positive (so therefore it is impossible to target a lower ν because even with always active thrusters it would be impossible for the spacecraft to reach it fulfilling the imposed time constraint). All the other solutions progressively rely on coasting for a greater portion of their mission time the further away the targeted point of the orbit is in front of the ν of the least-TOF rendez-vous (with a consequently greater saving of propellant).

Calculations have been conducted in both cases through a procedure of guessing to elaborate a set of initial conditions for the spacecraft (given the Keplerian parameters for the starting and arrival point), especially regarding the set of initial costates for the state variables, and then launching the calculations in order to guide it towards convergence to a solution through many attempts to improve the set of initial condition trying to understand how the initial adjoint variables influence the resulting optimal trajectory. As a result, it can be noticed that the adjoint variables of the position coordinates (λ_x , λ_y and λ_z), being the only variables influencing the differential equation for the components of the primer vector (λ_{v_x} , λ_{v_y} and λ_{v_z} , as shown in appendix A), have a strong influence on λ_V and therefore also on the switching function values. In fact, the higher λ_x , λ_y and λ_z , the higher the values of the switching function (and the length of the traits along the time dominion of the \mathcal{S}_F itself where it is positive) are and so therefore the tendency of the solution is to converge towards a maneuver with longer thrust arcs. On the other hand, higher initial values for the adjoint variables of velocity components lead to a higher tendency for the thrust to be directed with greater angles from the direction tangential to the followed trajectory (given the dependence of the thrust angles α and β with λ_{v_x} , λ_{v_y} and λ_{v_z} as shown in (4.59) and 4.60). As an example, if we choose to launch towards

name	H	e	a [AU]	i [°]	Ω [°]	ω [°]
2013BS45	25.9	0.0838	0.9915	0.77	83.4	150.74

Tabella 6.3: Characteristics of 2013BS45, part 1

name	r_p [AU]	r_a [AU]	v_c [km/s]	ΔV [km/s]	M_{max} [kg]	T [days]	d_{max} [m]
2013BS45	0.9084	1.0746	29.89	0.44	1.50E07	361	39.27

Tabella 6.4: Characteristics of 2013BS45, part 2

2013BS45 using too low values for λ_x , λ_y and λ_z and too high values for λ_{v_x} , λ_{v_y} and λ_{v_z} we have that the code tries to converge towards a trajectory that will not manage to reach the desired point of the targeted orbit because of the strong steering tendency of the thrust, brought by the high values of the adjoint variables of the components of velocity (with errors in the order of 10^8 or more in non-dimensional terms), that will result in a trajectory that will spiral towards the Sun as shown in fig. 6.1 obtained through the following set of initial costates.

$$\boldsymbol{\lambda}_0 = \{\lambda_x, \lambda_y, \lambda_z, \lambda_{v_x}, \lambda_{v_y}, \lambda_{v_z}, \lambda_m\} = \{0.2, 0.2, 0.2, 0.8, 0.8, 0.8, 1\}_0^T \quad (6.2)$$

On the contrary, if initial λ_x , λ_y and λ_z are too high and λ_{v_x} , λ_{v_y} and λ_{v_z} are too low we have very long thrust arcs with little steering so the vast majority of the thrust is directed along the tangential direction to the orbit and so the resulting trajectory tends to diverge towards the outer solar system as in fig. 6.2 obtained through the following set of initial costates.

$$\boldsymbol{\lambda}_0 = \{\lambda_x, \lambda_y, \lambda_z, \lambda_{v_x}, \lambda_{v_y}, \lambda_{v_z}, \lambda_m\} = \{0.6, 0.6, 0.6, 0.2, 0.2, 0.2, 1\}_0^T \quad (6.3)$$

So finding the right guess becomes a matter of finding the right balance between length of the thrust arcs and thrust steering. In this case the chosen target (in fixed-TOF and fixed- ν conditions) for the so far attempted maneuver was $\nu = 86^\circ$ for TOF = 633 days, in other words we targeted the rendez-vous with 2013BS45 on the 27th of May 2026 with the launch supposed to happen on the 1st of September 2024. So we were aiming at a transfer that relies on a complete revolution around the Sun that therefore requires more direction control than thrust-time. As a consequence, a set of guesses that finally successfully brings the solution to a convergence in 2457 iterations (see table 6.20) is the following.

$$\boldsymbol{\lambda}_0 = \{\lambda_x, \lambda_y, \lambda_z, \lambda_{v_x}, \lambda_{v_y}, \lambda_{v_z}, \lambda_m\}_0^T = \{0.37, 0.37, 0.37, 0.75, 0.75, 0.75, 1\}_0^T \quad (6.4)$$

where the velocity components costates are higher than the position ones (but are only 2 times higher so they create a more balanced guess than the one described in (6.2)) and the solution is represented in figs. 6.3, 6.4 and 6.5.

A recurrent feature of all the sets of initial costates that lead to a convergence is the value chosen for λ_m that is always set to 1. In fact, the goal of those calculation is to optimize the mass at the end of every integration arc to obtain the optimal final mass at the end of the whole integration so it is preferable to set its initial guess value to 1 and

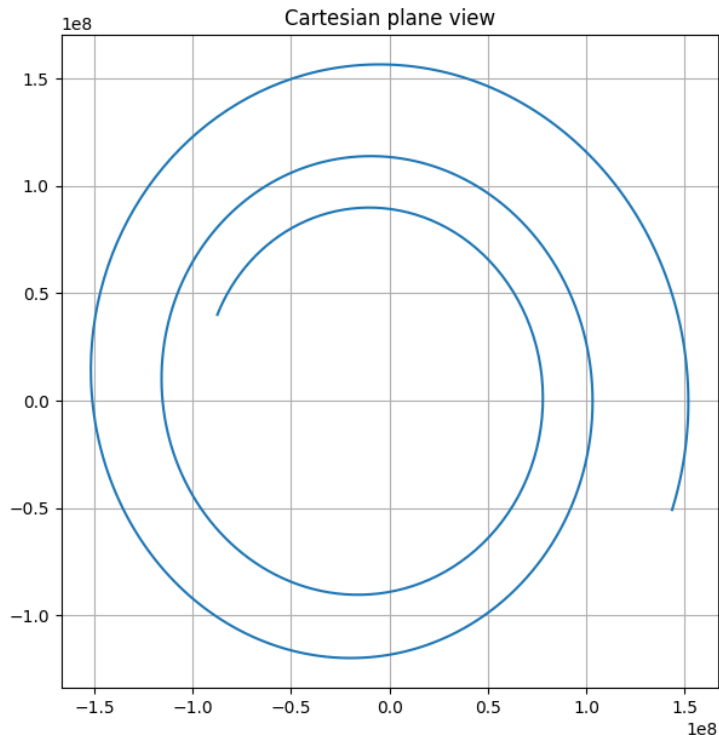


Figura 6.1: Trajectory resulting from a failed convergence process with too high initial costates on velocity components

then let the optimizer to find its optimal value according with the constraint over the mission TOF. In fact, the more time is available to complete the transfer, the less time will be necessary for the thrusters to push so consuming mass of propellant and so the higher the optimization will be possible since the earliest stages of the transfer (therefore, the resulting optimal initial λ_m will tend to be closer to 1).

Once the first convergence has been reached it is straightforward to find many other converging solutions using the optimal initial costates vector λ_0^* just obtained as an initial guess for targeting slightly different values for TOF and ν from the ones targeted with the solution just converged.

The principal family is composed of solutions about rendez-vous maneuvers with 2013BS45 which span from November 16th, 2025 to January 27th, 2027 while the secondary one spans from November 4th, 2026 to September 26th, 2027. So we have an over-lap between their time-spans that allows a better comparison between the two of them in a following subsection.

6.1.1 Principal family of solutions for 2013BS45 rendez-vous

The first family of solutions was found starting from the already presented 633-days long transfer to rendez-vous 2013BS45 on the 27th of May 2026. By progressively diminishing the targeted ν (and targeting the TOF obtained by considering the launch happening on

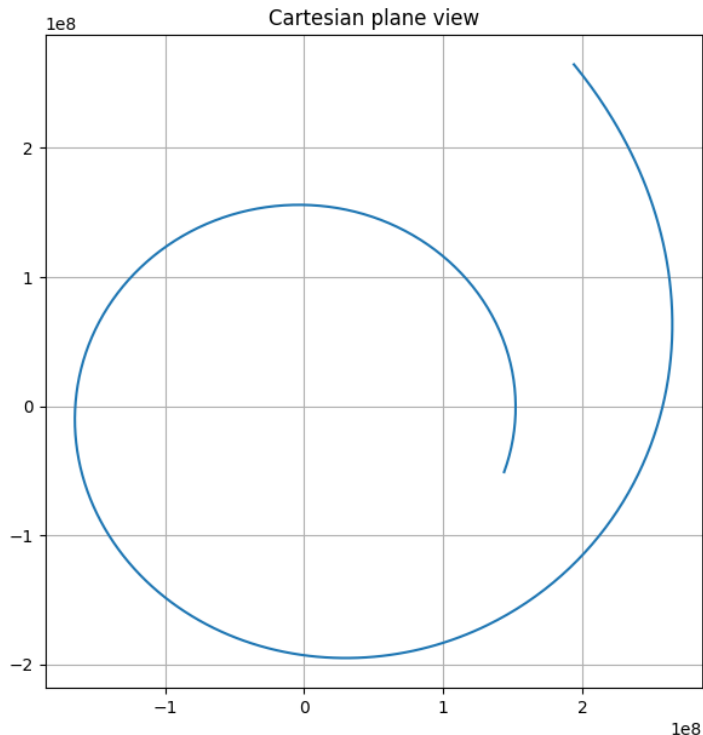


Figure 6.2: Trajectory resulting from a failed convergence process with too high initial costates on position components

the 1st of September 2024 and the arrival on the day of the transit of the asteroid at the targeted value of true anomaly as indicated by the NASA Ephemeris for 2013BS45 consulted on the 7th of June 2024 on [37]) it was possible to find solutions for shorter-TOF transfers (with also longer thrust arcs and therefore higher mass of propellant spent) until the solution for the transfer targeting the rendez-vous on the 16th of November 2025 (a 441-days long transfer) that, as it is shown in fig. 6.8, has $\mathcal{S}_F > 0$ for the whole duration of the maneuver so being the shortest-TOF one among the maneuvers of this family that lead to a rendez-vous with the asteroid (see also figg. 6.6 and 6.7).

If we increase the targeted ν and therefore the necessary TOF to rendez-vous 2013BS45 we can continue the sequence of solutions that reach convergence until a region of the asteroid orbit where the code does not manage to reach convergence. The last solution obtained is the transfer towards $\nu = 122.82^\circ$ in a TOF = 671 days represented in figg. 6.10, 6.11 and 6.12 shows how the 3D representation really looks like if we use the same scale on all three axes while for sake of visualization the scale on the z-axis is 2 orders of magnitude smaller than the one used for the x and y-axis). From that solution to the next one that successfully converges (the transfer that targets $\nu = 170.14^\circ$ and has TOF = 693 days) there is a region of nearly 48° of the targeted orbit where the optimizer does not find any convergence. This is a problem that can be related with the starting point of the maneuver. In fact this region of the targeted orbit (see fig. 6.9) has similar coordinates in the x,y -plane to the Sun-Earth L2 point at the moment of the launch (as shown in figs.

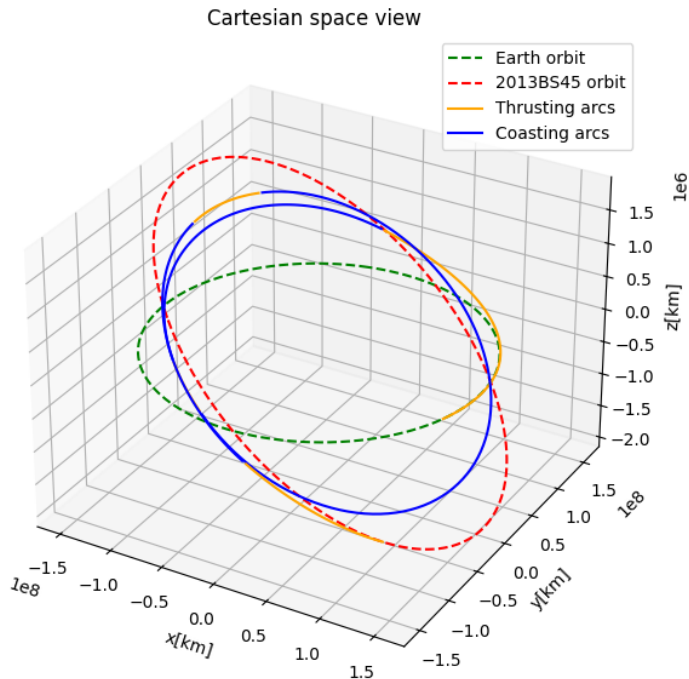


Figura 6.3: 3D optimal transfer towards 2013BS45 with rendez-vous on May 27th, 2026

6.10 and 6.11) so this makes the maneuver itself impossible.

Targeting the same ν of the orbit of 2013BS45 with a maneuver starting from Sun-Earth L2 on another day (on the 4th of January 2025 whose coordinates on the x,y -plane are far from the ones of the targeted point, as in figs. 6.21 and 6.22) is the way to demonstrate how the issue causing the lack of convergence is the relation between the coordinates of the starting and the final point of the transfer.

After this "hole" with absence of converging solutions that ends with the rendez-vous on the 26th of August 2026 ($\nu = 170.14^\circ$ and TOF = 725 days, see figs. 6.13, 6.14 and 6.15) from that another wide group of converging solutions can be found for the various true anomaly values until $\nu = 300.12^\circ$ (where the convergence is there obtained for TOF = 865 days with the rendez-vous happening on the 14th of January 2027, see figs. 6.16, 6.17 and 6.18) after that no convergence can be reached once again. Those regions of 2013BS45 orbit that cause those issues are the ones with the highest vertical distance (along the z -axis) from the ecliptic plane and therefore from the plane of the orbit of the Earth around the Sun (that is the plane the spacecraft has to be launched from). This means that those regions are the most demanding ones in terms of thrust along the vertical direction of the heliocentric-ecliptic reference frame so this may bring difficulties in defining the necessary switching function. For future research more calculation about transfers that target further ν values that belong to this family of solutions can impact positively on the comprehension of this numerical phenomenon.

The second group of solutions has been found starting from the rendez-vous found for

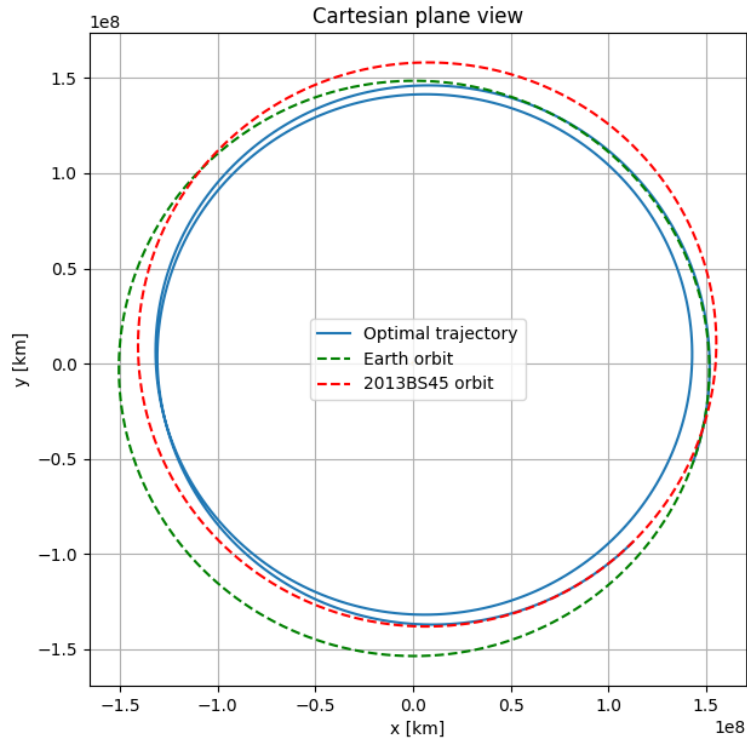


Figura 6.4: 2D optimal transfer towards 2013BS45 with rendez-vous on May 27th, 2026

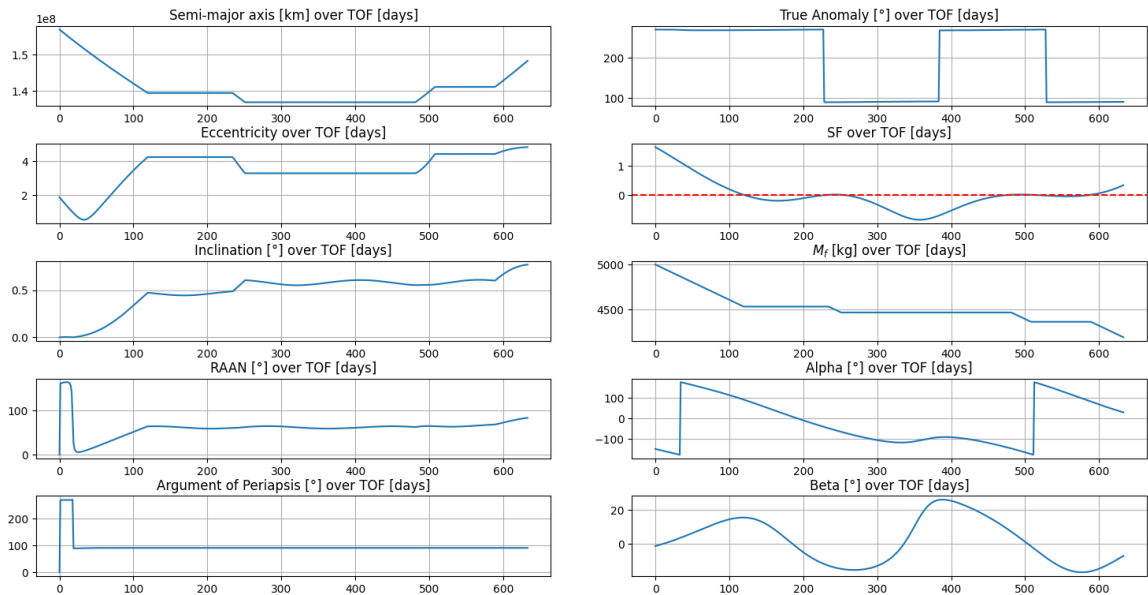


Figura 6.5: Orbital, angular and thrust data from maneuver for rendez-vous with 2013BS45 on May 27th, 2026

$\nu = 228.77$ (happening on the 3rd of November 2026 after TOF = 793 days) thanks to the following set of initial costates

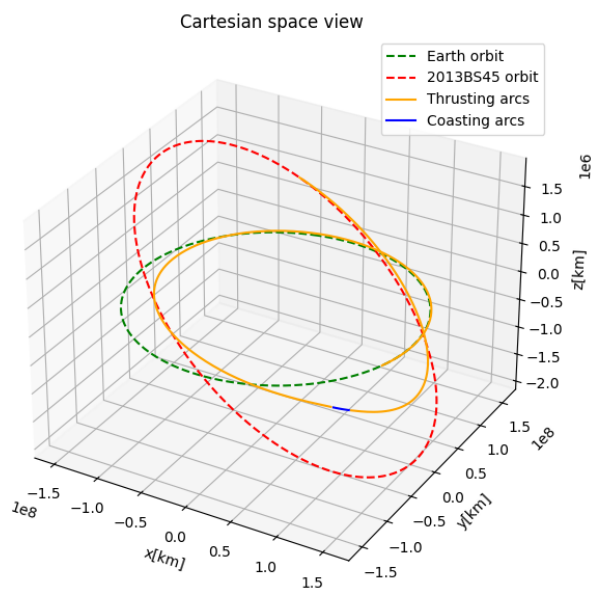


Figura 6.6: 3D optimal transfer towards 2013BS45 with rendez-vous on November 16th, 2025

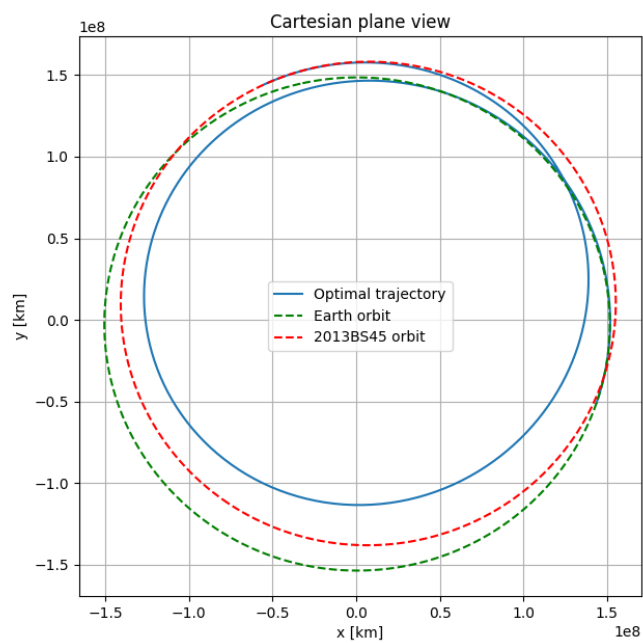


Figura 6.7: 2D optimal transfer towards 2013BS45 with rendez-vous on November 16th, 2025

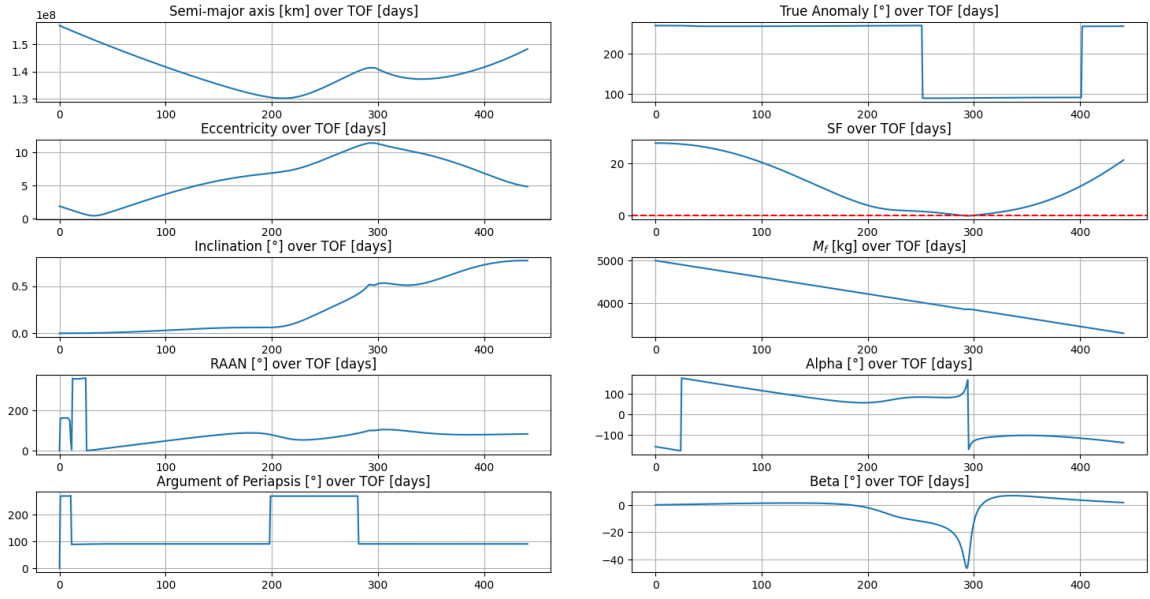


Figure 6.8: Orbital, angular and thrust data from maneuver for rendez-vous with 2013BS45 on November 16th, 2025

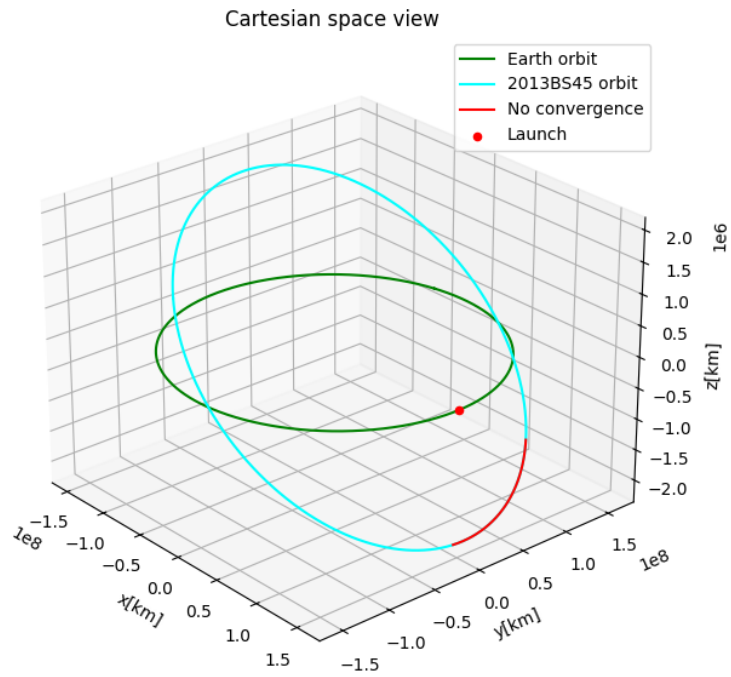


Figure 6.9: Arc of the 2013BS45 orbit where no convergence has been found

$$\lambda_0 = \{\lambda_x, \lambda_y, \lambda_z, \lambda_{v_x}, \lambda_{v_y}, \lambda_{v_z}, \lambda_m\}_0^T = \{0.42, 0.42, 0.42, 0.75, 0.75, 0.75, 1\}_0^T \quad (6.5)$$

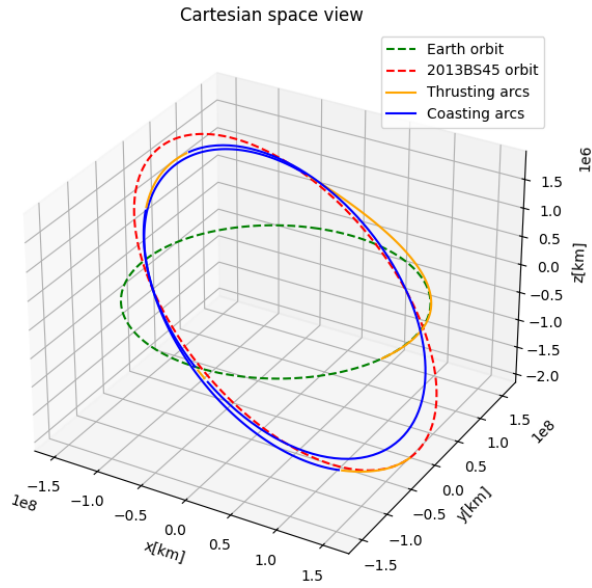


Figura 6.10: 3D optimal transfer towards 2013BS45 with rendez-vous on July 4th, 2026

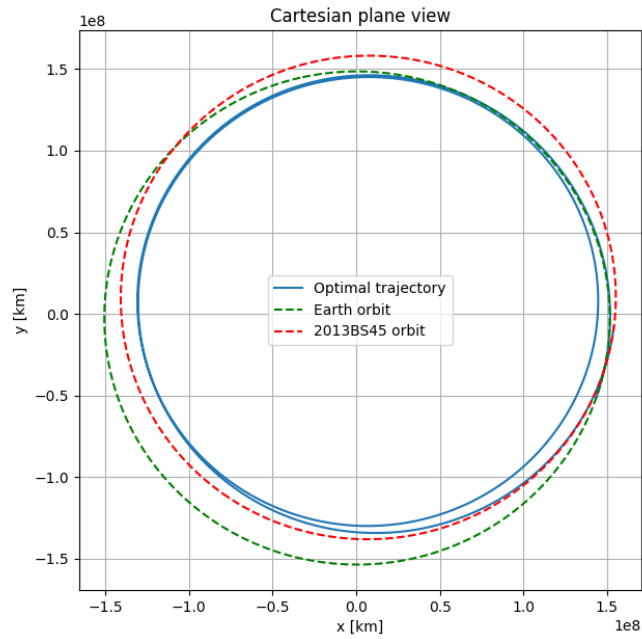


Figura 6.11: 2D optimal transfer towards 2013BS45 with rendez-vous on July 4th, 2026

that has higher position costates than the ones in (6.4) meaning that from the initial condition we are pushing the optimizer towards solutions with a higher portion of the TOF with $\mathcal{S}_F > 0$ and that can help to find convergences more easily if, compared with

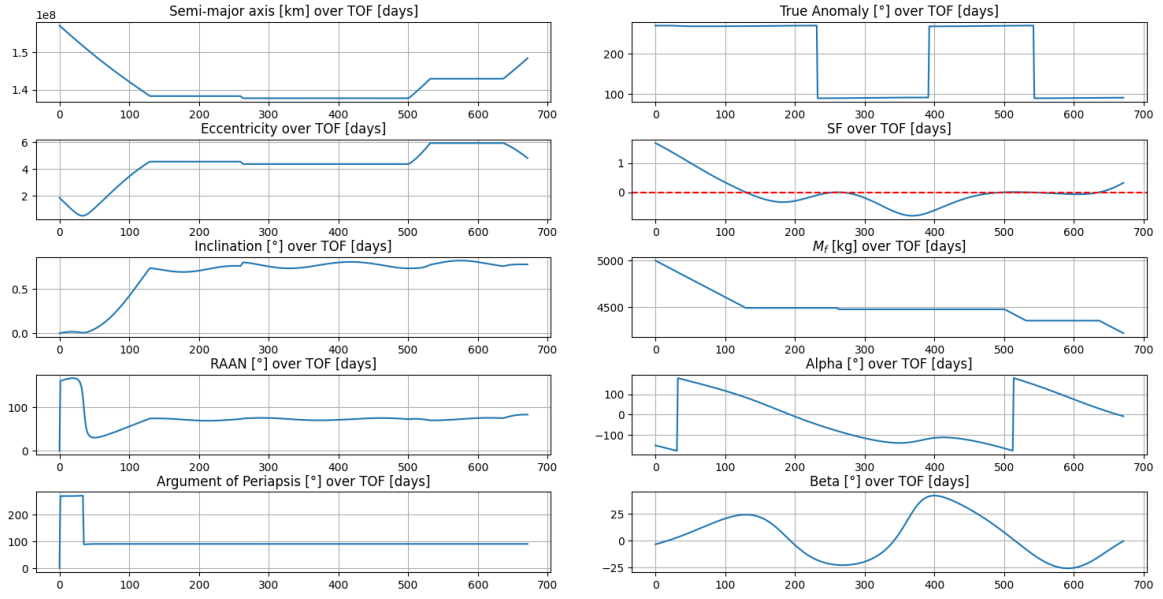


Figure 6.12: Orbital, angular and thrust data from maneuver for rendez-vous with 2013BS45 on July 4th, 2026

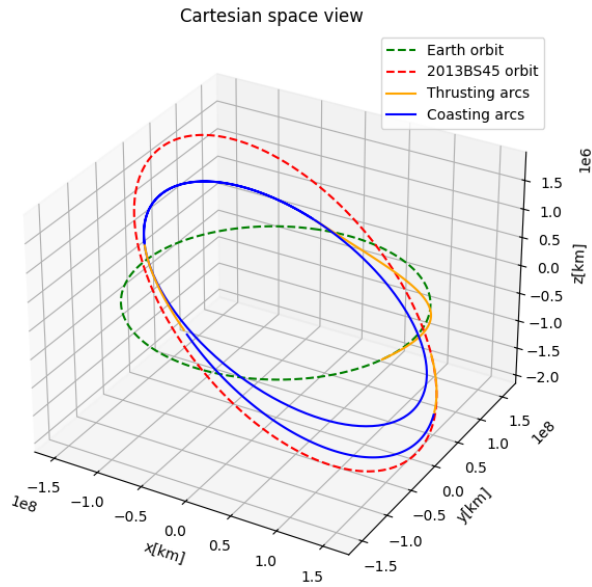


Figure 6.13: 3D optimal transfer towards 2013BS45 with rendez-vous on August 27th, 2026

6.4, the targeted ν is further than the previously targeted one with a higher TOF that has received a smaller increment if compared with the one on ν . In facts, if we try to go further in space but with a smaller increment of time allowed to get the rendez-vous we are forced to push more and so therefore we need higher portions of the \mathcal{S}_F being positive.

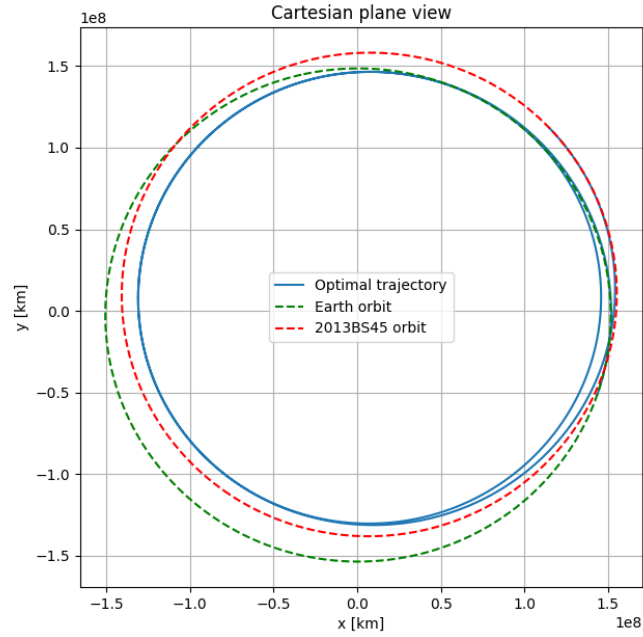


Figura 6.14: 2D optimal transfer towards 2013BS45 with rendez-vous on August 27th, 2026

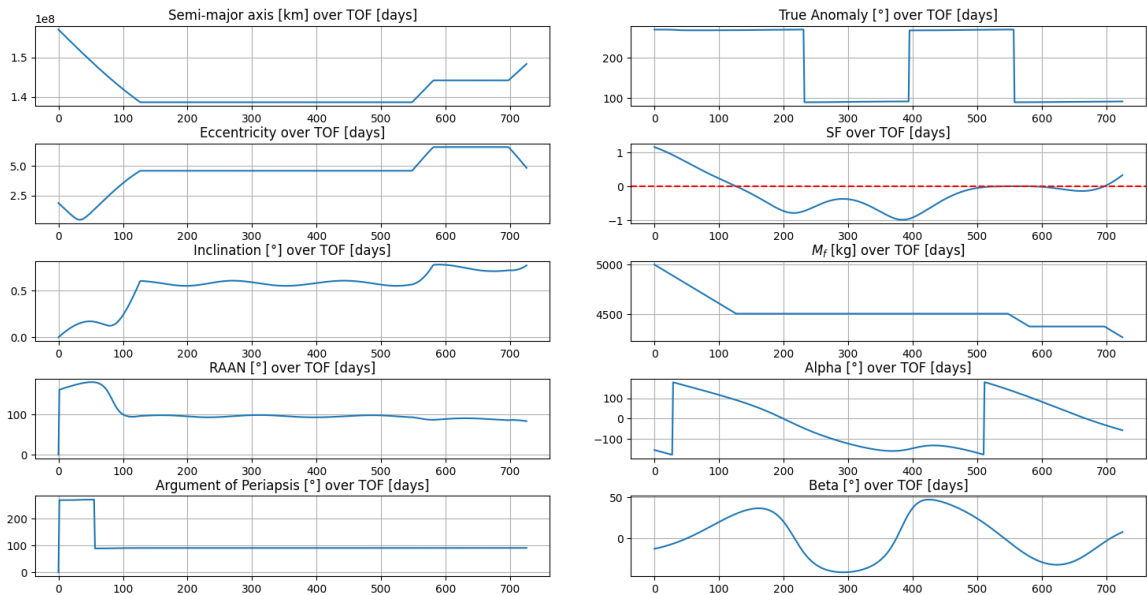


Figura 6.15: Orbital, angular and thrust data from maneuver for rendez-vous with 2013BS45 on August 27th, 2026

For all the obtained solutions the fraction of the initial mass of the spacecraft that reaches the rendez-vous has been calculated and recorded and give the fact that the solutions of the second group follow the trend established by the solutions of the first group can justify the conclusion that those two groups of solutions, even though they

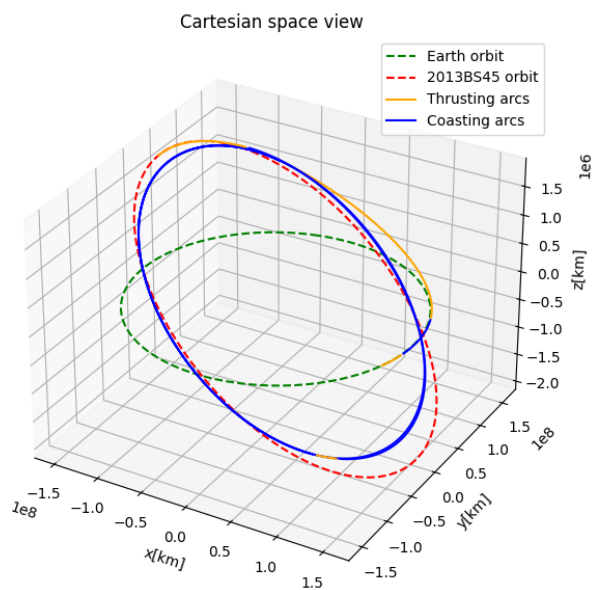


Figura 6.16: 3D optimal transfer towards 2013BS45 with rendez-vous on January 14th, 2027

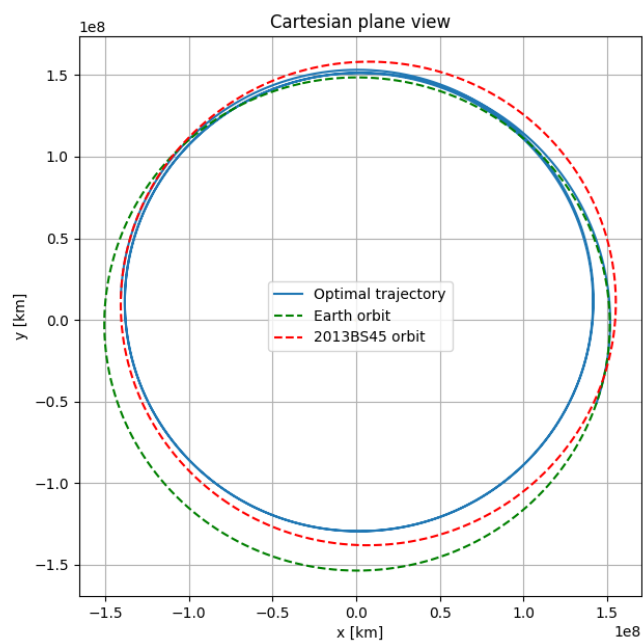


Figura 6.17: 2D optimal transfer towards 2013BS45 with rendez-vous on January 14th, 2027

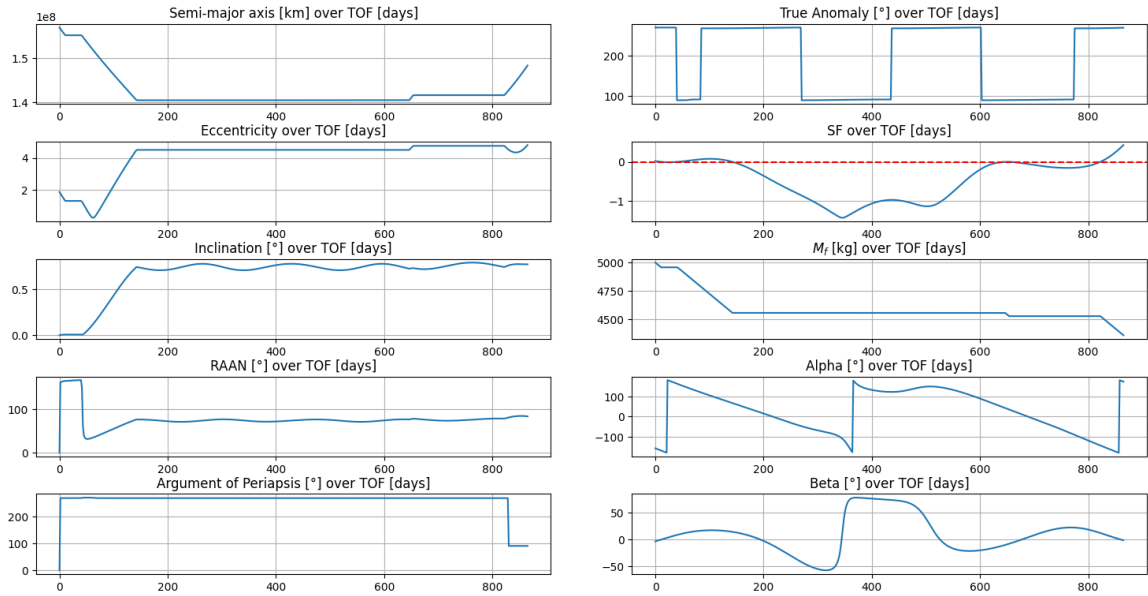


Figure 6.18: Orbital, angular and thrust data from maneuver for rendez-vous with 2013BS45 on January 14th, 2027

have been found separately, are part of the same family.

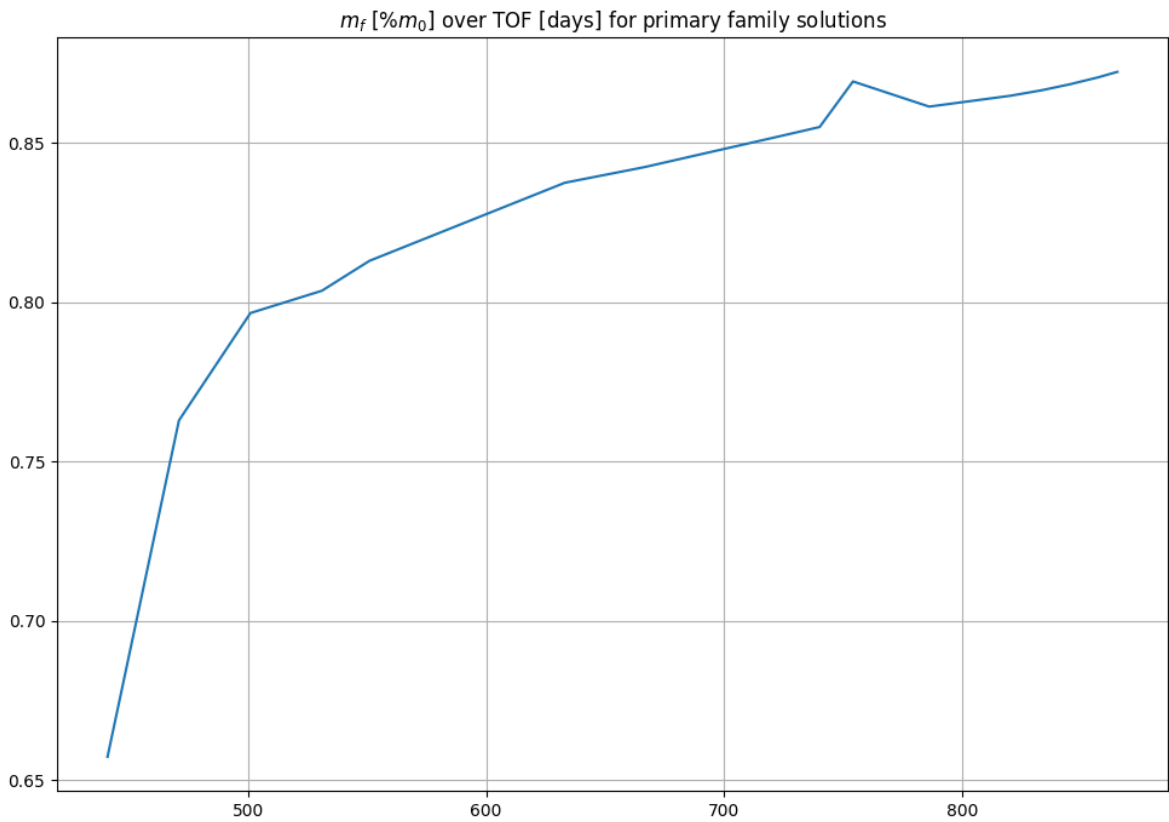


Figure 6.19: Values for m_f over TOF for trajectories among the primary family of solutions

ν_f [°]	arrival	TOF [d]	m_f (% m_0) [kg]	m_p (% m_{p0}) [kg]	day with $\mathcal{S}_F > 0$	figure
236.61	16/11/25	441	3286.5 (65.73%)	1286.5 (42.88%)	435 (98.6%)	6.6
86.00	27/5/26	633	4187.5 (83.75%)	2187.5 (72.92%)	246 (38.8%)	6.3
122.82	4/7/26	671	4216.0 (84.32%)	2216.0 (73.87%)	200 (29.8%)	6.10
170.14	27/8/26	725	4261.5 (85.24%)	2261.5 (75.38%)	188.5 (26.0%)	6.13
300.12	14/1/27	865	4361.5 (87.23%)	2361.5 (78.72%)	166.1 (19.2%)	6.16

Figura 6.20: Primary family maneuvers

When looking at figs. 6.8, 6.12, 6.15 and 6.18 it is possible to notice how generally all the solutions belonging to this family have a long first trait of their TOF (initially about 100 days long, its length decreases the further the targeted ν is from the one targeted by the quickest maneuver of this family) where the switching function is positive and decreasing so indicating the convenience the optimizer finds in pushing for the whole first part of the transfer to begin the plane change maneuver as soon as possible. After that, we can observe a plateau that, progressing with the increment of the targeted ν (fig. 6.33), begins to turn into a succession of a new peak and a subsequent valley. This adds a new thrust arc that is then followed by another one forming by deformation of the subsequent plateau (see fig. 6.36 where the remnants of the third arc that is part of the \mathcal{S}_F of the failed convergences of the region $\nu = [122.82 \ 170.14]^\circ$ are visible) while another omnipresent feature in switching functions for solutions in this family is the thrust arc on the final trait.

The first thrust arc is the crucial one for the necessary plane change because 2013BS45 has a closer orbit to the Sun so the optimal maneuver in that regard is the one performed the furthest possible from the Sun itself. In fact, this first thrust-arc contributes to reduce the semi-major axis of the orbit ($\alpha = -180^\circ$ at the beginning of the transfer so the spacecraft is braking to reduce the semi-major axis) so making the plane change maneuver more expensive ΔV wise. In the following stages of the transfer the in-plane direction of the thrust changes pointing towards the outside, then in front and then inside the trajectory in the attempt to vary the eccentricity of the orbit while generally the final thrust arc sees α close to 0° to make the necessary final correction of the semi-major axis to finally reach the targeted orbit.

The arc of absence of convergent solutions

As previously said, there is an arc of the orbit of the asteroid 2013BS45 where the code does not manage to find any convergent solution for maneuvers that start from Sun-Earth L2 point on the 1st September 2024 (see fig. 6.9).

The issue has been investigated in the context of this thesis in order to formulate an hypothesis about the causes of this behavior of the code.

In order to determine weather the issue is related to the starting point of the trajectory or not, the rendez-vous with 2013BS45 on the 26th July 2026 is targeted with a maneuver starting from Sun-Earth L2 point on another date. In this case the 4th of January 2025 has been chosen and the code manages to successfully bring a solution to convergence as shown in figs. 6.21 and 6.22.

If we repeat the process trying with the 1st of September 2024 we get no convergent solution, so the issue has to be related not with the starting point or with the arrival point

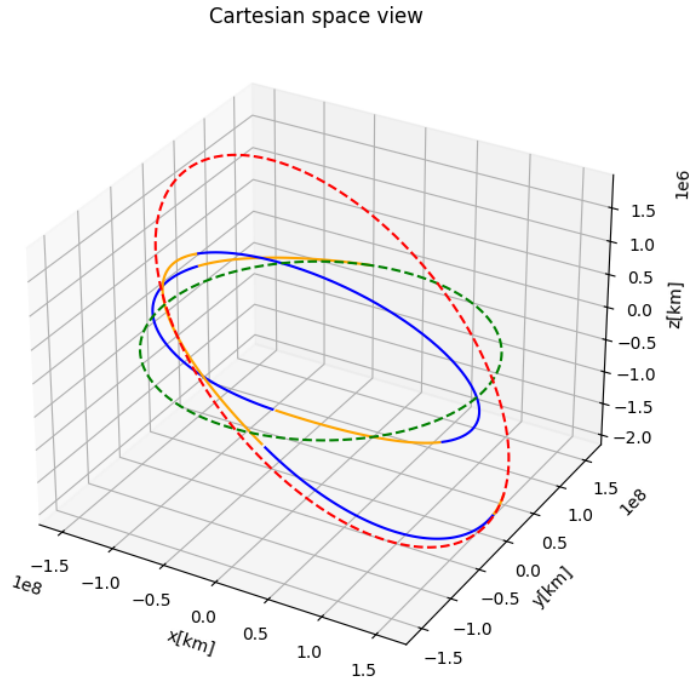


Figura 6.21: 3D optimal transfer towards 2013BS45 starting on January the 4th, 2025 with rendez-vous on July 26th, 2026

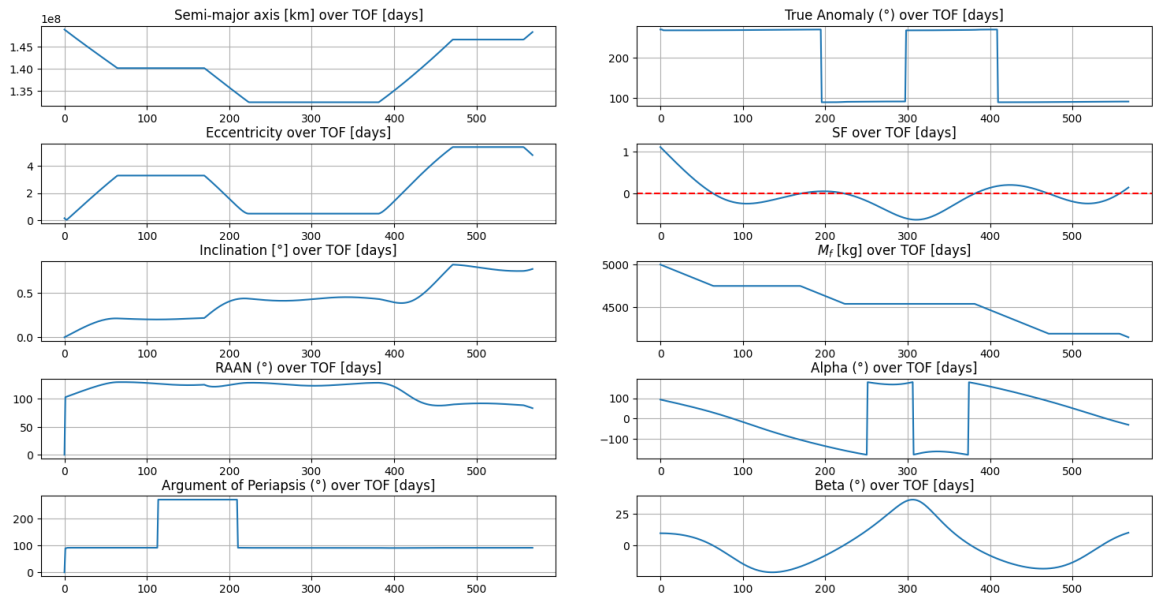


Figura 6.22: Orbital, angular and thrust data from maneuver starting on January the 4th, 2025 for a rendez-vous with 2013BS45 on July 26th, 2026

alone but with the relation existing between them. If we analyze the relation between the starting and the arrival point in the maneuver from Earth Orbit (on the 1st of September 2024) to 2013BS45 orbit (on the 26th of July 2026) it is possible to notice that the targeted point in the final orbit has a quadratic phase with the line of the nodes of the targeted orbit and also the starting point of the maneuver on the orbit of the Earth has a quadratic phase with it. So targeting that arc of 2013BS45 orbit from an Earth position around the one at 1st of September 2024 means that the spacecraft has to reach the zone of the targeted orbit with the highest vertical distance from the ecliptic plane where the orbit of the Earth fully lies, so that it can seem problematic for the optimizer to conjugate the need to have a greater vertical component for the thrust with the necessity to minimize the m_p spent. On more, we can notice from fig. 6.11 how the targeted position is in a region that, on the x - y plane, is slightly in front of the starting position of the spacecraft. For this geometrical reason the optimizer finds the direct maneuver as a potential solution that because of its minor TOF and therefore because of its m_p spent seems to be the best. However, how it will be shown in section 6.1.3, the minimum-TOF maneuver (obtained setting TOF free and so without targeting an actual rendez-vous with the asteroid but targeting the 2013BS45 orbit alone at the nearest ν possible) allows to target values for ν that are much further than the one where the asteroid will be on the 26th of July 2026, even by having $\mathcal{S}_F > 0$ for the whole maneuver, so that the optimizer will never be able to find a convergence for a solution on that maneuver, that if possible would be the most convenient, and will get to a singular jacobian matrix because of the huge discrepancies which will be generated because of this process.

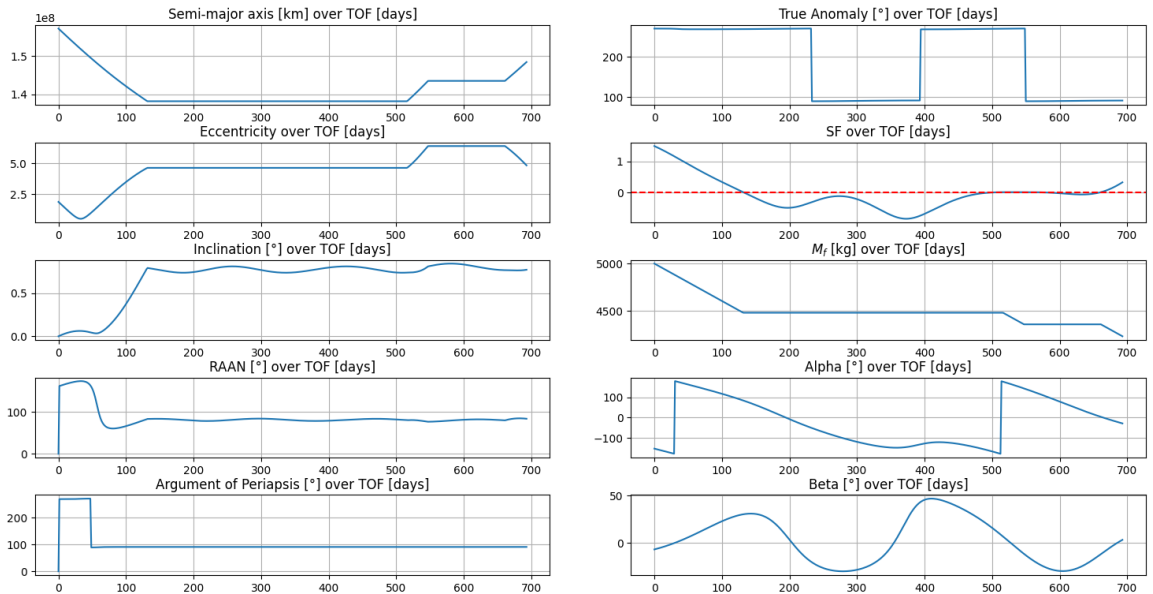


Figura 6.23: Data from the diverging solution for the transfer towards 2013BS45 (attempted rendez-vous on 26th July 2026) before the first use of the pseudo-inverse of the Jacobian matrix

If we consider data from the state variables and the obtained functions (such as \mathcal{S}_F and the thrust angles) we can notice that the first attempt made by the optimizer is to reduce the length of the thrust arcs minimizing the m_p as shown in fig. 6.23 (it is possible to notice the similarities between data for this solution and the one for the transfer toward the 4th of

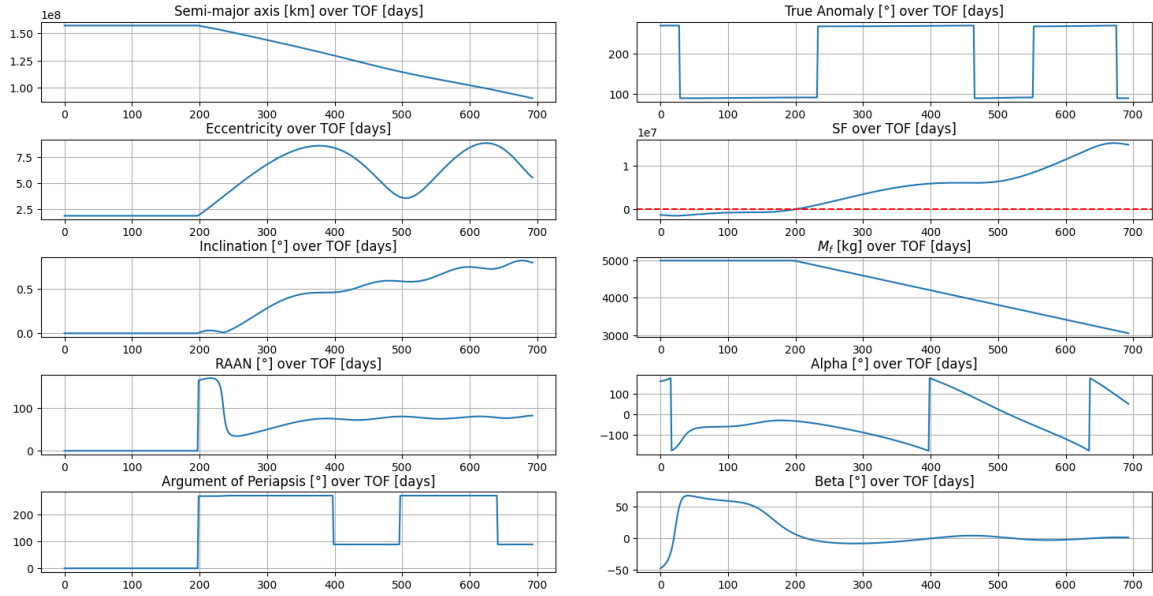


Figure 6.24: Data from the diverging solution for the transfer towards 2013BS45 (attempted rendez-vous on 26th July 2026) at the first use of the pseudo-inverse of the Jacobian matrix

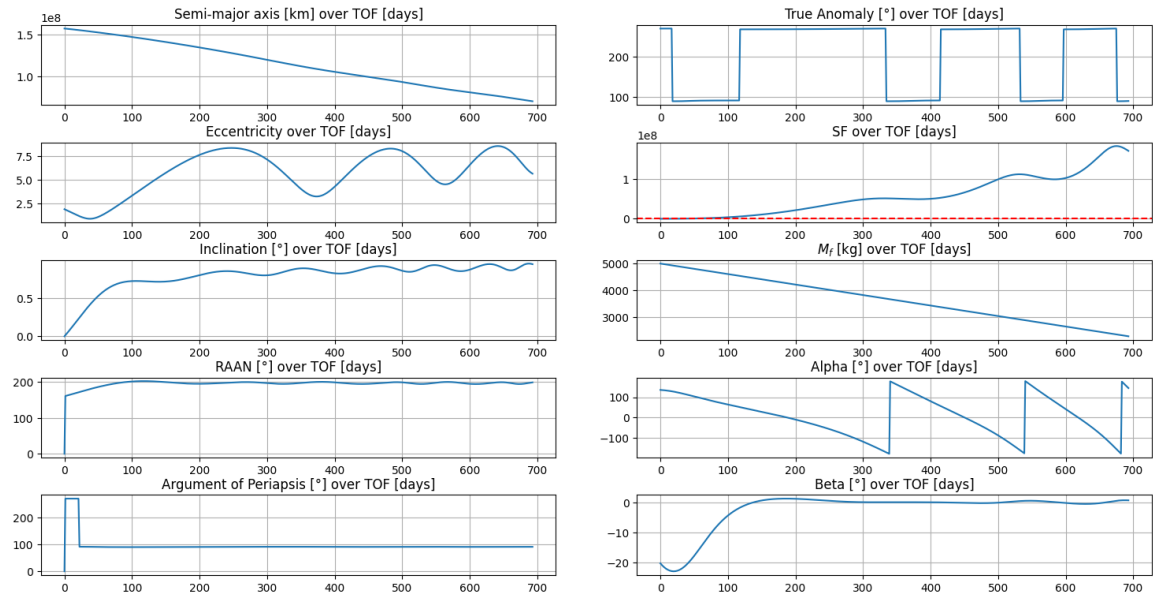


Figure 6.25: Data from the diverging solution for the transfer towards 2013BS45 (attempted rendez-vous on 26th July 2026) at the 5th and last use of the pseudo-inverse of the Jacobian matrix

July 2026 in fig. 6.8), so the optimizer is trying to converge to a solution that belongs to the already discussed primary family of solutions for transfers from Earth to 2013BS45. We can notice from the variations over time of α how the corrections on semi-major axis and eccentricity are continually made and timed to optimize their variations with the thrust arcs established by the shape of the \mathcal{S}_F . This works until the discrepancy drops below 2×10^{-6} when suddenly the quickest maneuver, the one without any revolution around

the Sun that as discussed before is more convenient from an optimization standpoint but is dynamically and therefore practically impossible, happens to be considered as the favorite option by the optimizer. This can only be achieved through an always positive \mathcal{S}_F and so the optimizer gets to very high values of \mathcal{S}_F in order to reach the targeted point directly (as it is possible to see in figs. 6.24 and 6.25). However, the thrust is not sufficient to reach the targeted point with such maneuver (also given the fact that TOF is fixed, so the spacecraft will push for the whole time of the maneuver) that will end after the imposed time (693 days) on a completely different point of the space from the desired one. This brings the terms of the Jacobian matrix to have big numbers at the numerator, with order of magnitude even greater than 10^8 when working with non-dimensional quantities (see (3.13)), while at their denominator δ is always in the order of 10^{-7} so the values in the Jacobian matrix become too big and so its inverse matrix becomes singular with a consequent divergence of the solution. The hypothesis is therefore that when considering transfers that require more than one complete revolution around the Sun and that target a point on the final orbit that is far from the starting point along the z-direction the optimizer tries to converge towards solutions that aim at reaching the targeted point directly without any revolution around the Sun in between. However, this surely brings to divergence because those calculations are operated with fixed TOF and its value is referenced to a transfer that is meant to have multiple revolutions around the Sun, so therefore the resulting wrong switching functions (such as the one in fig. 6.24) will bring to too long thrust arcs that will send the spacecraft far from the desired destination.

6.1.2 Secondary family of solutions for 2013BS45 rendez-vous

The secondary family of solutions was found when trying to find a solution that could converge for a transfer towards 2013BS45 orbit for a rendez-vous on the 25th of December 2026 in $\nu = 278.82^\circ$. The set of costates that constitutes the initial conditions guess that led to convergence is the following

$$\boldsymbol{\lambda}_0 = \{\lambda_x, \lambda_y, \lambda_z, \lambda_{v_x}, \lambda_{v_y}, \lambda_{v_z}, \lambda_m\}_0^T = \{0.19, 0.19, 0.3, 0.34, 0.34, 0.4, 1\}_0^T \quad (6.6)$$

When looking to figs. 6.26, 6.27, 6.31, 6.32, 6.34, 6.35, 6.37, 6.38 it is possible to notice how different this family of transfers is, especially given that the lowest-TOF transfer is the one for the rendez-vous on the 4th of November 2026 (so it requires the thruster to push continuously for 794 days compared with the 441 days of single thrust arc of the quickest maneuver of the primary family), with a consequent greater cost in terms of propellant mass used. They take more time (and at least nearly two complete revolutions around the Sun) and therefore it is necessary to have lower initial guess values for position costates (the ones influencing heavily the \mathcal{S}_F shape) in order to target the same ν value but with a one year longer transfer. The difference between the values for x- and y-components for both position and velocity costates is due to the greater control needed on the thrust, after the previous failed attempts with all the three components being equal, to push more towards the z-axis direction and to allow an easier convergence.

The reason for those great differences in comparison with the primary family of solutions is principally due to the tendency of the optimizer to increment the semi-major axis so that the following plane change has a reduced impact on the final mass of the spacecraft because of its being performed further from the Sun (it is split between the

first and the second leg of the transfer). However moving further from the Sun has a cost that negatively compensates the propellant mass saved performing the plane change further from the Sun, also because the available time to complete the transfer, in both cases, is 794 days and so the initial increment of the semi-major axis (that, how figs. 6.26, 6.27 help to point out, can bring the spacecraft to a distance from the Sun very close to Mars orbit, so it is a very long distance to close up during the "second leg" of the transfer) forces the thruster to push for the whole 794 days to reach the rendez-vous on the 4th of November 2026 as expected. This maneuver leaves the spacecraft with only the 37.90% of the initial mass, so given the fact that the dry mass of the spacecraft is the 40% of its whole initial wet mass we get that this maneuver is impossible to be performed by our spacecraft (so by choosing the maneuver from the primary family it is possible to virtually save nearly 2.5 tonnes of propellant).

A clear difference is noticed if we instead consider the maneuver taken from the first family of solutions targeting the same rendez-vous on the 4th of November 2026. During the same TOF (as shown by figs 6.29 and 6.30) the spacecraft performs three thrust arcs, the first to adjust mainly inclination, the second and the third to change semi-major axis (it is reduced, instead of incrementing it, by less than 10% with massive propellant saving and less time necessary to complete a revolution around the Sun) and eccentricity so the time length of those arcs (117, 24 and 33 days respectively) is 174 days on aggregate with 620 days of no-propellant consuming coasting (the final mass that is equal to the 86.22% as shown in table 6.5 of the initial wet mass) that contribute to increase the amount of mass from the asteroid itself the spacecraft can collect.

	m_f [kg]	final m_p [kg]	thrust days (% over TOF)
Primary family	4311	2311	174 (21.9%)
Secondary family	1895	-105	794 (100.0%)

Tabella 6.5: Comparison between transfers towards $\nu = 229.67^\circ$ (rendez-vous on 4th of November 2026, TOF = 794 days) from Primary and Secondary Family

If we increase the targeted ν and TOF we get that the increment in semi-major axis is less evident and so the duration of the thrust arcs decreases. The \mathcal{S}_F is shaped around a structure with two thrust arcs, one at the beginning of the maneuver to increase the semi-major axis and the other at the end to reduce it with the plane change that is split between the two arcs (figs. 6.33 and 6.36), that gets to turn into a 4-thrust arcs structure for longer maneuvers (see fig. 6.39) with reduced increments in the first stages of the transfer and so therefore a reduced quantity of propellant consumed (the rendez-vous on the 26th of September 2027, shown in figs. 6.37, 6.38 and 6.39, leaves the spacecraft with the 69.82% of the initial wet mass).

These calculations made clear how less convenient the secondary family is in comparison with the first. In facts the excessive increment in semi-major axis brings to a greater propellant consumption without any time advantage. In fact, the primary family allows to reach a rendez-vous with the asteroid using less propellant and less time (see fig. 6.41).

However this family of solutions was useful to better understand how the optimizer works and to see the concept of "family" of solutions in full display and how important the work of the engineer is in critically analyze the results obtained through computation.

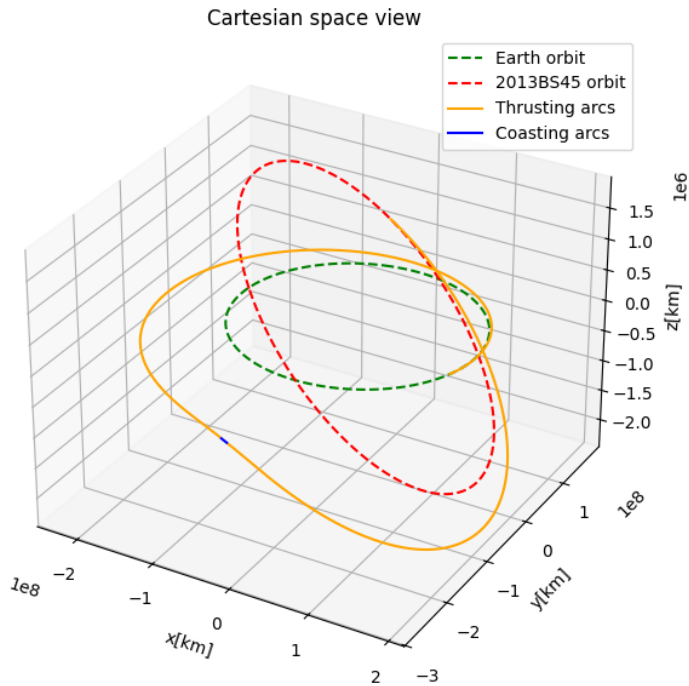


Figura 6.26: 3D optimal transfer towards 2013BS45 with rendez-vous on November 4th, 2026

Looking at solutions from both families it is possible to notice (see fig. 6.41) how the longer is the duration of the transfer the less is the mass of propellant consumed. This is true only if the destinations targeted are on the same orbit. In fact, as shown by (2.11), the mechanical energy is constant along each orbit so the variation of energy given to the spacecraft through the thrust is the same for all the considered maneuvers because they are performed from and to the same couple of orbits. The difference among all the trajectories lies in the different ν targeted and therefore the TOF fixed for the mission. The same Δv has to be generated by the thrusters in a different amount of time available and so we need to accelerate the spacecraft more if it has less time to reach the final orbit (so therefore we will have maneuvers with generally higher \mathcal{S}_F values and longer thrust arcs with higher mass of propellant consumed) and vice versa.

6.1.3 Solutions TOF-free for transfers towards 2013BS45 orbit

In sections 6.1.1 and 6.1.2 solutions for optimal maneuvers aimed at reaching 2013BS45 orbit for a rendez-vous with the asteroid itself (so targeting all the Keplerian orbital parameters and the TOF given the launch of the spacecraft from the L2 point of the Sun-Earth system assumed to be scheduled for the 1st of September 2024). In this section the goal is finding the optimal transfer to reach 2013BS45 orbit targeting only the ν of its point we want to reach. So therefore we want to make calculations that leave TOF

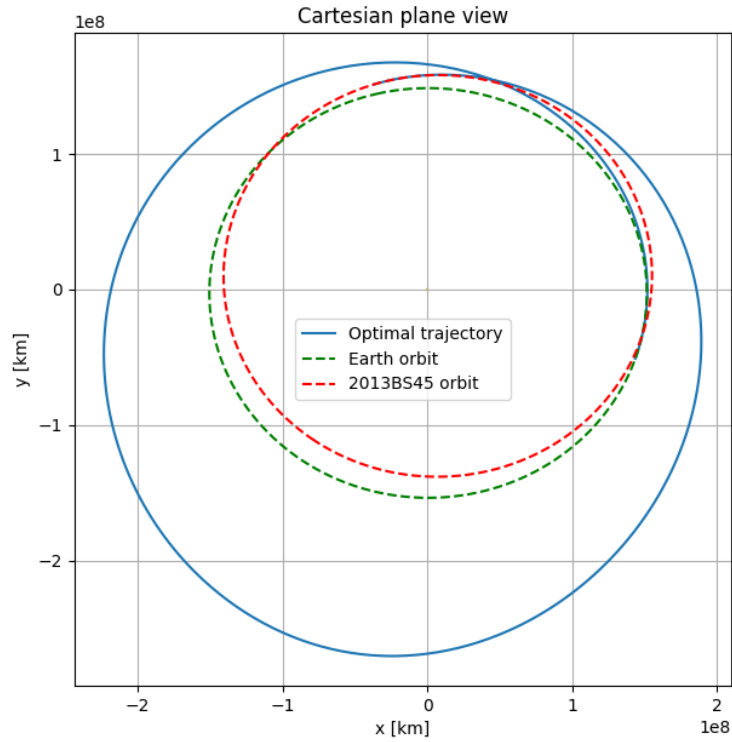


Figura 6.27: 2D optimal transfer towards 2013BS45 with rendez-vous on November 4th, 2026

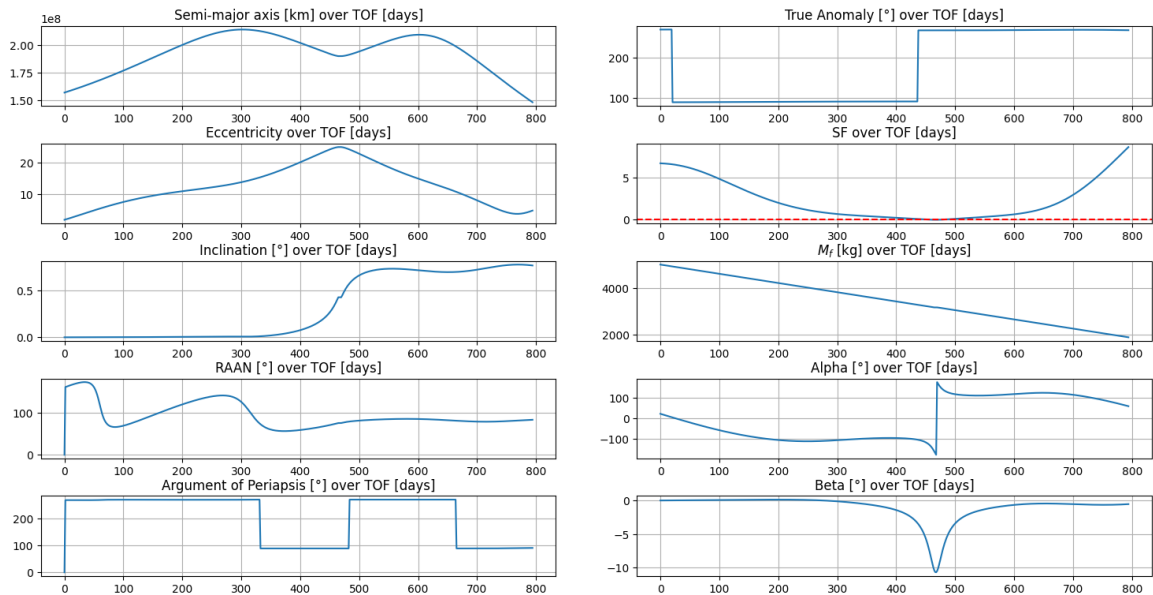


Figura 6.28: Orbital, angular and thrust data from maneuver for rendez-vous with 2013BS45 on November 4th, 2026

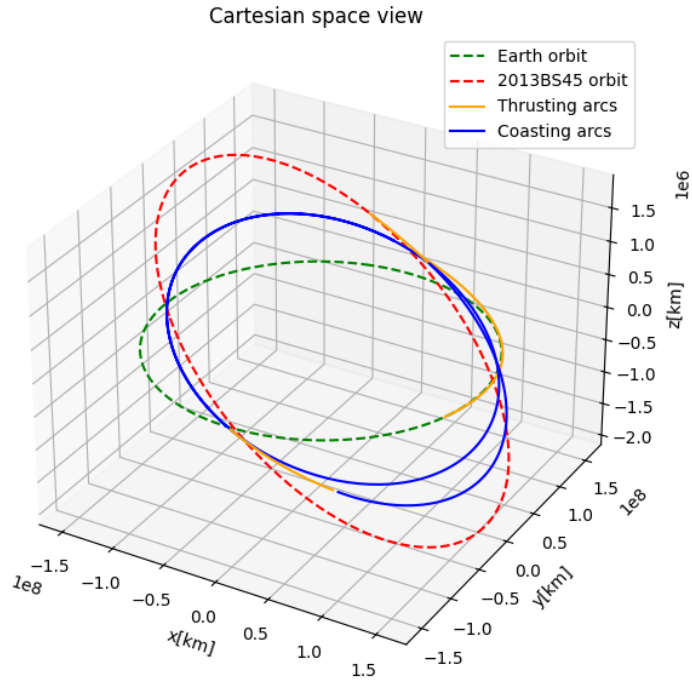


Figura 6.29: 3D optimal transfer towards 2013BS45 with rendez-vous on November 4th, 2026 (from primary family)

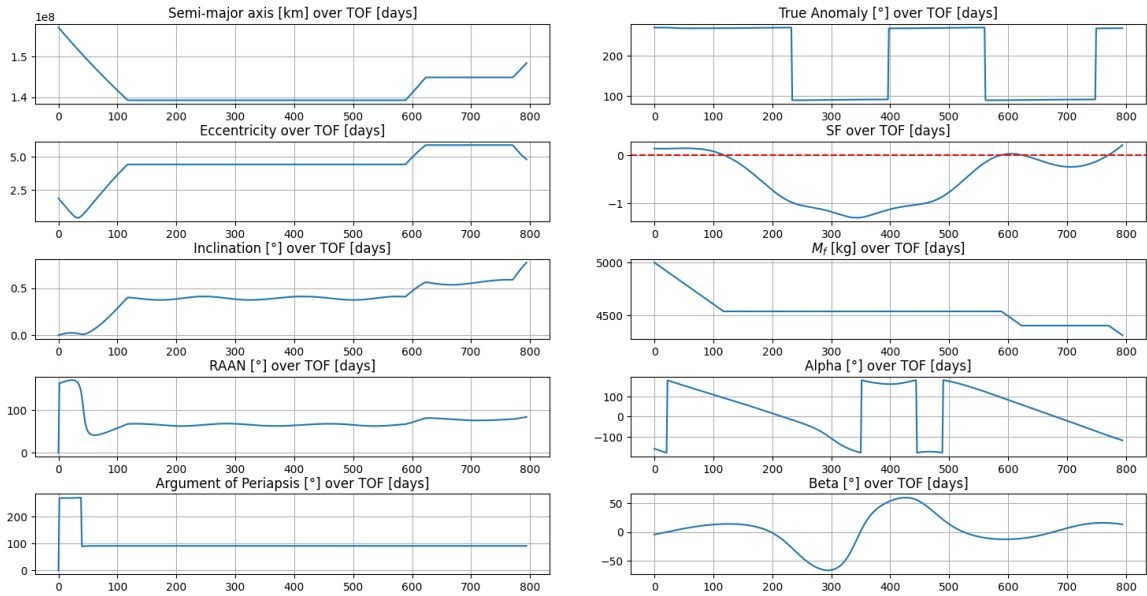


Figura 6.30: Orbital, angular and thrust data from maneuver for rendez-vous with 2013BS45 on November 4th, 2026 (from primary family)

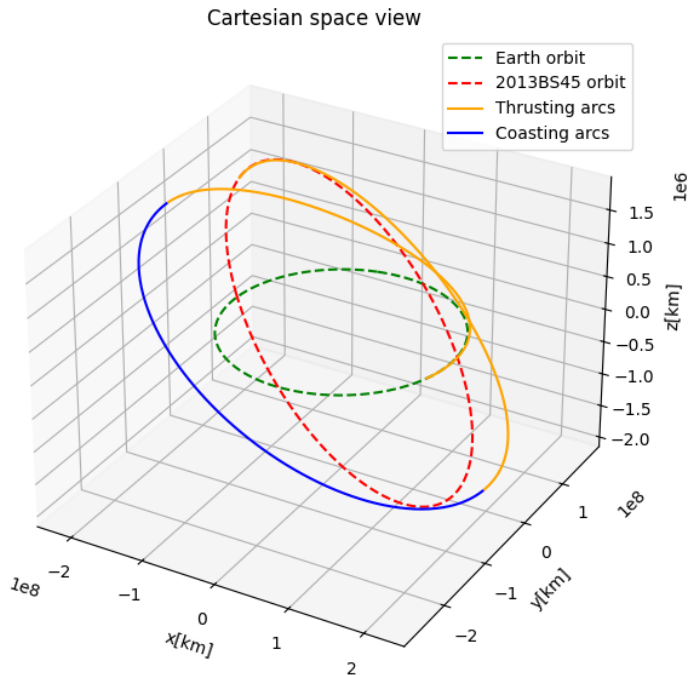


Figura 6.31: 3D optimal transfer towards 2013BS45 with rendez-vous on January 20th, 2027

free and therefore influenced by the ongoing process for the optimization of the mass of propellant used. In other words, the TOF of the following group of solutions is the one that brings the least expense in terms of m_p among all the possible transfer targeting 2013BS45 orbit at that particular value of true anomaly.

The first convergence has been obtained by targeting $\nu = 258.33^\circ$ on the final orbit with a resulting optimal transfer requiring 163 days to be completed and a final wet mass m_f of 4374 kg (the 87.48% of the initial wet mass) and 2374 kg of residual mass of propellant (the 79.13% of the mass of the initial propellant). The set of initial costates used to reach convergence is the following one

$$\boldsymbol{\lambda}_0 = \{\lambda_x, \lambda_y, \lambda_z, \lambda_{v_x}, \lambda_{v_y}, \lambda_{v_z}, \lambda_m\}_0^T = \{0.6, 0.6, 0.6, 0.4, 0.4, 0.4, 1\}_0^T \quad (6.7)$$

where the higher values for position components costates (if compared with the ones in eqs. 6.4, 6.5 and 6.6) indicates how this group of solutions privileges higher values for the \mathcal{S}_F because of the shorter TOF obtained by calculations. As figs. from 6.42 to 6.50 point out, the optimizer prefers to converge towards trajectories that tend to slightly increase the semi-major axis during the initial stages of the transfer to reduce the cost of the plane change maneuver (β is always positive during the whole transfer as in figs. 6.44, 6.47 and 6.50, also because the lowest-TOF possible transfer, with always $\mathcal{S}_F > 0$, is the one targeting $\nu = 256.1^\circ$ that is in the most vertically distant region of the orbit from the

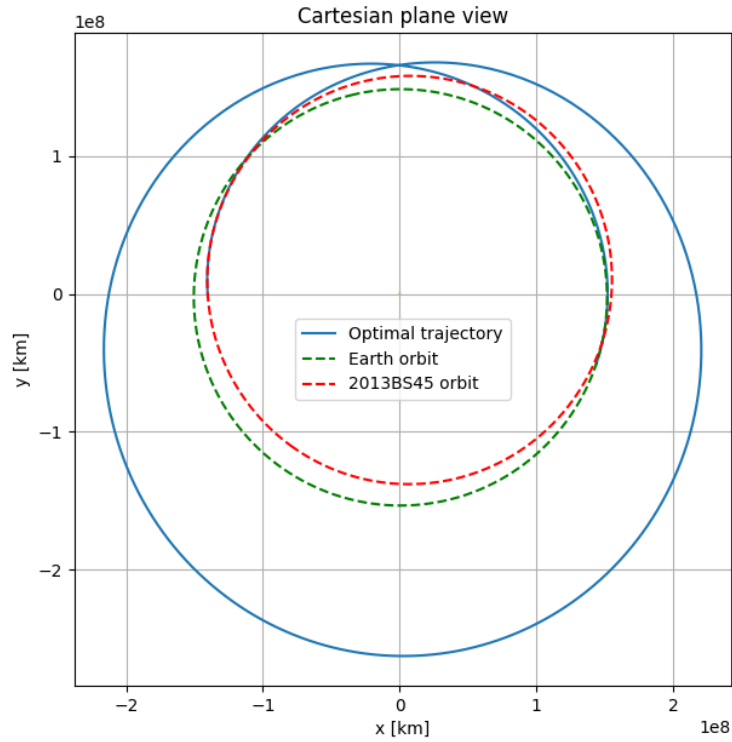


Figura 6.32: 2D optimal transfer towards 2013BS45 with rendez-vous on January 20th, 2027

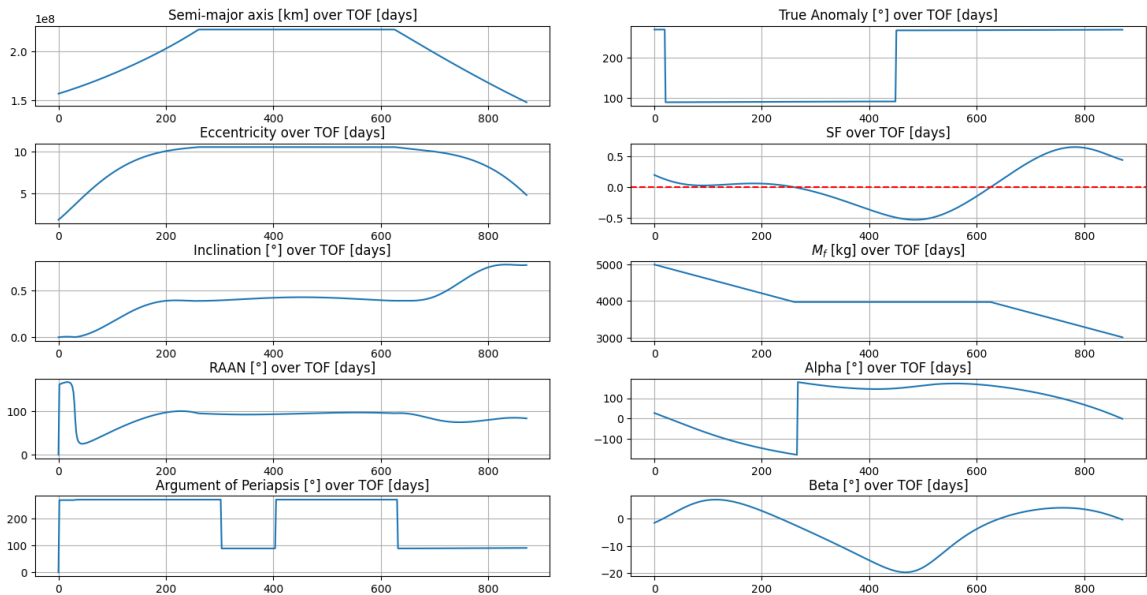


Figura 6.33: Orbital, angular and thrust data from maneuver for rendez-vous with 2013BS45 on January 20th, 2027

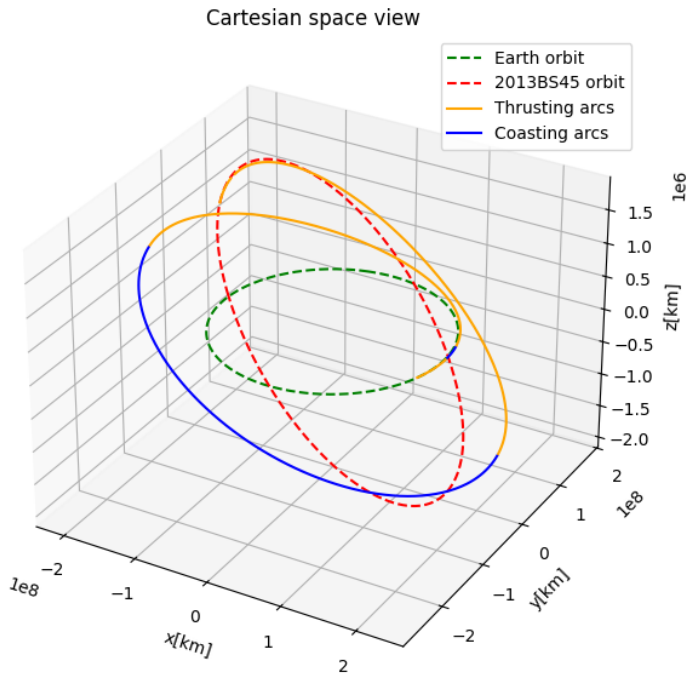


Figura 6.34: 3D optimal transfer towards 2013BS45 with rendez-vous on February 3rd, 2027

ecliptic plane, as shown in 6.42) and then to push towards the center of the orbit (with negative values for α) and towards the opposite verse along the longitudinal direction to decrease the semi-major axis and so to reach the asteroid orbit.

By increasing the targeted ν , as already observed for the solutions discussed in sections 6.1.1 and 6.1.2, a decrease in \mathcal{S}_F values comes as a consequence. However in this particular group of solutions it is possible to notice (see both figs. 6.45 and 6.48) that the 4-arcs structure (even 6-arcs as in fig. 6.48) tends to begin with a coasting arc whose length is greater the further the targeted ν is. This brings the effective launching date to be postponed according with the calculation of the optimizer (the launch now happens at the beginning of the first thrust arc of the mission). However, as already observed for the primary family rendez-vous maneuvers for the 4th of July 2026 and the 16th of August 2026, also in the maneuver targeting $\nu = 185.0^\circ$ it is possible to point out how the point in Earth Orbit where the \mathcal{S}_F begins positive for the first time in the whole transfer gets to be very close in the x, y -plane to the targeted point of the desired final orbit bringing the same feasibility issue for the mission that made impossible to find any convergence in the primary family for $\nu \in [122.82, 170.14]^\circ$.

If compared with the two already discussed families of solutions for rendez-vous maneuvers in terms of final mass of the spacecraft we get that being nearly 1 year shorter in terms of TOF these maneuvers end up being way more preferable because of the huge time and propellant saving advantages (as summed up by fig. 6.52) so that it would be

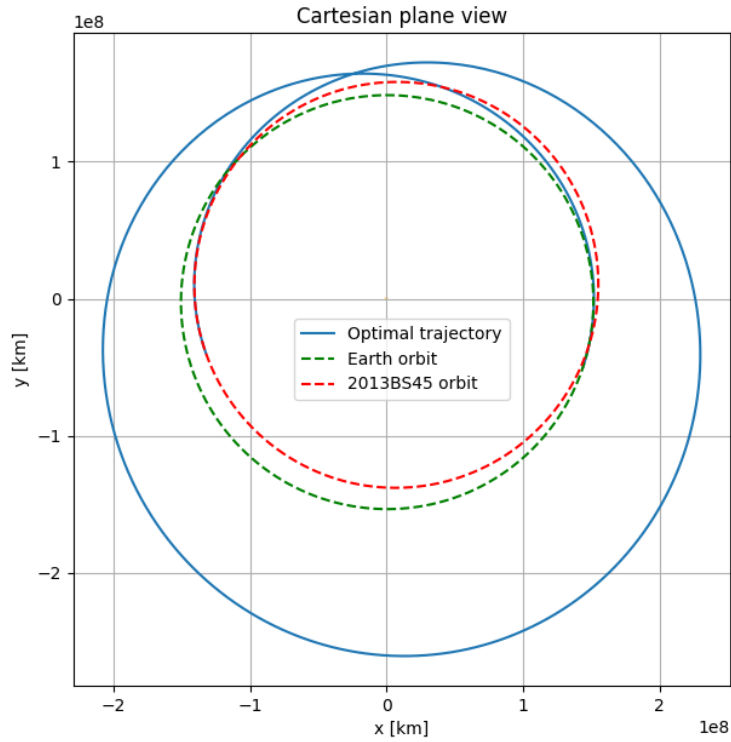


Figura 6.35: 2D optimal transfer towards 2013BS45 with rendez-vous on February 3rd, 2027

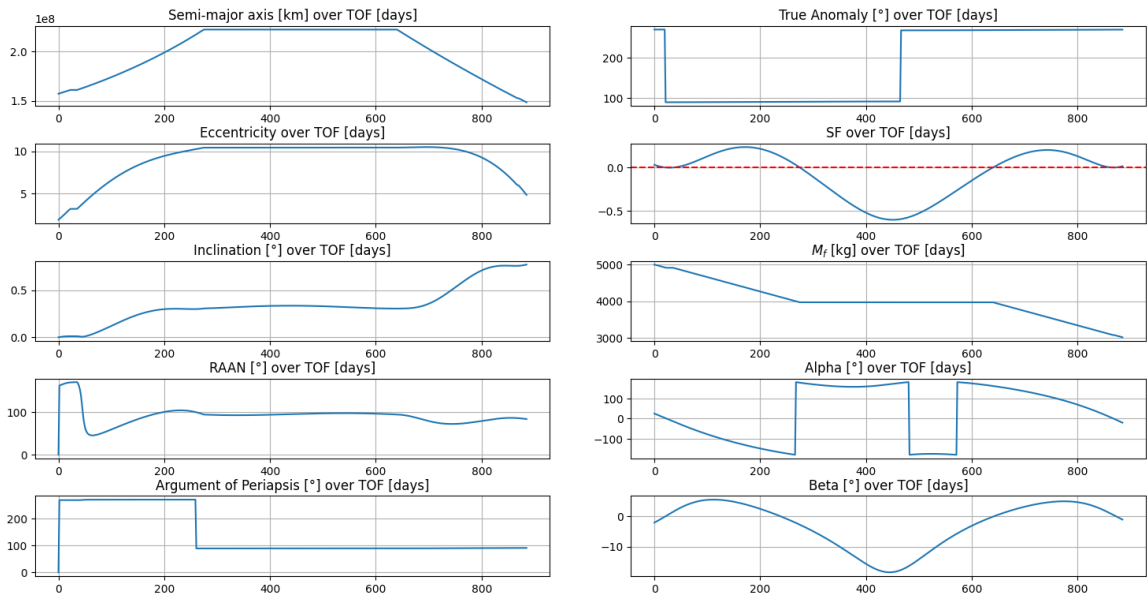


Figura 6.36: Orbital, angular and thrust data from maneuver for rendez-vous with 2013BS45 on February 3rd, 2027

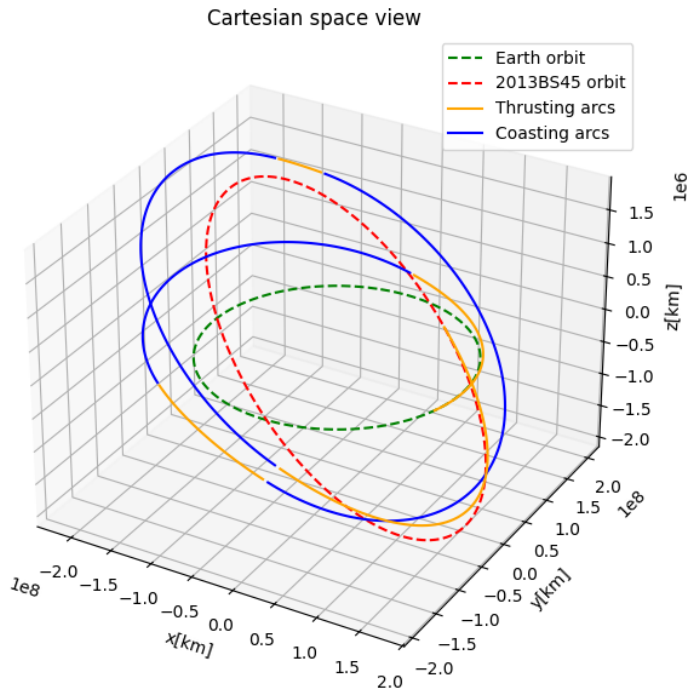


Figura 6.37: 3D optimal transfer towards 2013BS45 with rendez-vous on September 26th, 2027

possible to retrieve, under the hypothesis of a multiple spacecraft mission, more asteroid mass in the least amount of time. However this kind of maneuver is not always possible, in fact its feasibility, as it will be discussed later on, is subjected to previous evaluations about the reciprocal position between the Earth and the asteroid at the moment of the launch in order to be able to turn the TOF-free maneuver calculated in an actual rendez-vous-targeting one.

6.1.4 Optimal adjoint variables values and their dependence with time of flight and true anomaly

In subsections 6.1.1, 6.1.2 and 6.1.3 the results of the search for converging solutions was discussed. In this subsection the goal is to analyze and to compare the obtained results for each family of solutions regarding the set of optimal initial costates that result from the optimal control calculations made.

If we take a look to eqs. 2.49 and 4.54 we get that the costates can deeply influence the behavior of the \mathcal{S}_F and therefore of the distribution of mission-time between thrust and coasting arcs. In fact, as previously said, higher values for λ_x , λ_y and λ_z bring to higher values for λ_{v_x} , λ_{v_y} and λ_{v_z} over time and if the primer vector gets to higher values also the switching function does (being linearly dependent on the primer vector λ_V).

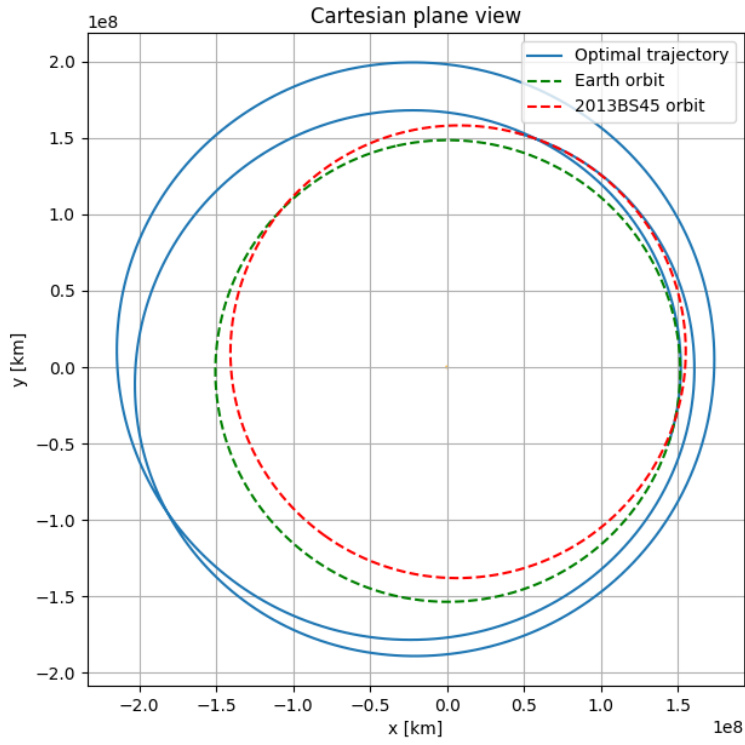


Figura 6.38: 2D optimal transfer towards 2013BS45 with rendez-vous on September 26th, 2027

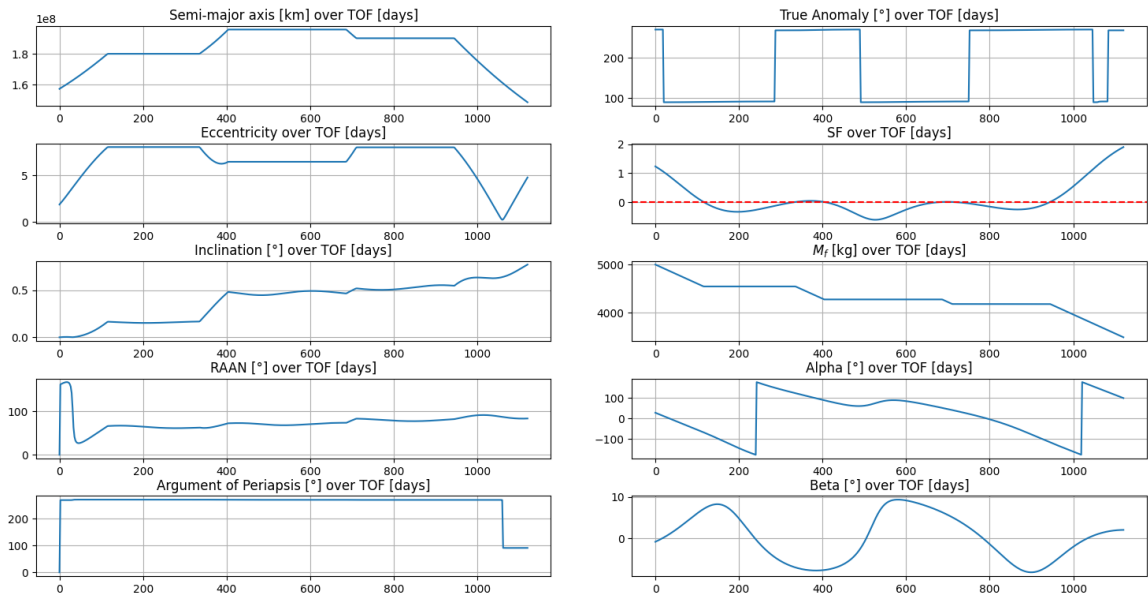
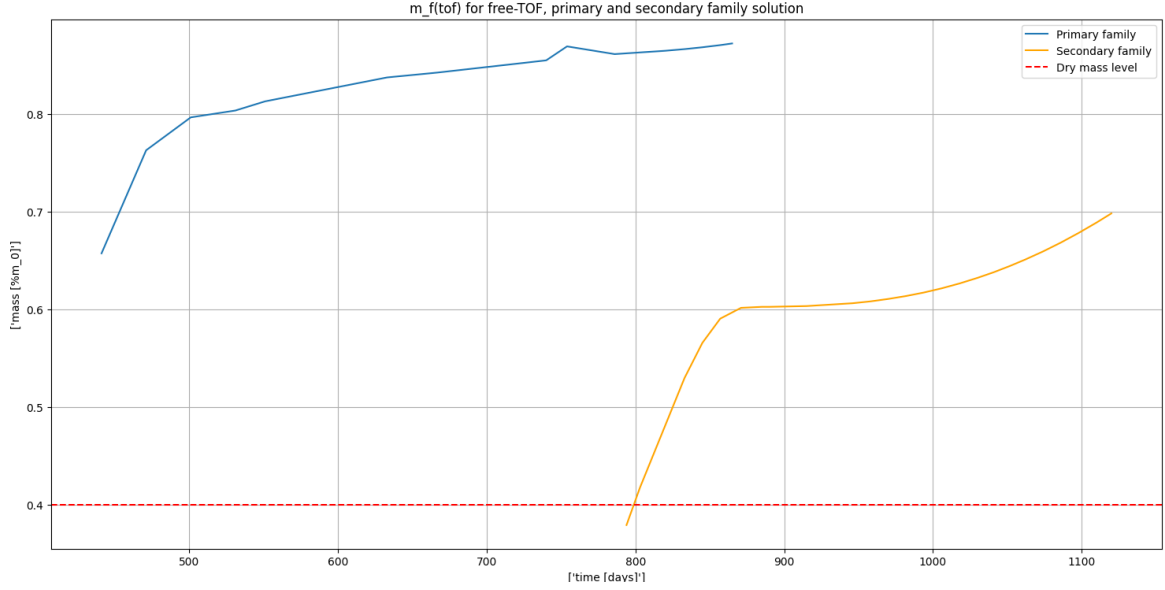


Figura 6.39: Orbital, angular and thrust data from maneuver for rendez-vous with 2013BS45 on September 26th, 2027

ν_f [°]	date of arrival	TOF [d]	m_f (% m_0) [kg]	m_p (% m_{p0})	day with $\mathcal{S}_F > 0$	figure
229.67	4/11/26	794	1895 (37.90%)	-105 (-0.04%)	788 (99.2%)	6.26
306.74	20/1/27	871	3008 (60.15%)	1008 (33.58%)	507 (58.2%)	6.31
322.56	3/2/27	885	3013 (60.25%)	1013 (33.75%)	506 (57.4%)	6.34
199.29	26/9/27	1120	3491 (69.82%)	1491 (49.7%)	385 (34.4%)	6.37

Figura 6.40: Secondary family maneuvers


 Figura 6.41: Comparison between m_f for maneuvers from primary and secondary family

On the other hand also λ_{v_x} , λ_{v_y} and λ_{v_z} have a strong influence over observable quantities such as the thrust angles α and β as shown in eqs. 4.59 and 4.60. In fact, if the velocity components costates have high values the thrust angles will be far from the neutral position so that the resulting direction of the thrust will not be aligned with the velocity vector \vec{V} and will highly probably have a component outside of the plane of the orbit.

Lastly, λ_m plays a role in defining the \mathcal{S}_F (the higher λ_m is, the lower the \mathcal{S}_F) because of its presence in the negative term of the switching function itself. In fact its value influences the tendency of the code to privilege the optimization of the mass over the TOF (the closer it is to 1, the more the mass is optimized) so if the code has to privilege the mass saving over the thrust-time it will end up keeping the \mathcal{S}_F limited to lower values that will make it negative for a greater fraction of the total TOF.

From a general perspective (looking at figs. from 6.53 to 6.58) it is possible to notice that, with the only exceptions of λ_z and λ_{v_z} , all the various λ evolve monotonously and asymptotically towards a certain value the longer the considered transfer is. This is caused by the progressive increasing of the available TOF that allows lower values for α , β and \mathcal{S}_F to be used (in facts the more TOF is available, the shorter the thrust arcs need to be and so the faster the \mathcal{S}_F needs to go back to negative values once it became positive and this is possible only by converging towards a shape for \mathcal{S}_F whose peaks are not so higher above the x-axis). In this context we can interpret the general behavior

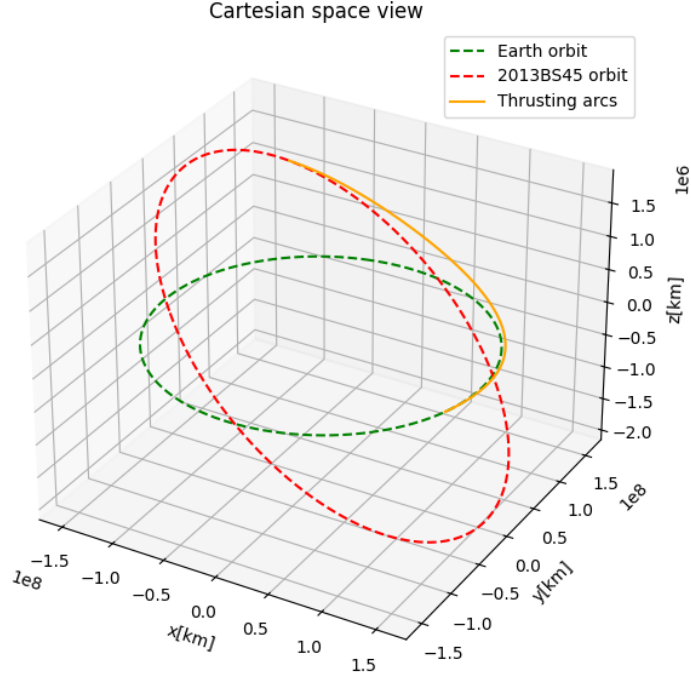


Figura 6.42: 3D optimal transfer towards 2013BS45 at $\nu = 256.1^\circ$

of λ_x and λ_{v_x} among all the analyzed groups of solutions (they tend asymptotically to zero when considering higher TOF transfers) as the reducing need to push with a great lateral component of thrust (as shown in (4.59), if λ_{v_x} tends to zero α tends to zero as well) from the very early stages of the transfer. Also λ_y and λ_{v_y} have a similar behavior tending asymptotically to -1 (of course they cannot tend towards 0 to avoid Inf values for α because of the aforementioned tendency of λ_x and λ_{v_x} to tend to zero).

On the other hand λ_z and λ_{v_z} constitute an exception. In fact the optimizer tends to chose their optimal initial values taking into account its necessity to start pushing towards the positive or the negative direction of the z-axis so, being β determined by (4.60),

$$\beta_T = \arctan \frac{\lambda_{v_z}}{\cos \alpha_T \lambda_{v_y} (1 + \tan^2 \alpha_t)} = \arcsin \frac{\lambda_{v_z}}{\lambda_V}$$

we have that if α gives the thrust a positive component towards the direction of motion of the spacecraft (so $\alpha \in [-90, 90]^\circ$ and $\cos(\alpha) > 0$), with λ_{v_y} being always negative and $\tan^2 \alpha_t$ positive, $\lambda_z > 0$ and $\lambda_{v_z} > 0$ bring to negative values for β with the thrust being pointed from the early stages of the transfer towards the space below the ecliptic plane (and vice versa for negative values of λ_z and λ_{v_z}). The only exception is the secondary family of solutions that tend to postpone the push towards the vertical axis to start with pushing inside the plane of the orbit to change the semi-major axis and the eccentricity instead so having much greater values for position and velocity costates along the x- and y-axis while λ_z and λ_{v_z} are very close to 0 (see fig. 6.59 where it is also possible to notice

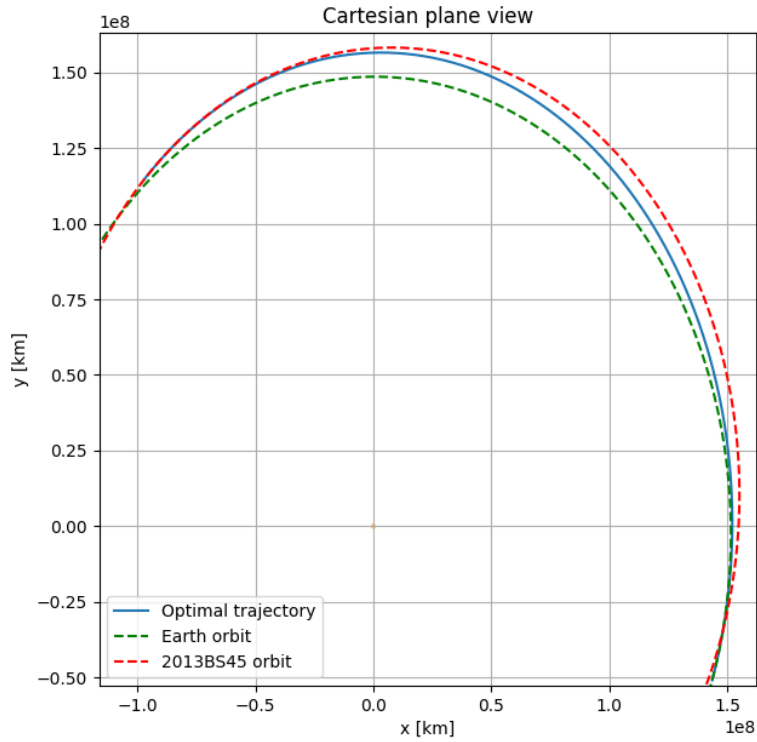


Figure 6.43: 2D optimal transfer (zoom) towards 2013BS45 at $\nu = 256.1^\circ$

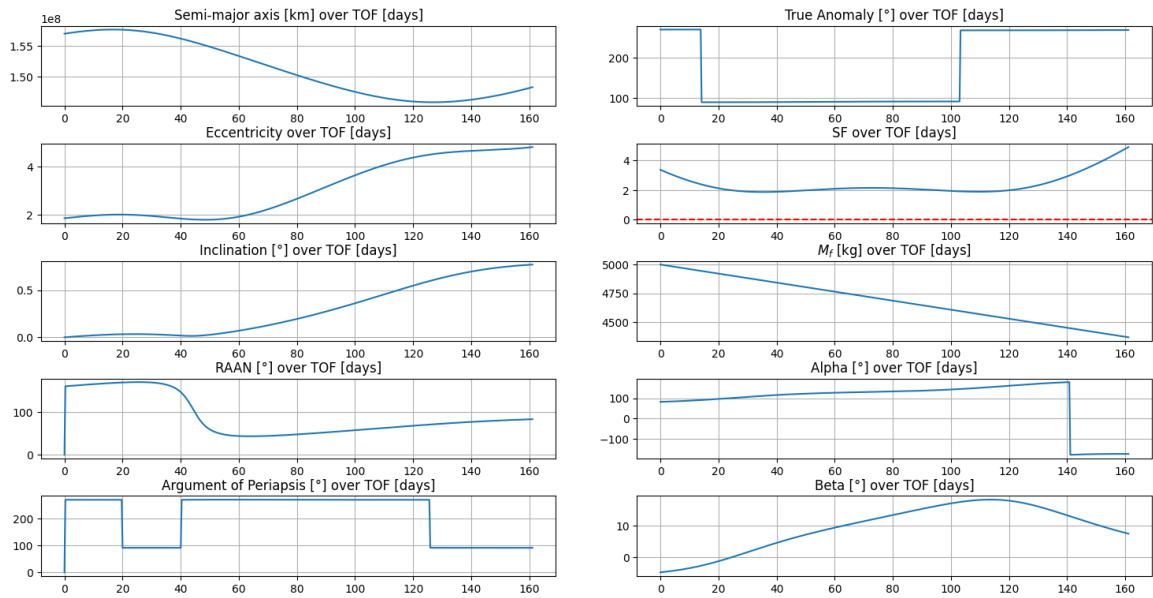


Figure 6.44: Orbital, angular and thrust data from maneuver towards 2013BS45 orbit at $\nu = 256.1^\circ$

that the secondary family solutions have greater differences in terms of optimal initial costates between them than the primary family ones because they are the solutions among

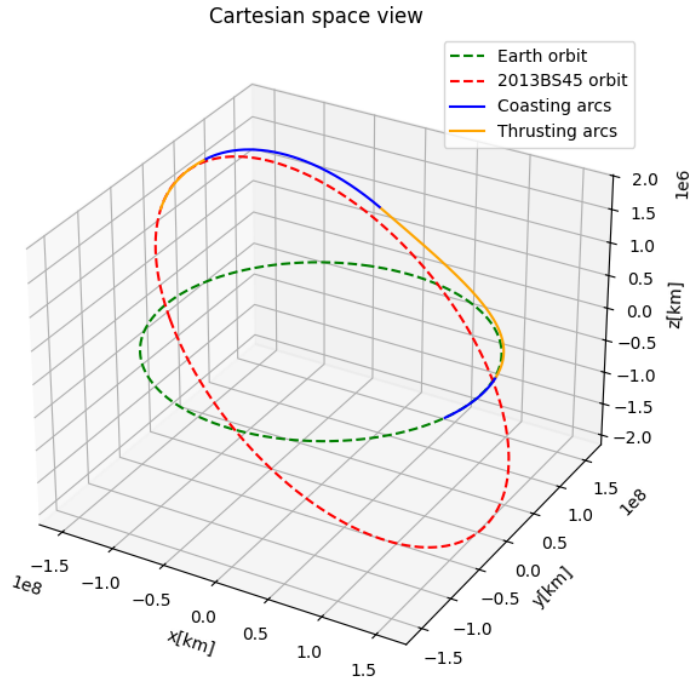


Figura 6.45: 3D optimal transfer towards 2013BS45 at $\nu = 320.3^\circ$

their family with the higher portions of $\mathcal{S}_F > 0$ while solutions with similar TOF values and very long coasting arcs tend to have very small differences between their respective components of the set of optimal initial costates).

The behavior of the optimal initial λ_m follows the principle of optimizing the mass of the spacecraft at the end of every integration step so the longer the transfer is the closer $\lambda_{m_0}^*$ is to 1 because the longer is the transfer the sooner the mass of the spacecraft needs to be optimized. On the other hand, it is possible to notice (see fig. 6.54, 6.56 and 6.58) how for shorter missions where the targeted asteroid has less time to be reached successfully the values for the optimal initial λ_m drops significantly from the benchmark value of 1. The more explicit case of this tendency is represented by the least-TOF transfers among the secondary family of solutions whose values for optimal initial λ_m drop below 0 as a sign of the complete loss of importance in the context of that calculation for the concept of "mass optimization" itself to complete the transfer respecting the time constraint imposed (in fact, as shown in table 6.40, the least-TOF maneuver of the secondary family requires more mass of propellant than the one present on board).

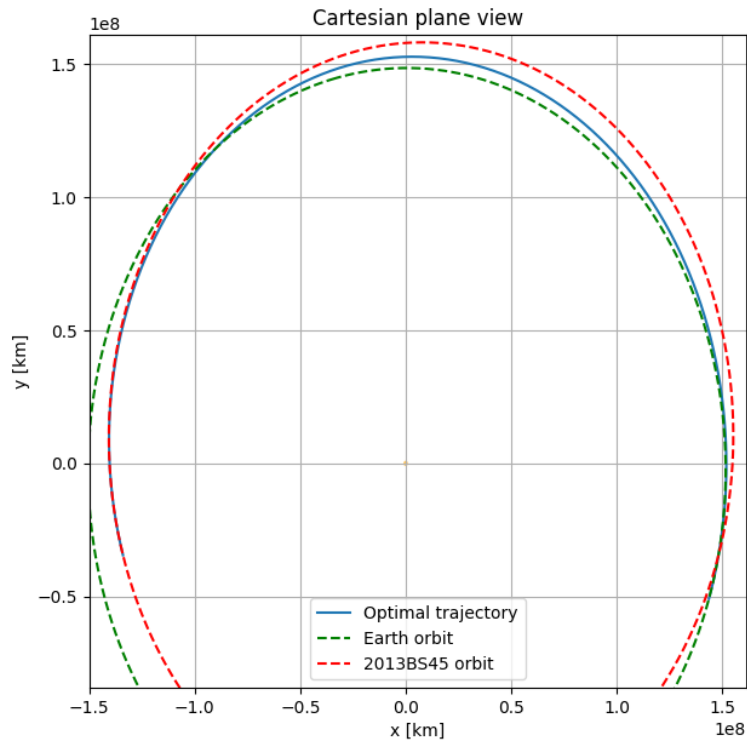


Figure 6.46: 2D optimal transfer (zoom) towards 2013BS45 at $\nu = 320.3^\circ$

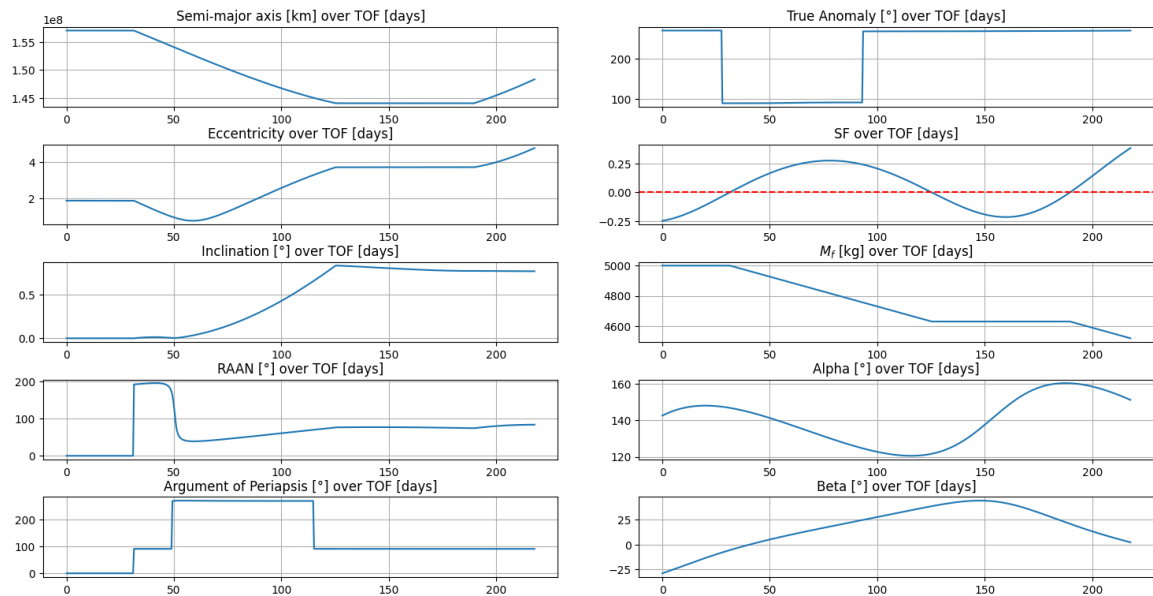


Figure 6.47: Orbital, angular and thrust data from maneuver towards 2013BS45 orbit at $\nu = 320.3^\circ$

6.2 Feasibility conditions for a rendez-vous through a TOF-free maneuver

In subsection 6.1.3 it was demonstrated how it can be preferable to target the orbit of an asteroid following an optimal TOF-free maneuver. However, such transfer is available

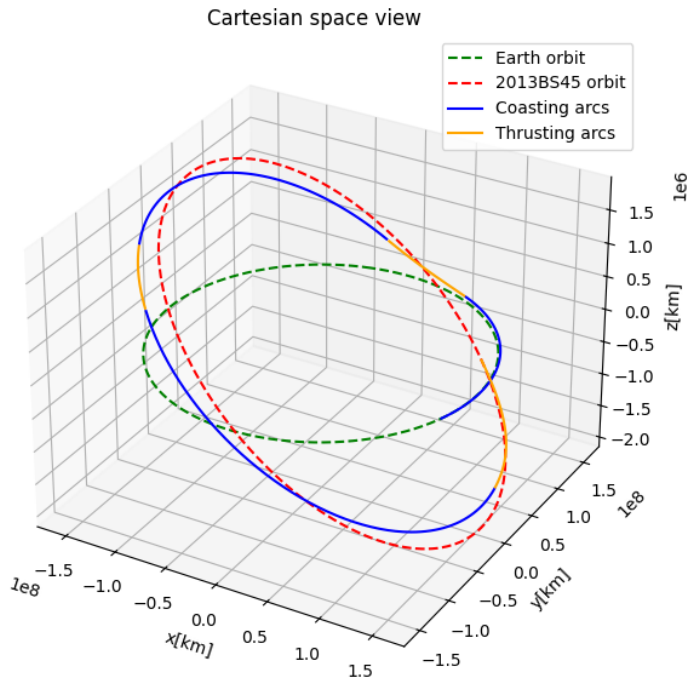


Figura 6.48: 3D optimal transfer towards 2013BS45 at $\nu = 185.0^\circ$

only if the proper alignment between the Earth and the asteroid itself is achieved. In fact, as shown in table 6.6, the orbit of 2013BS45 can be reached from L2 of the Sun-Earth system with a 161 days-long transfer destined to reach $\nu = 256.1^\circ$ on the 9th of February 2025. By the way, the transit of the asteroid via $\nu = 256.1^\circ$ is expected to happen on the 30th of November 2024 so launching on the 1st of September we will not be able to reach the asteroid with that maneuver.

For this reason analyzing when such maneuver can be feasible to actually meet the targeted asteroid for a subsequent rendez-vous can be useful.

With the code written in Python all the quickest TOF-free maneuvers starting on the 1st of September 2024 and targeting some of the selected asteroids have been calculated (the transfer with $\mathcal{S}_F > 0$ throughout the entire transfer so being the least-TOF transfer of each group of solutions targeting every single asteroids). In the table 6.6 values for the targeted ν and the ν of the actual position of the asteroid at the date of the arrival of the spacecraft (and their discrepancy $\Delta\nu$) are collected.

In the same table *negative* $\Delta\nu$ are referred to asteroids that are *behind* the Earth (and therefore *positive* $\Delta\nu$ are referred to asteroids that are *in front* of the Earth) in their revolution around the Sun.

However, given the fact that the closer to the Sun a body is, the higher its angular velocity around the Sun is, we get that a body will reach the optimal ν in only a few years if it is behind the position for the ideal rendez-vous and its semi-major axis is smaller than Earth's one (i) or if it is in front of the ideal rendez-vous ν and its semi-major

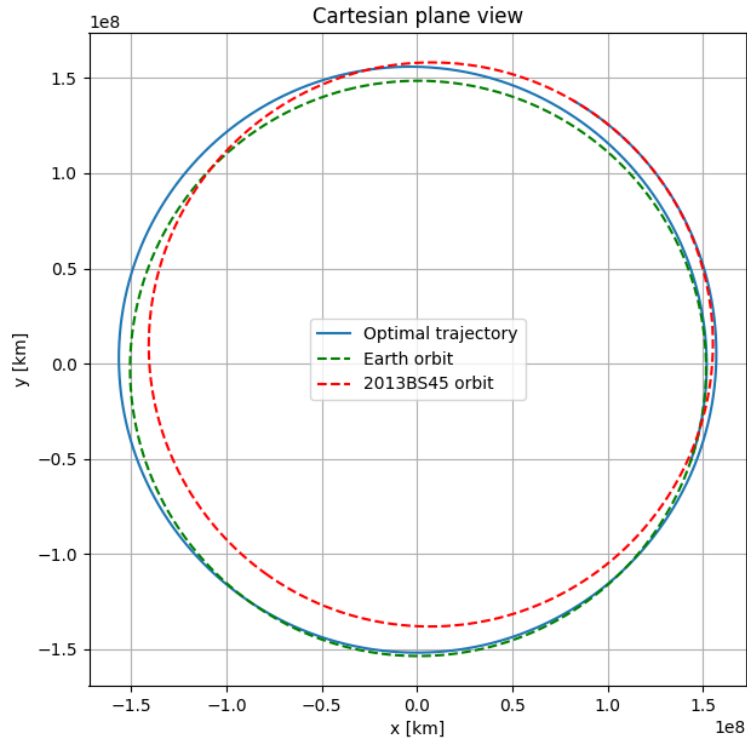


Figura 6.49: 2D optimal transfer (zoom) towards 2013BS45 at $\nu = 185.0^\circ$

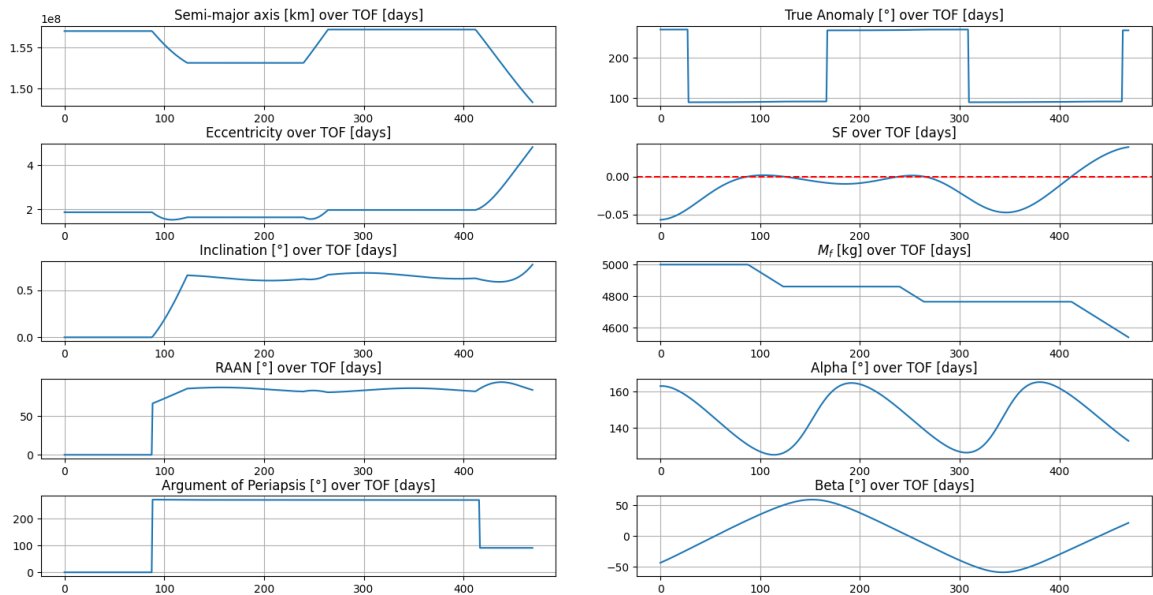


Figura 6.50: Orbital, angular and thrust data from maneuver towards 2013BS45 orbit at $\nu = 185.0^\circ$

axis is greater than Earth's (\circ). In facts, in the first case the inner asteroid will close the gap with the optimal alignment with Earth while in the second case the Earth itself

ν_f [°]	arrival	TOF [d]	m_f (% m_0) [kg]	m_p (% m_{p0})	day with $\mathcal{S}_F > 0$	figure
256.1	9/2/25	161	4366 (87.32%)	2366 (78.87%)	161 (100.0%)	6.42
320.3	27/4/25	218	4520 (90.39%)	2520 (83.98%)	123 (56.2%)	6.45
185.0	14/12/25	469	4540 (90.80%)	2540 (84.67%)	116 (24.8%)	6.48

Figure 6.51: Optimal maneuvers towards 2013BS45 obtained leaving TOF free

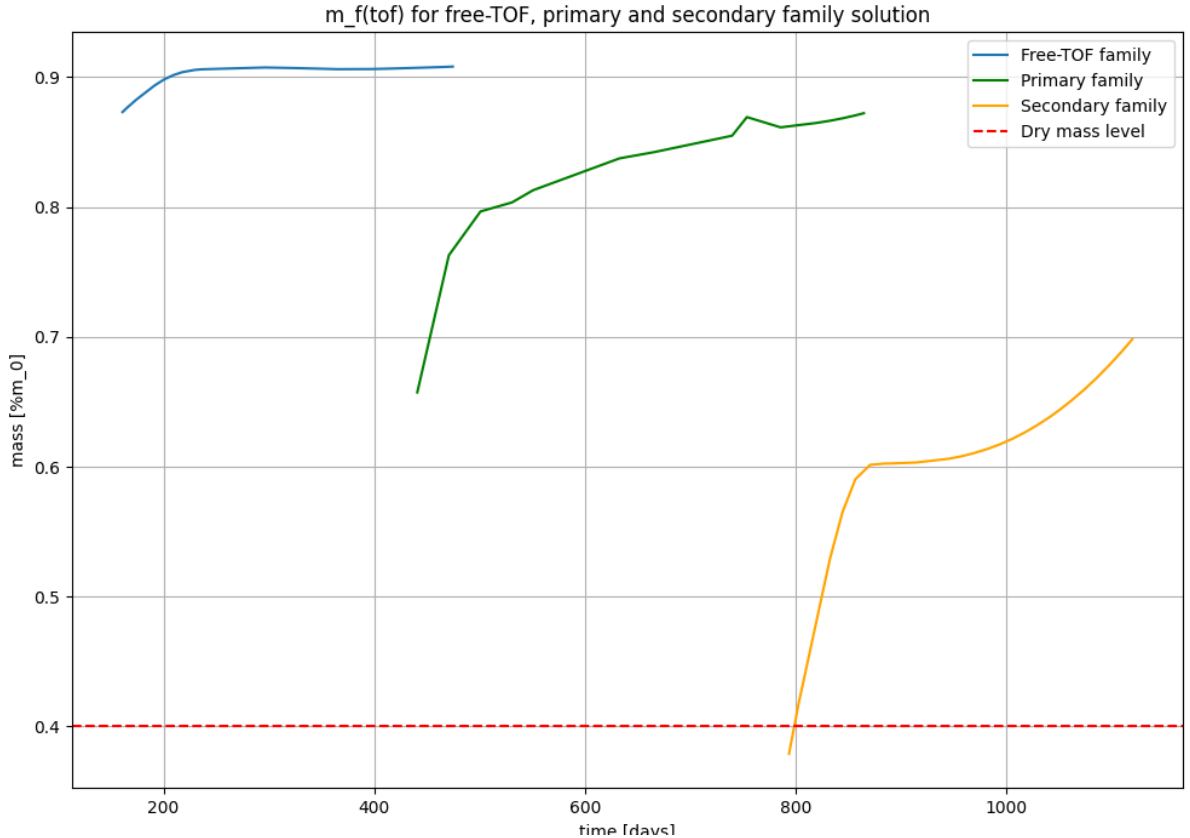


Figure 6.52: Final mass comparison between TOF-free, primary family and secondary family of solutions

will close that gap. Otherwise, it will be possible to launch anyway towards an asteroid if the proper alignment with the Earth with the only condition to be forced to choose a slightly longer maneuver than the least-tTOF one (even if it will be better in terms of m_f) with this being possible only if asteroids with $a_{ast} < a_{Earth}$ are still behind the necessary starting position (the ideal ν_{ast} at the day of the launch) to be reached with the least-TOF maneuver. On the other hand, if a inner asteroid is already in front of the desired position or an outer one is already behind the optimal ν for the direct rendez-vous it will be impossible to reach it with a time-wise suboptimal maneuver (a higher TOF one) because in space its is necessary a longer thrust time to enter an orbit at a closer ν to the starting point so it would not be sufficient pushing for the 100% of the TOF of the transfer to reach the asteroid (the more demanding low-TOF maneuver is the one towards a closer destination). As a consequence, in such cases it will be necessary to rely on a longer maneuver that requires one or more complete revolutions around the Sun in

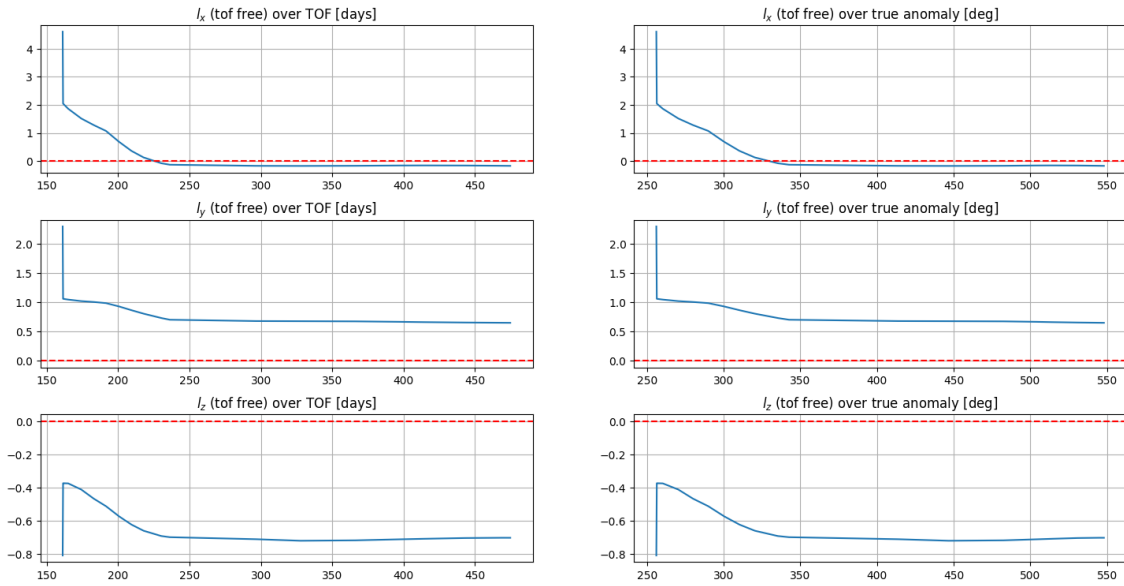


Figure 6.53: Variations of λ_x , λ_y and λ_z over TOF and ν of the mission for free-TOF optimal maneuver for 2013BS45

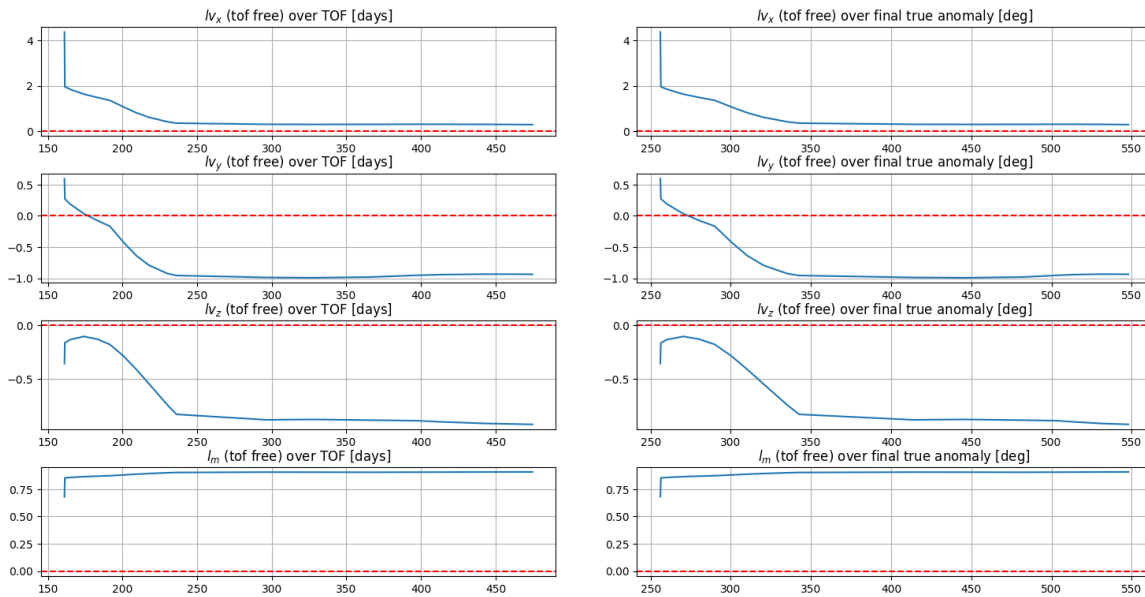


Figure 6.54: Variations of λ_{v_x} , λ_{v_y} , λ_{v_z} and λ_m over TOF and ν of the mission for free-TOF optimal maneuver for 2013BS45

order to reach and rendez-vous it as in the case of 2013BS45 (an inner asteroid in relation with Earth that, considered the date of the launch being Semptembre the 1st 2024, is in front of the ideal ν so it cannot be reached with the optimal-time maneuver) that have been already discussed in subsections 6.1.1 and 6.1.2.

So it is possible to estimate how much time it is necessary to wait for the optimal-TOF transfer to be available and the results of those calculations, knowing the difference in angular velocity, Δn , between the Earth ($n = 1.139448918E-05$ °/s) and every considered asteroid, and the phasing error $\Delta\nu$ we want to be nullified, according with the equation

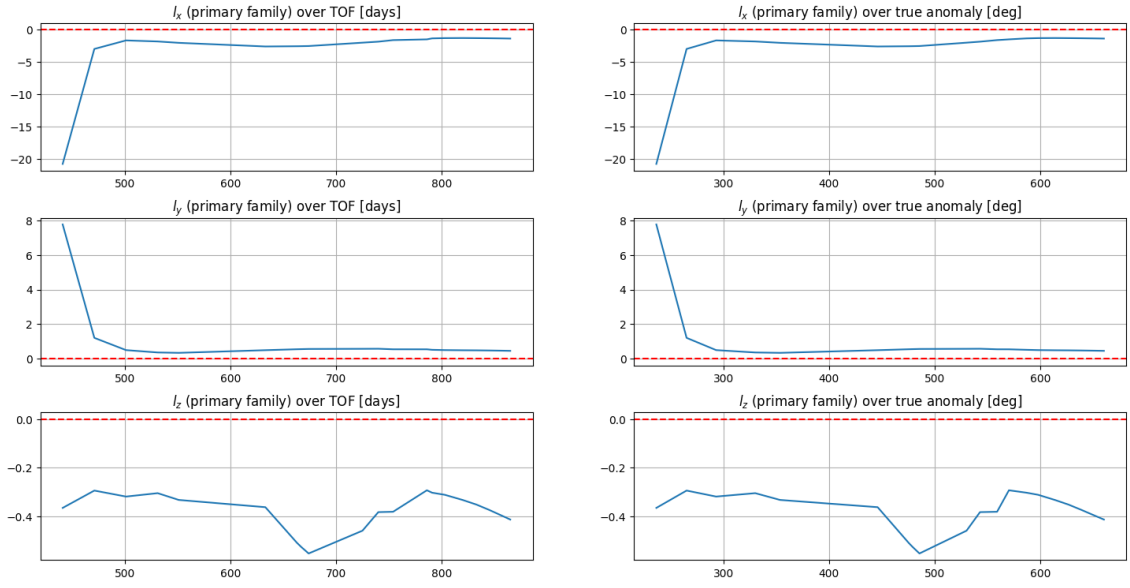


Figure 6.55: Variations of λ_x , λ_y and λ_z over TOF and ν of the mission for primary family of rendez-vous solutions for 2013BS45

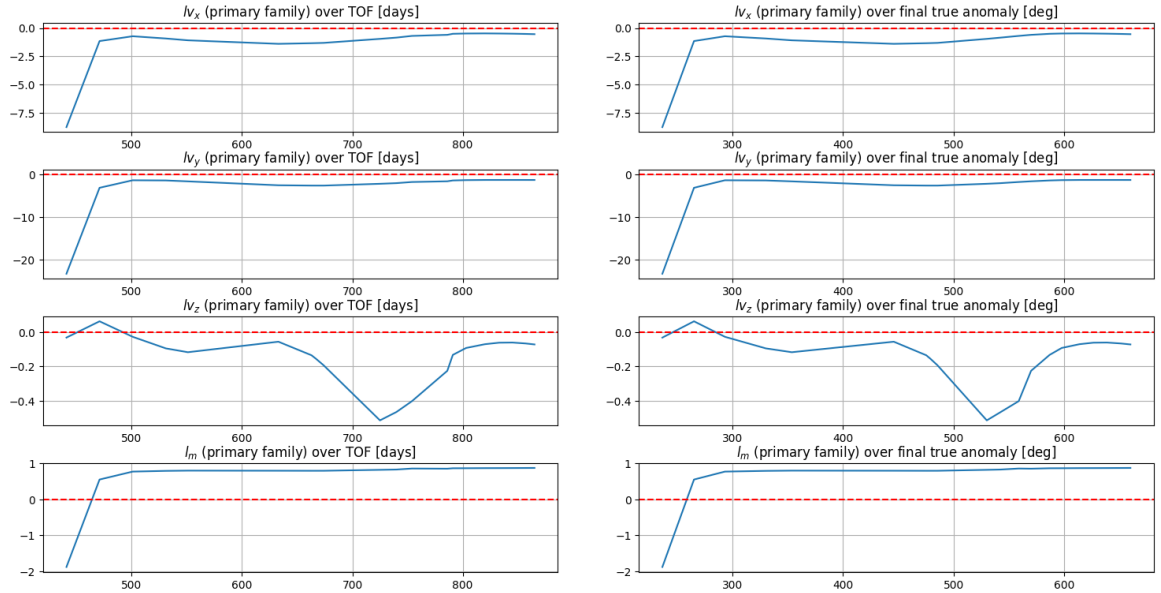


Figure 6.56: Variations of λ_{v_x} , λ_{v_y} , λ_{v_z} and λ_m over TOF and ν of the mission for primary family of rendez-vous solutions for 2013BS45

$$\Delta t_{\text{phasing}} = \frac{\Delta \nu_{\text{to optimality}}}{\Delta n} \quad (6.8)$$

are collected in the table 6.7. The results listed there show how in the near future ($\Delta t < 5$ years from now) 2000SG344 is the only asteroid, among the few here analyzed) that can be reached through a least-TOF-free maneuver (like the ones discussed in subsection 6.1.3) for a rendez-vous launching from L2 of the Sun-Earth system on the 1st of September 2024. For all the other asteroids the more time-consuming one-revolution maneuver (as the ones

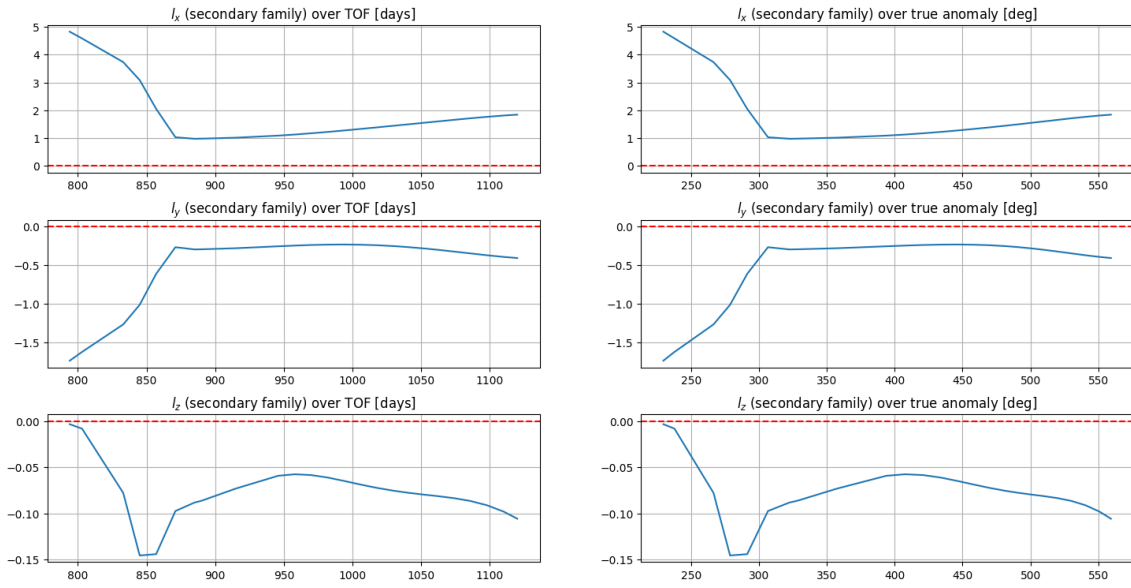


Figure 6.57: Variations of λ_x , λ_y and λ_z over TOF and ν of the mission for secondary family of rendez-vous solution for 2013BS45

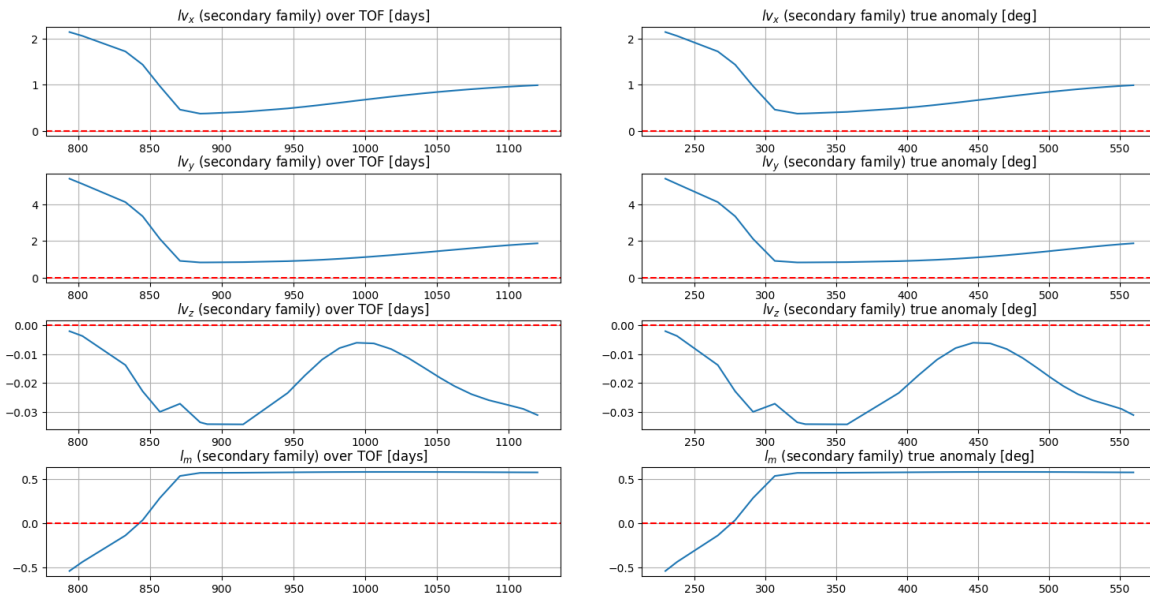


Figure 6.58: Variations of λ_{v_x} , λ_{v_y} , λ_{v_z} and λ_m over TOF and ν of the mission for secondary family of rendez-vous solutions for 2013BS45

discussed in 6.1.1) should be taken into account if the designer of a potential mission does not find preferable to wait until the least-TOF-free maneuver becomes available once again.

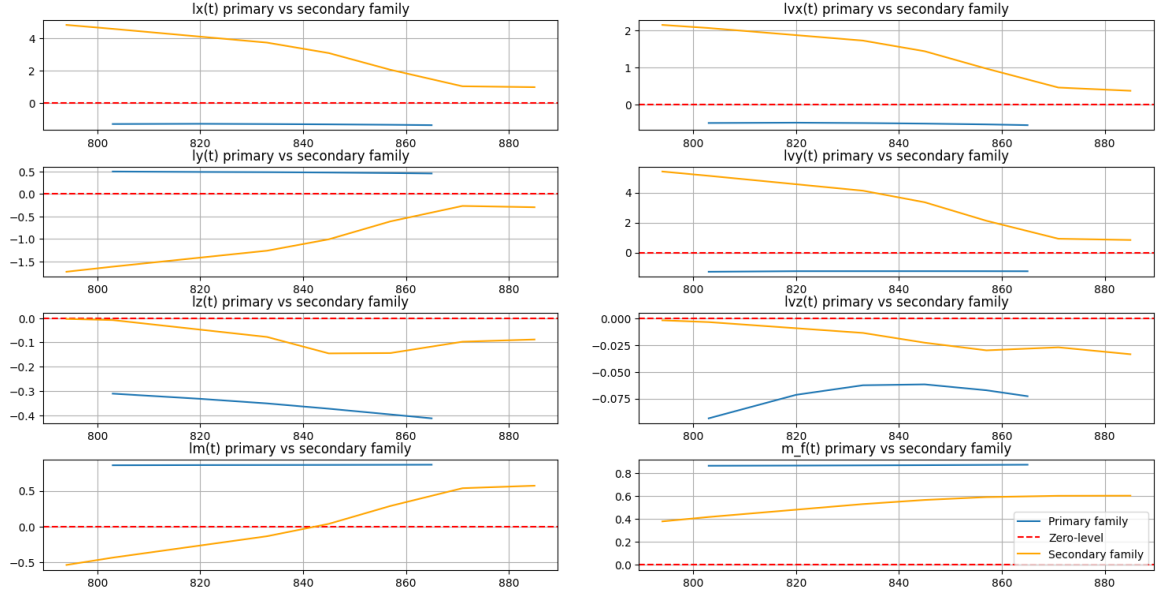


Figure 6.59: Comparison over variations of adjoint variables λ and final mass m_f between the primary family (blue) and the secondary family (orange) of solutions

	Opt rv	rv ν_{ast}	cart rv ν_{ast}	act ν_{ast}	actl cart ν_{ast}	$\Delta\nu$ from rv
2013BS45 (i)	9/2/25	256.1°	119.84°	319.38°	183.12°	63.28°
2000SG344 (i)	29/5/25	136.57°	243.72°	103.70°	210.97°	-32.75°
2021LD6 (i)	28/4/25	172.75°	202.11°	212.21°	241.57°	39.46°
2020CD3 (o)	15/2/25	299.52°	72.77°	6.75°	139.00°	-66.23°
2022NX1 (o)	18/3/25	84.00°	169.72°	62.10°	147.82°	-21.90°
2021GM1 (i)	18/4/25	158.00°	220.39°	210.32°	272.71°	52.32°
2006JY26 (o)	25/1/25	159.00°	116.11°	87.17°	44.28°	-71.83°
2023RX1 (i)	29/3/25	333.00°	180.38°	357.61°	204.99°	24.61°
2010VQ98 (o)	7/3/25	129.00°	156.88°	319.38°	347.26°	190.38°

Tabella 6.6: $\Delta\nu$ between asteroids and their ideal position to be reached in a rendez-vous after the quickest TOF-free optimal transfer from Earth

6.3 Retrieval maneuver

As the last phase of the mission, in this thesis some calculations about the retrieval maneuver have been done. The goal of those calculations was to estimate the amount of asteroid mass that the spacecraft is able to collect from the asteroid itself after having performed the first leg of the mission (the results are shown in section 6.1) to bring it back to the Earth orbit and the total TOF of the mission until it reaches Earth.

After the first leg maneuver the spacecraft has successfully landed on the asteroid and is orbiting the Sun on it while it is collecting material from it, so in simulating the whole mission the material collection time has been arbitrarily assumed in 5 months. Secondly, the first-leg maneuver had to be chosen from the pool of successfully convergent solution previously got. The maneuver with rendez-vous (the analysis of the rendez-vous was outside the goals of this thesis) with 2013BS45 on the 4th July 2026 was chosen because

	$\Delta\nu$ from opt rv	$\Delta\nu$ to next opt rv	Δn with Earth [$^{\circ}/s$]	Δt to rv [y]
2013BS45 (i)	63.28 $^{\circ}$	296.72 $^{\circ}$	1.155408457E-05	58.95
2000SG344 (i)	-32.75 $^{\circ}$	32.75 $^{\circ}$	1.180619182E-05	2.52
2021LD6 (i)	39.46 $^{\circ}$	320.54 $^{\circ}$	1.161065459E-05	47.02
2020CD3 (o)	-66.23 $^{\circ}$	293.77 $^{\circ}$	1.092753566E-05	19.95
2022NX1 (o)	-21.90 $^{\circ}$	339.10 $^{\circ}$	1.101447075E-05	28.30
2021GM1 (i)	52.32 $^{\circ}$	307.68 $^{\circ}$	1.179405481E-05	24.42
2006JY26 (o)	-71.83 $^{\circ}$	288.17 $^{\circ}$	1.123419235E-05	57.00
2023RX1 (i)	24.61 $^{\circ}$	333.39 $^{\circ}$	1.151611337E-05	86.92
2010VQ98 (o)	190.38 $^{\circ}$	190.38 $^{\circ}$	1.102461193E-05	16.32

Tabella 6.7: Time to the next availability for the least-TOF free-TOF maneuver

of its balance between TOF and mass consumption, assuming the goal of the mission being to retrieve the most possible mass from the asteroid in the least possible time. So table 6.8 summes up the characteristics of the chosen mission up to the beginning of the retrieval maneuver.

departure	arrival	TOF [days]	m_f (%) [kg]	m_p left (%) [kg]
1/9/24	4/7/26	671	4216 (84.32%)	2216 (73.86%)

Tabella 6.8: Mass data about the spacecraft after the rendez-vous with the asteroid

In order to help the code to converge for those maneuvers where the total initial mass of the complex spacecraft-retrieved mass (with the mass taken from the asteroid that now acts as the payload of the spacecraft) gets much greater values than the initial wet mass of the spacecraft a nondimensionalizing value of 22000 kg has been used.

6.3.1 Transfer towards the waiting orbit

Having fixed the time for collection of asteroid mass in 6 moths it is possible to assume the date of lift-off from the asteroid to begin the second leg of the journey to be on January the 4th, 2027. Using the python code for optimal transfers calculations iterative computations through a process of try-and error were made to find solutions that enable the spacecraft to move from the orbit of 2013BS45 (whose ν is 289.32 $^{\circ}$ as shown by NASA Ephemeris [37]) to an intermediate parking orbit where it has to wait until a second spacecraft, with same initial characteristics of the first one (see table 6.1), will perform a rendez-vous with the first spacecraft to bring it at the orbit of the Earth as in the mission structure suggested by [23] where the final retrieved mass is maximized through the use of two spacecrafts (a *pitcher* that deflects the entire asteroid from its initial orbit to send it towards the orbit of the Earth where the *catcher* intercepts it and slows it down to bring it into an Earth orbit) even though there is suggested the use of impulsive maneuvers to deflect the whole asteroid. In this case, electrical propulsion is considered and given the very low accelerations provided (from data in table 6.1 it is possible to establish the average initial acceleration provided by the thrusters to be 1.75 μN) it is considered $T=T_{max}$ for the whole TOF of the maneuver. The waiting orbit has to have $a_{wo} > a_{Earth}$ because the goal of reaching an outer orbit is to close the gap with the needed alignment

with the Earth to return to Earth with a least-TOF-free maneuver (the kind of transfer analyzed in subsection 6.1.3).

The problem can therefore be defined as a matter of balancing the amount of retrieved mass with the distance between the chosen waiting orbit and the orbit of 2013BS45 and with how far is the point of the waiting orbit where the spacecraft manages to enter it (that is the point where the second spacecraft will have a rendez-vous with the first one to push it back to Earth). In fact, the heavier the retrieved mass is, the further the enter point in the waiting orbit is and this makes longer the time the spacecraft needs to spend on it to reach the optimal alignment (the Earth is now on a closer orbit to the Sun so the spacecraft needs to stay slightly in front of the Earth to be able to reach it with a direct maneuver).

As a result of this iterative process the following maneuver has been found: a 427-days transfer (arrival on March the 6th, 2028, JD = 2461836) towards the orbit (final $\nu = 350^\circ$) described by table 6.9 to bring 15000 kg of retrieved material. The final state of the spacecraft is described in table 6.10, where about 500 kg of propellant were left to face potential corrections during the mission, while the whole maneuver is depicted in fig. 6.60.

semi-major axis [AU]	eccentricity	inclination	RAAN	Arg of perihelion	final ν
1.04	0.017	0.77°	83.4°	150.74°	350°

Tabella 6.9: Keplerian parameters of the waiting orbit

departure	arrival	TOF [days]	m_f ($\%m_0$) [kg]	m_{pf} ($\%m_{p0}$) [kg]
4/1/27	6/3/28	427	2537.15 (50.74%)	537.15 (17.91%)

Tabella 6.10: Mass data about the spacecraft after reaching the waiting orbit (retrieved asteroid mass = 15000 kg)

It would be possible to target further values of ν on the waiting orbit to be able to increase the amount of the retrieved asteroid mass, however this would come with an increased TOF that would translate into a higher time spent on the waiting orbit so therefore delaying the moment of the final return to Earth orbit. The potential convenience of this choice should be evaluated from an economical perspective in terms of Return On Investments (ROI) but this is beyond the intent of this thesis.

6.3.2 Transfer towards Earth orbit

The final goal of this thesis is to find a maneuver the spacecraft can perform to bring the asteroid back to Earth orbit and therefore to estimate the *waiting time* of the complex spacecraft-asteroid, or in other words the time the spacecraft carrying the retrieved mass from the asteroid 2013BS45 has to spend on its waiting orbit (described in subsection 6.3.1) to reach the necessary position in relation with the Earth to be able to perform the desired maneuver.

Considering the mission structure proposed by [23] (with the only difference in the use of electrical propulsion for continuous-thrust maneuvers instead of the impulsive one) we assume that a second spacecraft with the same characteristics of the one that performed

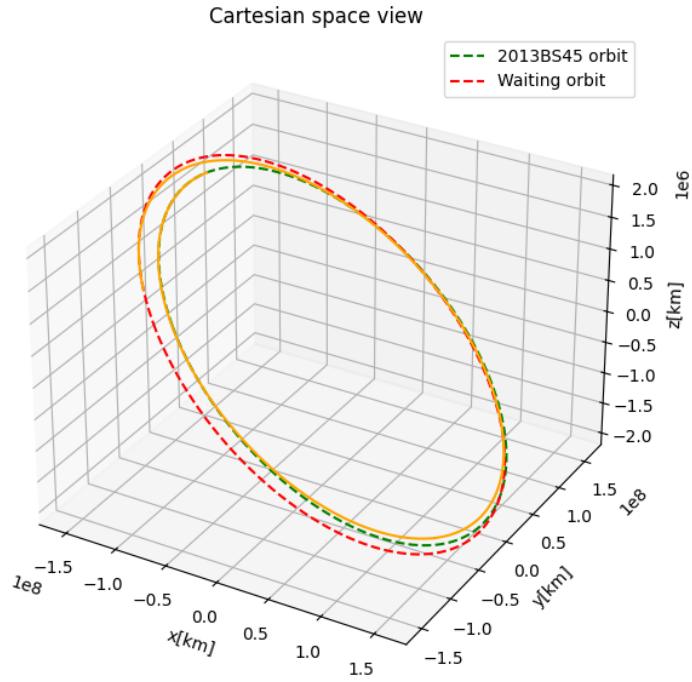


Figura 6.60: 3D transfer towards waiting orbit starting on January the 4th, 2027 from 2013BS45 orbit with arrival on March the 6th, 2028

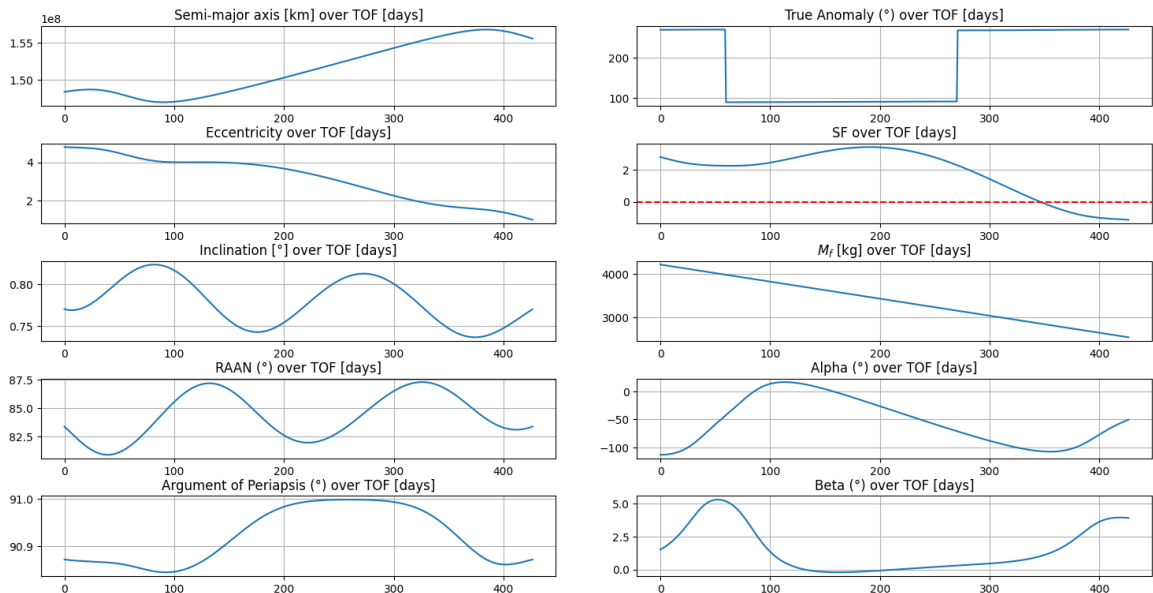


Figura 6.61: Orbital, angular and thrust data from maneuver towards waiting orbit starting on January the 4th, 2027 from 2013BS45 orbit with arrival on March the 6th, 2028

all the maneuvers so far described is already on the waiting orbit ready to rendez-vous with the first one carrying the retrieved mass. According with the results of subsection 6.3.1 the rendez-vous has to happen on the 6th of March 2028.

Given that the target orbit for this maneuver is the orbit of the Earth the least-TOF maneuver that allowed the whole \mathcal{S}_F to be positive (so to obtain the quickest possible maneuver) was searched considering starting and target orbital parameters in table 6.11

	a [AU]	e	i	Ω	ω	ν
Waiting orbit	1.04	0.017	0.77°	83.4°	150.74°	350°
Earth orbit	1.00	0.017	0°	348.73936°	114.20783°	?

Tabella 6.11: Keplerian parameters for starting orbit and target orbit for the last maneuver of the mission

The calculations were made with free-TOF through a try-and-error process that involved the guess of the value of the final ν that the spacecraft was able to reach with a single thrust arc and the so obtained maneuver is described in table 6.12 and in figures 6.62 and 6.63.

TOF [days]	ν_f	m_f (% m_0) [kg]	m_{p_f} (% m_{p_0}) [kg]
329	80.54°	4257.5 (85.15%)	2257.5 (75.25%)

Tabella 6.12: Mass data about the second spacecraft carrying the first spacecraft(2537.15 kg) and the asteroid mass retrieved (15000 kg) back to Earth orbit

The last question to answer to define the last maneuver of the mission was to estimate when it would be possible given the date of arrival on the waiting orbit where the spacecraft carrying the asteroid was moved to have the rendez-vous with the second spacecraft (the equivalent of the *catcher* in the work of Ionescu, Ceriotti and McInnes [23]) and to wait for the ideal alignment with Earth.

The obtained maneuver, as in table 6.12, has a TOF of 329 days so assuming it to begin in the exact day (and from the exact ν) of the rendez-vous between the second spacecraft and the first one (the 6th of March 2028, when $\nu_{start} = 350^\circ$) and to end in $\nu_f = 80.54^\circ$ on the Earth orbit and assuming that the Earth would be exactly there where it is needed to be to have actually have a rendez-vous we get that the transfer would end on the 29th of January 2029 but on that date Earth is at $\nu = 27.13^\circ$ so it is 53.41° behind the necessary position along its orbit. This means that the spacecraft has to wait on the waiting orbit until the misalignment between the Earth and the spacecraft is naturally corrected. In fact, semi-major axis of Earth orbit is smaller than the one of the waiting orbit and therefore its angular velocity in its revolution around the Sun is higher than the one of the spacecraft, so the spacecraft will orbit the Sun staying on the waiting orbit until the moment that the Earth reaches the right position. Given the difference between angular velocities of Earth and Waiting orbit and the $\Delta\nu$ the Earth has to recover we get the time the spacecraft has to wait on the waiting orbit (see table 6.13).

So the spacecraft has to wait 948 days from its rendez-vous on the waiting orbit (6th of March 2028), until the 9th of October 2030 (for more than 2 years and a half), for the beginning of its final transfer that, as table 6.13 indicates, will require a TOF of 329

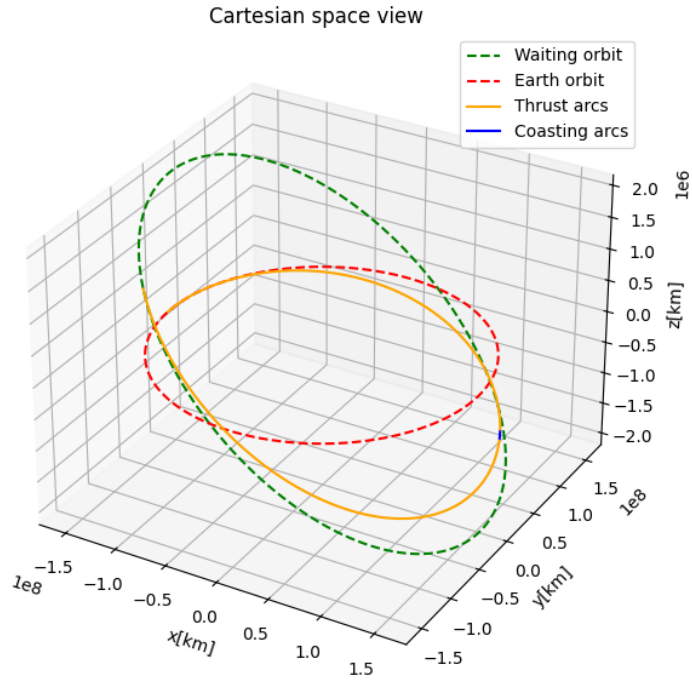


Figura 6.62: 3D minimum-TOF transfer towards Earth orbit at $\nu = 80.54^\circ$

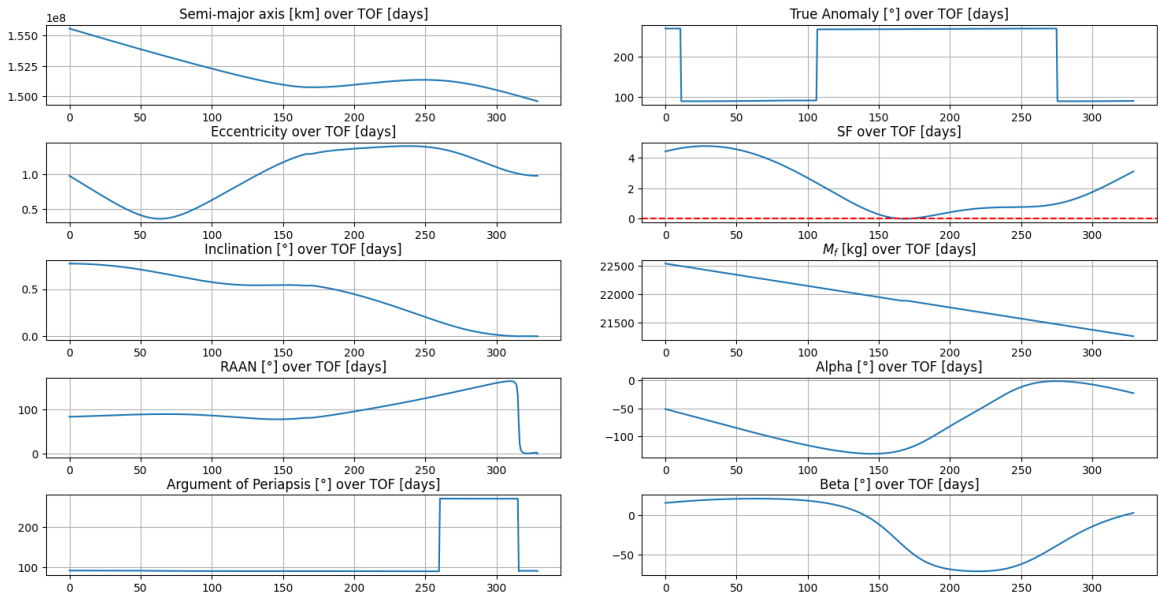


Figura 6.63: Data for the minimum-TOF transfer towards Earth orbit at $\nu = 80.54^\circ$

days with arrival at Earth orbit on September the 3rd, 2031, 7 years and 2 days after the launch of the mission (on September the 1st, 2024).

n_{Earth} [°/s]	n_{wo} [°/s]	Δn [°/s]	$\Delta \nu$ [°]	Δt on wo [d]
$1.1407 \cdot 10^{-5}$	$1.0755 \cdot 10^{-5}$	$6.5174 \cdot 10^{-7}$	53.41	948.49

Tabella 6.13: Waiting time for the spacecraft on the waiting orbit (wo) before the beginning of the maneuver to reach Earth orbit

Influence of the retrieved mass increment over the date of the final arrival to Earth orbit

Besides every possible economical evaluation, the impact of an increment of the desired retrieved mass on the date of the return to Earth orbit for the spacecraft has been analyzed. Acting in the same way as for the calculations regarding the maneuver towards the waiting orbit discussed in subsection 6.3.1, an attempt to increase the mass retrieved from the asteroid 2013BS45 always keeping $\mathcal{S}_F > 0$ throughout the whole maneuver was made. The results of the transfer to move 16000 kg of mass from 2013BS45 orbit to the waiting orbit are collected in table 6.14

m_{ast} [kg]	TOF [days]	ν_f [°]	m_f (% m_0) [kg]	m_{pf} (% m_{p0}) [kg]
15000	427	350	2537.15 (50.74%)	537.15 (17.91%)
16000	496	50	2353.28 (47.06%)	353.28 (11.78%)

Tabella 6.14: Comparison between maneuvers between 2013BS45 orbit and the waiting orbit

So retrieving 1000 kg more from the asteroid makes the transfer towards the waiting orbit (with $\mathcal{S}_F > 0$ for 100% of TOF) 69 days longer in order to target a point in the waiting orbit that in terms of ν is 60°further. Given the analysis previously made in this subsection about the ideal position of the spacecraft and the planet Earth in relation with the Sun for this maneuver to happen (this is also a minimum free-TOF maneuver) we can affirm that because of this "angular delay" in reaching the waiting orbit and in operating the rendez-vous with the second spacecraft the complex of the two spacecrafts and the retrieved asteroid mass will have to wait more on the waiting orbit for the Earth to recover a greater angle of misalignment. In fact if the maneuver towards Earth has to start from the ν along the waiting orbit were the two spacecrafts made the rendez-vous in the very moment they perform it it would take 349 days (so 20 days more than the case where the retrieved mass is 15000 kg, see table 6.15) so the spacecraft would reach the Earth orbit on the 18th of February 2029 (considering as before the 6th of March 2028 as a starting date) when the $\nu_{Earth} = 44.37^\circ$, so the misalignment would be $\Delta \nu = 111.17^\circ$ and knowing the Δn between the two orbits we get that the time the spacecraft has to wait on the waiting orbit before the beginning of the transfer back to Earth orbit is 1974.24 days (nearly 1026 days more then the case of 15000 kg of retrieved asteroid mass, see table 6.16).

In conclusion, those estimations show how trying to exploit all the residual propellant on the first spacecraft to maximize the retrieved asteroid mass during the maneuver towards the waiting orbit can backfire if the goal is to get the retrieved mass to Earth orbit as soon as possible.

m_{ast} [kg]	TOF [days]	ν_0 [°]	ν_f [°]	m_f (% m_0) [kg]	m_{pf} (% m_{p0}) [kg]
15000	329	350	80.54	4257.5 (85.15%)	2257.5 (75.25%)
16000	349	50	155.54	3695.12 (73.90%)	1695.12 (56.50%)

Tabella 6.15: Comparison between maneuvers between the waiting orbit and Earth orbit

m_{ast} [kg]	$\Delta\nu$ [°]	Δt on wo [d]	date of arrival on EO
15000	53.41	948.49	3/09/2031
16000	111.17	1974.24	22/09/2034

Tabella 6.16: Comparison between waiting time for the spacecraft on the waiting orbit (wo) before the beginning of the maneuver to reach Earth orbit between the two cases of retrieved mass considered (15000 kg vs 16000 kg), $\Delta n = 6.5174 \cdot 10^{-7} \text{°/s}$

In fact, as tables 6.14 and 6.16 testify, retrieving 1000 kg more in terms of asteroid mass costs an increment in mass of propellant spent from the first spacecraft of 180 kg but extends the global duration of the mission by 3 years. By the same criteria, we can assume (assuming the phenomenon has a linear progression with the retrieved m_{ast}) that in order to maximize the m_{ast} retrieved (and bring the first spacecraft as close as possible to run out of propellant) we could retrieve more than 18000 kg of asteroid mass but we should not expect that to be delivered home before October 2040. Weather this is convenient or not, it depends on the evaluation of the committer of the mission and on the value of the material composing the asteroids (however, such evaluations are beyond the intent of this thesis).

Comparison with the results of other works

The two-spacecraft mission structure was considered following the work of Ionescu, Ceriotti and McInnes [23]. In that paper impulsive maneuvers were considered in order to allow to the same couple of spacecraft to deflect asteroids from their orbit and then to slow them down when reaching the orbit of the Earth without moving themselves along the trajectory of the deflected asteroid. This strategy, thanks to the impulsive maneuver, allows the *pitcher* to deflect more than one single asteroid moving from the orbit of an asteroid to another one while the *catcher* slows them down as they reach the orbit of the Earth. This forces the comparison to be made, in order for it to be meaningful, with the case from the paper where only 1 asteroid is retrieved. As a result it is possible to notice from fig. 6.64 how the retrieved mass in terms of retrieved mass to initial wet mass ratio for the two-spacecraft strategy is the same of the two-spacecraft mission structure considered for this thesis (with an initial wet mass of 5000 kg the retrieved mass of 15000 kg is exactly 3 times greater than it). The only difference lies in the global TOF of the mission. In fact the impulsive strategy does not require any phasing time to wait on a waiting orbit given that the *catcher* can move itself towards another point of the orbit of the Earth in order for the impulsive Hohmann transfer to be feasible in any moment while electric propulsion requires the optimal alignment with the Earth to be achieved and so this makes the strategy applied for this thesis less convenient time-wise. In fact in the paper [23] missions no longer than 2.5 years are considered and so in the best case the time mission for the retrieval is half of the time necessary for the whole retrieval maneuver

here analyzed to be completed. However, the advantage linked with the absence of any risk of involuntary asteroid disruption through impulsive maneuver guaranteed by electric propulsion [41] along its easier trajectory control has to be considered.

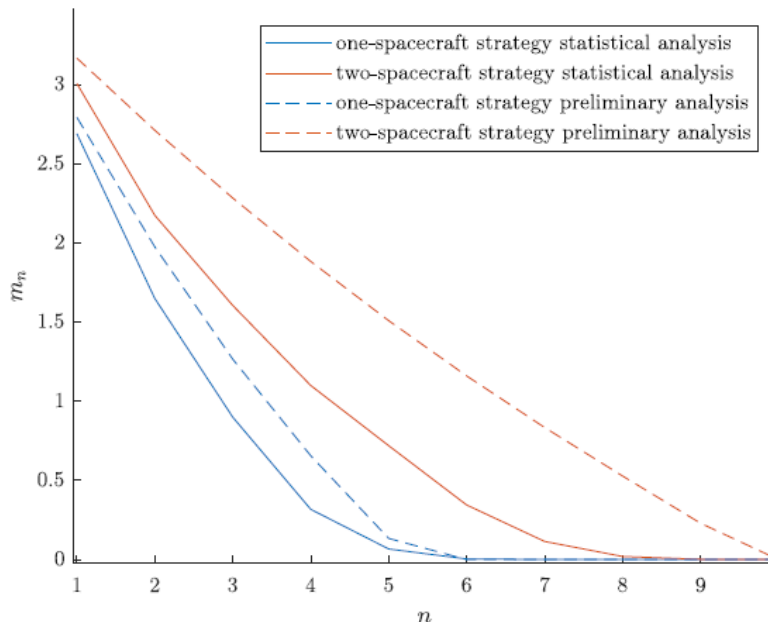


Figura 6.64: Retrieved mass over initial mass ratio over the number of retrieved asteroids from the paper by Ionescu, Ceriotti, McInnes (results and image from [23])

6.4 Conclusions

With the present work of thesis the implemented Python code has been successfully validated through its application to a problem of trajectory optimization aimed at finding the minimum m_p solution for a transfer from the L2 point of the Sun-Earth system towards one of the few selected NEA (from the NASA database considering both numbered and unnumbered candidates). Various families have been obtained, considered and compared in terms of both feasibility and convenience seen the m_f of the spacecraft and the TOF estimated by the optimizer for each of them. Among the so called *Primary family* an incremental trend for m_f of the spacecraft was noted for higher values for TOF. A similar trend was noticed also for the *Secondary family* and the minimum-TOF family of solutions (as shown in fig. 6.52) with different values of m_f that shown to be higher for the lower-TOF ones. In a separate section it was shown that because of misalignment between Earth and the vast majority of the asteroids (the considered asteroid 2013BS45 included) those both cost-wise and time-wise very convenient kind of transfer was not feasible in the foreseeable future (given the 1st of September as the arbitrarily chosen date for the launch of the mission). After a choice was made about the transfer towards the EO to consider for the mission, a mission strategy to balance the maximization of the retrieved mass and the TOF was implemented and two scenarios (in terms of both retrieved mass and TOF) have been considered and compared. The conclusion is that the more mass it is retrieved, the more time it will cost in terms of delay in delivering it back home were the

investors (both public and private) are waiting to see the results of the mission in terms of ROI, so if there is any time constraint the best option is not to retrieve the most of the mass according with the maximum propellant on board of the first spacecraft (whose m_p consumption determines the real upper limit for the result of the mission in terms of retrieved mass) but to find the optimal balance between retrieved mass and TOF of the whole mission. In last instance, a comparison between the obtained results in terms of retrieved mass in respect to the initial mass of the spacecraft and the ones shown by [23] has been made so getting to the conclusion that besides the differences in the propulsive choices the results in the case of one single asteroid retrieved can be considered equivalent in terms of retrieved mass while a reduced flexibility imposes higher TOF in the case of the use of electric propulsion.

6.5 Future Research

It is possible to study more in depth the possibility of a deflection of a NEA, as [16] points out (with a consequent variation of orbital parameters of each NEA), after a close encounter with Earth given the periodical alignments between Earth and NEA and the difference in mass between each asteroid and the Earth which can lead to such perturbations to happen, also given the proximity between their orbits (as from the already discussed definition of NEA) and.

In the context of close encounters, given the potential proximity between earth and the targeted asteroid for the minimum-TOF maneuver to be feasible, it is necessary to understand in each case if the considered alignment in relation with the Sun in terms of true anomaly can lead to a perturbing gravitational interaction for the NEA (with the consequent change of its orbital parameters making impossible for a previously designed mission to reach the targeted asteroid because its movement towards another orbit).

In the context of this thesis gravitational perturbation from third bodies on the spacecraft trajectory were not taken into consideration so a very interesting future work could be implementing perturbation from Earth, Moon and other planetary bodies to reach a high-fidelity model as the one defined by [34].

Because of a lack of robustness of the code in converging to a solution when targeting certain regions of the targeted orbit implementing the MPBVP through an a-priori discretization of the time domain of the solution can improve the possibilities of finding a solution towards those values of true anomaly.

As a consequence of the implementation of the MPBVP the implementation of the equations of the TBP can guarantee a boost in flexibility for the code because of the increased group of cases and problems it could be applied to. In the context of the case study considered for this thesis the implementation of the TBP would allow to consider families of trajectories called *invariant manifolds* ([48], [55] and others) that are mathematically proven to be able to drive a spacecraft retrieving asteroids towards periodical orbits around Lagrange points of the Sun-Earth or Earth-Moon system with very low ΔV cost so making less expensive, from a mass budget standpoint, the mission of pushing an asteroid towards an orbit around the Earth. In a similar fashion it is possible to introduce the flyby with the Moon [17] or with the Earth ([49], [50] and others) to make every capture maneuver of this kind even less expensive.

In order to improve our understanding of the problem of the lack of convergence on certain regions of the targeted orbit, finding solutions belonging to the primary families of solutions targeting rendez-vous beyond the one on the 14th of January 2027 can be useful to gain more information about the size of that region where no convergent solutions can be found.

Appendice A

Equations for the adjoint variables

$$\begin{aligned}\frac{d\lambda_x}{dt} &= \left(\frac{\mu}{r^{3/2}} - \frac{3\mu}{r^{5/2}}x^2 \right) \lambda_{v_x} - \frac{3\mu}{r^{5/2}}x (\lambda_{v_y}y + \lambda_{v_z}z) \\ \frac{d\lambda_y}{dt} &= \left(\frac{\mu}{r^{3/2}} - \frac{3\mu}{r^{5/2}}y^2 \right) \lambda_{v_y} - \frac{3\mu}{r^{5/2}}y (\lambda_{v_x}x + \lambda_{v_z}z) \\ \frac{d\lambda_z}{dt} &= \left(\frac{\mu}{r^{3/2}} - \frac{3\mu}{r^{5/2}}z^2 \right) \lambda_{v_z} - \frac{3\mu}{r^{5/2}}z (\lambda_{v_x}x + \lambda_{v_y}y) \\ \frac{d\lambda_{v_x}}{dt} &= -\lambda_x \\ \frac{d\lambda_{v_y}}{dt} &= -\lambda_y \\ \frac{d\lambda_{v_z}}{dt} &= -\lambda_z \\ \frac{dm}{dt} &= -T \frac{\lambda_V}{m^2}\end{aligned}\tag{A.1}$$

Appendice B

List of the selected asteroids

In this appendix are collected the tables showing orbital and physical data regarding the selected asteroids for this thesis. As previously discussed in these are the 20 asteroids from the NEA database from *NASA Jet propulsion laboratory* [37], JPL, fulfilling all the selected criteria as in section 5.1.

Many of them have been discovered only in the last 5 years (as shown by their recorded name) so they are not present in many of the works in literature (for esample see [16]).

Table B.1 collects all the keplerian parameters of the orbits these asteroids are currently orbiting the Sun on and that have been used for optimal trajectory calculation to target them as destination of the desired maneuver In the second column it is also reported the *apparent magnitude*, H , that is useful for the estimation of their mass as for eqs. 5.2 and 5.3 .

Table B.2 collects other orbital characteristics as the perihelion and aphelion of their orbits along with their orbital period (in days) and their circular velocity around the Sun. Lastly, for all the selected asteroids the value of the necessary ΔV from Earth considering a Hohmann's maneuver to reach them has been reported.

Table B.3 collects the results of the estimation procedures for mass and diameter of every considered asteroid (given that the albedo p_v of each asteroid is considered in a range of [0.05, 0.5]).

name	H	e	a [AU]	i [°]	Ω [°]	ω [°]
2000SG344	24.7	0.0668	0.9773	0.11	191.76	275.51
2013BS45	25.9	0.0838	0.9915	0.77	83.4	150.74
2021LD6	27.2	0.0999	0.9885	0.77	100.66	288.7
2020CD3	31.74	0.0123	1.029	0.63	82.23	50.02
2019GF1	27.5	0.0484	0.9899	1.24	4.15	326.09
2011UD21	28.5	0.0304	0.9786	1.06	22.35	209.76
2022NX1	28.07	0.0246	1.024	1.07	274.46	171.26
2018PK21	25.88	0.0809	0.9833	1.22	302.63	227.42
2021VH2	28.82	0.0792	1.013	1.31	222.9	260.65
2021GM1	30.4	0.0254	0.9781	1.18	176.24	226.15
2006JY26	28.4	0.0831	1.01	1.44	43.46	273.65
2007VU6	26.59	0.0906	0.9762	1.22	220.24	34.87
2014WU200	29.1	0.0715	1.028	1.27	265.65	226.54
2023RX1	30.25	0.0282	0.9968	1.6	168.82	38.56
2023HM4	27.69	0.0494	1.012	1.54	68	34.66
2006BZ147	25.4	0.0987	1.023	1.41	139.83	94.83
2010VQ98	28.2	0.0271	1.023	1.48	46.17	341.71
2021RZ3	27.33	0.0533	1.014	1.67	343.02	243.38
2020UO4	28.64	0.0916	0.9737	1.46	210.45	64.04
2020WY	26.2	0.0286	1.02	1.7	107.1	180.41

Tabella B.1: Keplerian parameters of the selected asteroids

name	aphelion [AU]	perihelion [AU]	v_c [m/s]	ΔV fr. Earth [m/s]	T [days]
2000SG344	0.91201636	1.04258364	30.10427642	0.351239338	353
2013BS45	0.9084123	1.0745877	29.88792626	0.440491415	361
2021LD6	0.88974885	1.08725115	29.93324536	0.464980894	359
2020CD3	1.0163433	1.0416567	29.33826689	0.572174194	382
2019GF1	0.94198884	1.03781116	29.91207081	0.683592276	360
2011UD21	0.94885056	1.00834944	30.08427408	0.691442655	354
2022NX1	0.9988096	1.0491904	29.40980629	0.707484924	379
2018PK21	0.90375103	1.06284897	30.01228921	0.724219514	356
2021VH2	0.9327704	1.0932296	29.56905327	0.73262731	373
2021GM1	0.95325626	1.00294374	30.09196257	0.751718061	354
2006JY26	0.926069	1.093931	29.61293514	0.778273592	371
2007VU6	0.88775628	1.06464372	30.12123266	0.788265069	353
2014WU200	0.954498	1.101502	29.352533	0.833106515	381
2023RX1	0.96869024	1.02490976	29.80836309	0.834656237	364
2023HM4	0.9620072	1.0619928	29.58365888	0.839451113	372
2006BZ147	0.9220299	1.1239701	29.42417708	0.855115633	378
2010VQ98	0.9952767	1.0507233	29.42417708	0.887882758	378
2021RZ3	0.9599538	1.0680462	29.55446927	0.915674901	373
2020 UO4	0.88450908	1.06289092	30.1598764	0.923325366	351
2020WY	0.990828	1.049172	29.46741616	0.969979491	377

Tabella B.2: Orbital characteristics of the selected asteroids

name	m_{max} [kg]	m_{min} [kg]	d_{max} [m]	d_{min} [m]
2000SG344	78875008.99	19346700.32	68.24015094	21.57943048
2013BS45	15029323.13	3686437.748	39.26810818	12.41766613
2021LD6	2494246.789	611796.3821	21.57943048	6.824015094
2020CD3	4709.116359	1155.066277	2.667104172	0.843412394
2019GF1	1647932.511	404209.8612	18.79489824	5.943468684
2011UD21	413941.9314	101532.9266	11.85877909	3.750075218
2022NX1	749789.6164	183910.6606	14.45572836	4.571302686
2018PK21	15450389.12	3789718.087	39.63145151	12.53256538
2021VH2	266035.395	65253.96481	10.23387195	3.236234466
2021GM1	29987.44205	7355.410314	4.943561926	1.563291544
2006JY26	475268.9277	116575.3974	12.41766613	3.926810818
2007VU6	5793478.795	1421041.969	28.5785361	9.037326626
2014WU200	180692.2067	44320.72994	8.995803882	2.844722965
2023RX1	36892.61347	9049.131606	5.297122041	1.675097069
2023HM4	1267475.058	310890.1085	17.22027088	5.445527791
2006BZ147	29987442.05	7355410.314	49.43561926	15.63291544
2010VQ98	626526.4665	153676.3031	13.61570015	4.305662442
2021RZ3	2084200.145	511218.9034	20.32544107	6.427468824
2020UO4	341145.3231	83677.15472	11.11834072	3.515928047
2020WY	9929775.317	2435605.266	34.20109247	10.81533507

Tabella B.3: Physical characteristics of the selected asteroids

Bibliografia

- [1] Amirah R. Algethami, Colin R. McInnes, and Matteo Ceriotti. The capture of small near-earth asteroids in a bound binary pair in earth's orbit. *Acta Astronautica, Elsevier, January 2024*, 214:545–552, 2024.
- [2] Inc. Anaconda et al. Link for numba documentation. <https://numba.readthedocs.io/en/stable/>, 2024. [Online: accessed 15-July-2024].
- [3] Niklas Anthony and M. Reza Emami. Asteroid engineering: The state-of-the-art of near-earth asteroids science and technology. *Progress in Aerospace Sciences*, 100:1–17, 2018.
- [4] M. Azadmanesh, J. Roshanian, and M. Hassanalilian. On the importance of studying asteroids: A comprehensive review. *Progress in Aerospace Sciences*, 142:100957, 2023.
- [5] Roger R. Bate, Donald D. Mueller, Jerry E. White, and William W. Saylor. *Fundamentals of Astrodynamics, Second Edition*. Dover Publications, 2020.
- [6] L. Bayón, J.A. Otero, P.M. Suárez, and C. Tasis. New developments in the application of optimal control theory to therapeutic protocols. *Mathematical Biosciences*, 272:34–43, 2016.
- [7] Brad R Blair. The role of near-earth asteroids in long-term platinum supply. *Space Resources Roundtable II*, 1070(5), 2000.
- [8] Claudio Bombardelli and Jesus Peláez. Ion beam shepherd for asteroid deflection. *Journal of Guidance, Control, and Dynamics*, 34(4):1270–1272, 2011.
- [9] Lorenzo Casalino. *Dispense del corso di Propulsione Spaziale*. Politecnico di Torino, Torino, 2023.
- [10] Queenie Hoi Shan Chan and Michael E. Zolensky. Chapter 4 - water and organics in meteorites. In Rebecca Thombre and Parag Vaishampayan, editors, *New Frontiers in Astrobiology*, pages 67–110. Elsevier, 2022.
- [11] Andrew F. Cheng, Andrew S. Rivkin, Patrick Michel, Justin Atchison, Olivier Barnouin, Lance Benner, Nancy L. Chabot, Carolyn Ernst, Eugene G. Fahnestock, Michael Kueppers, Petr Pravec, Emma Rainey, Derek C. Richardson, Angela M. Stickle, and Cristina Thomas. Aida dart asteroid deflection test: Planetary defense and science objectives. *Planetary and Space Science*, 157:104–115, 2018.

-
- [12] Howard D. Curtis. Chapter 2 - the two-body problem. In Howard D. Curtis, editor, *Orbital Mechanics for Engineering Students (Third Edition)*, pages 59–144. Butterworth-Heinemann, Boston, third edition edition, 2014.
- [13] Longjun Dong, Daoyuan Sun, Weiwei Shu, and Xibing Li. Exploration: Safe and clean mining on earth and asteroids. *Journal of Cleaner Production*, 257:120899, 2020.
- [14] Chongrui Du, Liangjun Song, Jiye Zhang, and Yi Liu. A novel calculation method for low-thrust transfer trajectories in the earth-moon restricted three-body problem. *Aerospace Science and Technology*, 147:109048, 2024.
- [15] Quora Forum. Link of the image of the lagrange points. <https://www.quora.com/How-big-would-LaGrange-Point-L4-or-L5-be-Are-we-talking-100s-of-metres-or-miles>, 2019. [Online: accessed 16-July-2024].
- [16] Daniel García Yárnoz, Joan-Pau Sánchez, and C. McInnes. Easily retrievable objects among the neo population. *Celestial Mechanics and Dynamical Astronomy*, 116:367–388, 04 2013.
- [17] Shengping Gong and Junfeng Li. Asteroid capture using lunar flyby. *Advances in Space Research*, 56(5):848–858, 2015.
- [18] Jeremy L Gustafson. Space nuclear propulsion fuel and moderator development plan conceptual testing reference design. *Nuclear Technology*, 207(6):882–884, 2021.
- [19] Zaki Hasnain, Christopher A. Lamb, and Shane D. Ross. Capturing near-earth asteroids around earth. *Acta Astronautica*, 81(2):523–531, 2012.
- [20] Jeannette Heiligers, Giorgio Mingotti, and Colin McInnes. Optimisation of solar sail interplanetary heteroclinic connections. 03 2014.
- [21] Gerald R. Hintz. *Orbital Maneuvers*, pages 61–137. Springer International Publishing, Cham, 2022.
- [22] M. Hirabayashi, Y. Mimasu, N. Sakatani, S. Watanabe, Y. Tsuda, T. Saiki, S. Kikuchi, T. Kouyama, M. Yoshikawa, S. Tanaka, S. Nakazawa, Y. Takei, F. Terui, H. Takeuchi, A. Fujii, T. Iwata, K. Tsumura, S. Matsuura, Y. Shimaki, S. Urakawa, Y. Ishibashi, S. Hasegawa, M. Ishiguro, D. Kuroda, S. Okumura, S. Sugita, T. Okada, S. Kameda, S. Kamata, A. Higuchi, H. Senshu, H. Noda, K. Matsumoto, R. Suetsugu, T. Hirai, K. Kitazato, D. Farnocchia, S.P. Naidu, D.J. Tholen, C.W. Hergenrother, R.J. Whiteley, N.A. Moskovitz, and P.A. Abell. Hayabusa2 extended mission: New voyage to rendezvous with a small asteroid rotating with a short period. *Advances in Space Research*, 68(3):1533–1555, 2021.
- [23] Livia Ionescu, Colin R. McInnes, and Matteo Ceriotti. A multiple-vehicle strategy for near-earth asteroid capture. *Acta Astronautica*, 199:71–85, 2022.
- [24] Robert G. Jahn. *Physics of Electric Propulsion*. McGraw-Hill, 1968.

-
- [25] Jun'ichiro Kawaguchi, Akira Fujiwara, and Tono Uesugi. Hayabusa—its technology and science accomplishment summary and hayabusa-2. *Acta Astronautica*, 62(10):639–647, 2008.
- [26] Dan Lev, Roger M Myers, Kristina M Lemmer, Jonathan Kolbeck, Hiroyuki Koizumi, and Kurt Polzin. The technological and commercial expansion of electric propulsion. *Acta Astronautica*, 159:213–227, 2019.
- [27] Daniel Liberzon. *Calculus of Variations and Optimal Control Theory*. Princeton University Press, 2012.
- [28] Neus Lladó, Yuan Ren, Josep J. Masdemont, and Gerard Gómez. Capturing small asteroids into a sun–earth lagrangian point. *Acta Astronautica*, 95:176–188, 2014.
- [29] Edward T Lu and Stanley G Love. Gravitational tractor for towing asteroids. *Nature*, 438(7065):177–178, 2005.
- [30] Philip Lubin and Alexander N. Cohen. Asteroid interception and disruption for terminal planetary defense. *Advances in Space Research*, 71(3):1827–1839, 2023.
- [31] Christie Maddock, Joan Pau Sanchez Cuartiellas, Massimiliano Vasile, and Gianmarco Radice. Comparison of single and multi-spacecraft configurations for nea deflection by solar sublimation. In *AIP conference Proceedings*, volume 886, pages 303–316. American Institute of Physics, 2007.
- [32] Danylo Malyuta, Yue Yu, Purnanand Elango, and Behçet Açıkmeşe. Advances in trajectory optimization for space vehicle control. *Annual Reviews in Control*, 52:282–315, 2021.
- [33] Raymond E. March. Osiris-rex: a nasa asteroid space mission. *International Journal of Mass Spectrometry*, 469:116677, 2021.
- [34] Luigi Mascolo. *Low-Thrust Optimal Escape Trajectories from Lagrangian Points and Quasi-Periodic Orbits in a High-Fidelity Model*. PhD thesis, Tesi di dott. Torino: Politecnico di Torino, 2023.
- [35] Colby C. Merrill, Carl J. Geiger, Abu T.M. Tahsin, Dmitry Savransky, and Mason Peck. Creating a contact binary via spacecraft impact to near-earth binary asteroid (350751) 2002 aw. *Acta Astronautica, Elsevier, January 2024*, 214:629–640, 2024.
- [36] K. Mishima and K. Yamashita. Free-time and fixed end-point multi-target optimal control theory: Application to quantum computing. *Chemical Physics*, 379(1):13–22, 2011.
- [37] JPL NASA Jet Propulsion Laboratory. Link for downloading ephemerides. <https://ssd.jpl.nasa.gov/>, 2024. [Online: accessed 2-July-2024].
- [38] Bifeng Pan, Zheng Chen, Ping Lu, and Bo Gao. Reduced transversality conditions for optimal space trajectories. *Journal of Guidance, Control and Dynamics*, 36, number 5:1289–1300, 2013.

-
- [39] Robert E. Pritchett. *Numerical methods for low-thrust trajectory optimization*. Purdue University, West Lafayette, Indiana, 2016.
- [40] I. Michael Ross. 6 - space trajectory optimization and l1-optimal control problems. In Pini Gurfil, editor, *Modern Astrodynamics*, volume 1 of *Elsevier Astrodynamics Series*, pages 155–VIII. Butterworth-Heinemann, 2006.
- [41] Russell L Schweickart, Edward T Lu, Piet Hut, and Clark R Chapman. The asteroid tugboat. *Scientific American*, 289(5):54–61, 2003.
- [42] L. Sertorio and Elif Renda. *Orbite (e vita nell’Universo)*. 11 2012.
- [43] HU Shou-cun, ZHAO Hai-bin, and JI Jiang-hui. Statistical analysis on the number of discoveries and discovery scenarios of near-earth asteroids. *Chinese Astronomy and Astrophysics*, 47(1):147–176, 2023.
- [44] Thomas E Skinner, Timo O Reiss, Burkhard Luy, Navin Khaneja, and Steffen J Glaser. Application of optimal control theory to the design of broadband excitation pulses for high-resolution nmr. *Journal of Magnetic Resonance*, 163(1):8–15, 2003.
- [45] Ernst Stuhlinger. Electric space propulsion systems. *Space Science Reviews*, 7(5):795–847, 1967.
- [46] Nina N. Subbotina and Timofey B. Tokmantsev. Optimal control theory applications to dynamic reconstruction problems. *IFAC Proceedings Volumes*, 45(25):21–26, 2012. 15th IFAC Workshop on Control Applications of Optimization.
- [47] George P. Sutton and Oscar Biblarz. *Rocket Propulsion Elements, Ninth Edition*. Wiley, 2017.
- [48] Joan Pau Sánchez and Daniel García Yáñez. Asteroid retrieval missions enabled by invariant manifold dynamics. *Acta Astronautica*, 127:667–677, 2016.
- [49] Minghu Tan, Colin McInnes, and Matteo Ceriotti. Capture of small near-earth asteroids to earth orbit using aerobraking. *Acta Astronautica*, 152:185–195, 2018.
- [50] Minghu Tan, Colin McInnes, and Matteo Ceriotti. Low-energy near earth asteroid capture using earth flybys and aerobraking. *Advances in Space Research*, 61(8):2099–2115, 2018.
- [51] L’infinito teatro del cosmo. Link of the image of the gravitational potential. <http://www.infinitoteatrodelcosmo.it/tag/punti-di-lagrange/>. [Online: accessed 16-July-2024].
- [52] Merel Vergaaij, Colin R. McInnes, and Matteo Ceriotti. Economic assessment of high-thrust and solar-sail propulsion for near-earth asteroid mining. *Advances in Space Research*, 67(9):3045–3058, 2021. Solar Sailing: Concepts, Technology, and Missions II.

- [53] Dehant Véronique, Breuer Doris, Claeys Philippe, Debaille Vinciane, De Keyser Johan, Javaux Emmanuelle, Goderis Steven, Karatekin Özgür, Spohn Tilman, Vandaele Ann Carine, Vanhaecke Frank, Van Hoolst Tim, and Wilquet Valérie. From meteorites to evolution and habitability of planets. *Planetary and Space Science*, 72(1):3–17, 2012. Mars Habitability.
- [54] Vincenzo Zappalà. L’infinito teatro del cosmo. <http://www.infinitoteatrodelcosmo.it/2016/07/01/il-problema-dei-due-corpi-da-newton-a-keplero/>, 2016. [Online: accessed 16-July-2024].
- [55] Àngel Jorba and Begoña Nicolás. Using invariant manifolds to capture an asteroid near the l3 point of the earth-moon bicircular model. *Communications in Nonlinear Science and Numerical Simulation*, 102:105948, 2021.